Effet de l'orientation sur les nanofilms de Pd/Pt(hkl) : électrodépôt, caractérisation et isothermes électrochimiques de Pd-H Orientation effect on Pd/Pt(hkl) nanofilms

Bruno Alarcon Fernandes Previdello

UNIVERSITÉ DE GRENOBLE

THÈSE

Pour obtenir le grade de

DOCTEUR DE L'INP GRENOBLE

Spécialité : **Matériaux, Mécanique, Génie Civil, Électrochimie**

Arrêté ministériel : 7 août 2006

Présentée par

Bruno ALARCON FERNANDES PREVIDELLO

Thèse dirigée par **Yvonne Soldo-Olivier**
codirigée par **Eric Sibert**
préparée au sein du **Laboratoire d'Electrochimie et de Physico-chimie des Matériaux et des Interfaces**
dans l'**École Doctorale Ingénierie-Matériau Mécanique Énergétique Environnement procédés Production**

Effet de l'orientation sur les nanofilms de Pd/Pt(hkl) : électrodépôt, caractérisation et isothermes électrochimiques de Pd-H

Orientation effect on Pd/Pt(hkl) nanofilms: electro-deposition, characterization and electrochemical Pd-H isotherms

Thèse soutenue publiquement le **8 Avril 2013**, devant le jury composé de :

M. Marian CHATENET
Professeur à Grenoble-INP, Président

M. Boniface KOKOH
Professeur à l'Université de Poitiers, Rapporteur

M. Pierre Antoine BONNEFONT
Maître de Conférences à l'Université de Strasbourg, Rapporteur

M. Emmanuel MAISONHAUTE
Professeur à l'Université Pierre et Marie Curie, Paris, Examinateur

Mme. Yvonne SOLDO-OLIVIER
Chargée de Recherche CNRS, Directeur de thèse

M. Eric SIBERT
Chargé de Recherche CNRS, Co-directeur de thèse

Résumé

Le présent travail s'intéresse à l'électro-dépôt et à la caractérisation des nanofilms Pt/Pd(hkl) ainsi que leurs propriétés en relation avec le stockage d'hydrogène. Les effets de taille nanométrique, de l'épaisseur et de l'orientation cristallographique du substrat ont été étudiés.

En comparant les films Pd/Pt(111) et Pd/Pt(100), des caractéristiques distinctes ont été observées aussi bien pour les courbes d'électro-dépôt que durant les caractérisations électrochimiques et par AFM *ex situ*. Les dépôts Pd/Pt(100) ont montré la présence d'un dépôt en sous tension jusqu'à deux couches atomiques, ce qui est assez inhabituel. Les films plus épais montrent la présence de pyramides à base carrée alignées sur l'orientation (100) du substrat. Au contraire, seule la première couche de Pd/Pt(111) se dépose en sous-tension et le dépôt présente un caractère pseudomorphe jusqu'à 10 couches complètes.

L'absorption d'hydrogène dans les nanofilms de Pd/Pt(100) a été étudiée avec une méthode « classique » dans une solution d'acide sulfurique. Nous avons développé une nouvelle méthode recourant à une électrode tournante à ménisque suspendu pour mesurer l'insertion d'hydrogène dans les films les plus minces de Pd/Pt(111), où l'insertion d'hydrogène et le dégagement de H_2(g) ne sont pas bien séparés.

Les isothermes d'insertion d'hydrogène présentent des points communs entre les deux systèmes, comme la réduction du taux maximal d'insertion $(H/Pd)_{max}$ comparé au Pd massif, valeur qui décroît avec la réduction d'épaisseur. La largeur de la région biphasique décroît aussi avec la réduction d'épaisseur de film et présent une pente. Cette pente a été attribuée à la présence de sites d'insertion non-équivalents résultant des contraintes induites par le substrat. Cependant, pour Pd/Pt(100), la pente est moins prononcée et la valeur de $(H/Pd)_{max}$ décroît plus rapidement avec l'épaisseur. Sa valeur pour Pd_{5ML}/Pt(100) est à peine supérieure au taux d'insertion α_{max} du Pd massif.

Mots clés : électro-dépôt de Pd, dépôt en sous tension, monocristaux de Pt, nanofilms, insertion d'hydrogène, isothermes électrochimiques, électrode tournante à ménisque suspendu

Abstract

The present work focuses on the electro-deposition and characterization of Pd/Pt(hkl) nanofilms and on their properties concerning hydrogen storage. The effects of the nanometric size, of the thickness and of the substrate's orientation have been studied.

Comparing Pd/Pt(111) and Pd/Pt(100) films, distinct features were observed either in the electrodeposition curve or in the electrochemical and *ex situ* AFM characterizations. Pd/Pt(100) deposits have shown the presence of an UPD process up to two layers, which is a quite uncommon phenomenon. Thicker films show the presence of square based pyramids, following the substrate's (100) orientation. On the contrary, only the first layer is Under Potentially Deposited in Pd/Pt(111) films and the deposit presents a pseudomorphic character up to about 10 complete layers.

Hydrogen absorption into the Pd/Pt(100) nanofilms was studied following a "classical" method in sulphuric acid medium. We have developed a new method using the hanging meniscus rotating disk electrode (HMRDE) to measure the hydrogen insertion into ultra-thin Pd/Pt(111) films, where H insertion and HER (Hydrogen Evolution Reaction) are not well separated. The hydrogen insertion isotherms present some common points between the two studied systems, like smaller value of the maximum hydrogen insertion rate $(H/Pd)_{max}$ compared to bulk Pd, value which decreases with the decrease of the thickness. The two-phase region width decreases with film thickness as well and presents a slope. Such slope has been attribtued to the presence of non-equivalent insertion sites due to substrate induced constraints. Nevertheless, for Pd/Pt(100) the slope is less pronounced and $(H/Pd)_{max}$ value decreases more rapidly with thickness. Its value in correspondence of Pd_{5ML}/Pt(100) is only slightly higher than the α_{max} insertion rate of bulk Pd.

Keywords: Pd electro-deposition, UPD, platinum single crystal, nanofilms, hydrogen insertion, electrochemical isotherms, HMRDE.

“Aos meus avós que muito ajudaram em minha educação”

Acknowledgements

First of all I would like to acknowledge my family, that even if they were not physically present they were constantly giving their support and their best thoughts for my work.

My companion Daniella, for the support and the help through the rough times.

To the numerous friends that remained away in Brasil but were in touch through the on-line conversations.

To the friends that I have made in France and that undoubtedly will remain for life: Luis, Thiago, Nina, Eduardo, Koxo, Giovanni, Marcio, Gilberto, Leandro (valeu), Belen and Lorenço (gracias), Howard and Hanna (tack), Pyo-McGayver, Marc, Romain, Anicet (merci).

To my supervisors Yvonne and Eric for the scientific knowledge and the patience during the work.

And for sure, to the many friends of the LEPMI as Marian, Fred, Ricardo, Laetitia, Guillaume, Nicola, Benoit, Pascal, Marie, Manu, Julien, Kenia, Douglas, Livia, Lais, Tharton and to all that in one way or another have contribute and helped me during this years.

Mireille Maret (SIMAP) for the collaboration in the AFM analysis.

“Only the one who does not question is safe from making a mistake.”
— Albert Einstein ---

Table of Contents

General Introduction

The economic development of most countries in the world largely depends on fossil fuel energies. Although the use of such energies provides indisputable advantages, resulting in the development of our modern society, several drawbacks must be highlighted. The increase of the greenhouse effect in relation to CO_2 production resulting from the burning of fossil fuels and the atmospheric pollution (CO, NO_x, HC…) constitute an important challenge for the next years. One can also mention the pollution generated by accidental oil spills.

In this context, the rational exploitation of renewable and clean energy resources replacing fossil fuel is a worldwide challenge.

Hydrogen as an energy vector appears to be a key technology. However its utilization at a large scale is still difficult, due to two main problems: the production cost and the storage. Nowadays, hydrogen is mostly chemically extracted from fossil fuels. It requires extra expenses to remove impurities like CO. Its extraction also produces large amounts of CO_2. There are other ways to produce hydrogen by bioreactors, electrolysis, thermolysis and redox chemical reaction. Indeed, they are presently not very efficient and must be improved. Several ways are also explored to improve hydrogen storage. Hydrogen is a highly reactive (extremely flammable) gas at ambient temperature, with a low energy volume density. The compression, the liquefaction and the storage as metallic hydride are the main methods under investigation.

Pd is widely studied in different areas due to its high catalytic properties versus reactions involving hydrogen. In particular it is very efficient towards the insertion/desinsertion of atomic hydrogen. Even if it is not of practical interest for hydrogen storage, due to high price and strong degradation, it is an interesting model system for the comprehension of the mechanisms involved in hydrogen insertion/desinsertion processes in solids. Some light alloys of Li and Mg present high capacity for hydrogen storage. Conversely, they present a low kinetic for H_2 bond breaking and they may be oxidized by traces of oxygen or water. One suggestion is to put a thin Pd film on the surface of such light alloys. This would provide a high catalytic activity for H_2 dissociation, protect the material from contamination, but minimize the quantity of Pd.

The study of the properties of ultra-thin Pd films towards hydrogen insertion/desinsertion processes is the challenge of our work, where the effect of the nanometric size and of the support must be taken into account.

In order to get a better understanding of the phenomenon, we have considered Pd nanofilms well-defined at the atomic scale. This can only be obtained by using a well-defined substrate like a single crystal cut along a precise crystallographic orientation. We selected Pt as first substrate because its lattice parameter is very similar to the one of Pd (+0.7 %), which should make possible a pseudomorphic growth at least of the first adlayers. Two different orientations, Pt(100) and Pt(111), have been experimented.

In our study we have firstly developed the Pd nanofilms electrochemical preparation on Pt(100), following the procedure previously optimized for Pd/Pt(111) deposits in LEPMi by C. Lebouin.

In the second part of this thesis we have studied the hydrogen insertion in Pd nanofilms into both on Pd/Pt(111) and Pd/Pt(100) films. Hydrogen insertion is performed by electrochemical reduction of H^+ in acid solution. The quantity of inserted hydrogen is deduced from charge measurement at the electrode.

Indeed, reactions like hydrogen evolution can occur in parallel. We could not get rid of such contribution for the thinner Pd/Pt(111) films with existing methods. For this system we developed a new method for hydrogen insertion isotherm measurements using a hanging meniscus rotating disk electrode.

This work will be presented in four chapters. Chapter 1 will present a bibliographic review on Pd/Pt(100) nanofilms preparation and characterization. In chapter 2 we will focus on the electrochemical deposition and characterizations of Pd/Pt(100) deposits. Chapter 3 contains an introduction to hydrogen insertion into bulk Pd followed by a bibliographic study of hydrogen insertion into Pd nanoparticles and Pd nanofilms. Chapter 4 presents the study of the electrochemical hydrogen insertion isotherms of Pd/Pt(100) and Pd/Pt(111) nano-films.

1 Bibliographic study: deposition of ultra-thin Pd layers onto Pt(100) single crystal

This chapter will give a review of the studies on various topics involved in the deposition of Pd thin films onto Pt(111) and Pt(100) single crystals. We will start with a brief introduction to the crystallographic structures, to the hydrogen adsorption reactions used as probe in the electrochemical characterizations of the two single crystal Pt surfaces. The chapter will then give an overview of the studies present in the literature on Pd films electro-deposition and their characterizations.

1.1 History

The surface science in general and surface chemistry in particular have a long and distinguished history[1]. The application of catalysis started in 1746 by John Roebuck when he developed the *lead chamberprocess*[2] (bell process) for the manufacture of sulfuric acid, using a NO/NO_2 catalyst[3]. But only in 1796, Martinus van Marum reported the dehydrogenation of alcohols when put in contact with a metal surface (Adsorption, Ion Exchange and Catalysis) showing the importance of surfaces in chemical transformations. It was followed by the discovery of the platinum-surface-catalyzed reaction of H_2 and O_2 by Johann Wolfgang Döbereiner (1800s)[1,4–6], the experiment known as “Döbereiner’s Tinder box”. It is considered as the starting point of surface catalysis. The experiment consists of hydrogen gas production from metallic zinc in sulfuric acid solution[1,7,8]. But at the same time, Sir Humphry Davy began his study on the oxidation of methane on Pt, also considered by some authors as the beginning of surface catalysis. It is important to note that many scientists contributed to the growth of catalysis and surface science to allow the present knowledge on this scientific field. There was still a long way down to the nanoscale studies. The Figure 1.1 shows a timeline of the historical development of surface chemistry.

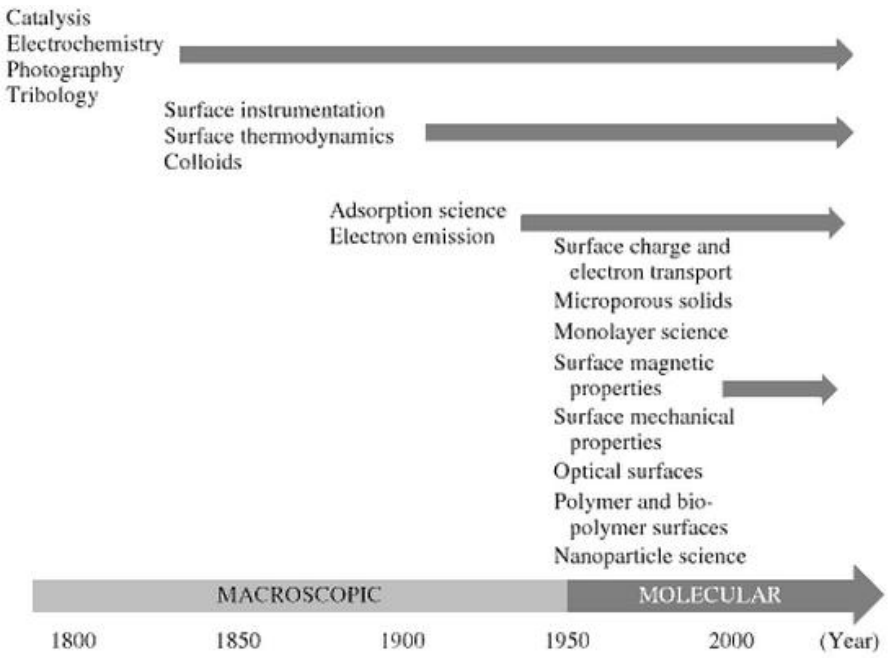

Figure 1.1 : Timeline of the historical development of surface chemistry[1].

The advent in the 1950s of ultrahigh vacuum systems (developed for researches in space sciences) provided to surface chemistry new challenges and opportunities, resulting in an explosive growth of the discipline. New surface instrumentations and techniques have been developed that allowed the study of surface properties on the atomic scale. Clean surfaces of single crystals could be studied for the first time[1,9].

One of the main goals in modern electrochemical surface science is to establish relations between the surface structure of an electrode and its effect on a given electrochemical reaction, like metal deposition, adsorption of atoms, ions and molecules, oxidation of small organic molecules etc. These reactions are of utmost importance in electrocatalysis. Single crystalline materials are often used as model systems due to the rather complex behavior of polycrystalline surfaces, the structure of which cannot be easily controlled and characterized[10]. Therefore, the science of well-ordered surfaces is has known an important development in order to understand the complex mechanisms that are present on electrocatalysis. In this way, it might be possible to improve or create new technologies that will be relevant in the future.

1.2 General views about Platinum and Palladium

1.2.1 Platinum

This metal was used by pre-Columbian Indians to made many little artifacts with gold-platinum alloy. But the first references about platinum only appear in Europe during the XVI century. It was first mentioned in the writings of famous Italian scholar and poet, Julies Caesar Scaliger, with the observation of the unknown noble metal. But the credit of discovery was for Don Antonio de Ulloa. He was a Spanish mathematician, naval officer and traveler. Two years after his return from a mission in Peru and Equator in 1746, he published a report giving a brief but definite description of platinum[11].

Platinum (Pt) is a chemical element which the name is derived from Spanish term platina, translated into “little silver”, sometimes mistaken for silver (Ag). It is a member of group 10 in the periodic table of elements with atomic number equal to 78. It is an extremely rare metal occurring at an average concentration of only 0.005 ppm in Earth’s crust. In 2010, South Africa was the top producer of Pt, with an almost 77% share, followed by Russia at 13%. World production in 2010 was 192.000 Kg.

Platinum is a noble metal. It is generally non-reactive, exhibits a remarkable resistance to corrosion, even at high temperatures, and is resistant in acidic medium. It is the most studied metal in electrochemistry due to its remarkable properties as electrocatalyst. There is countless research work with different purposes based on platinum, as for example on the influence of the crystallography planes on the electro-catalytic activity [12–14], on the properties of nanoparticles[15,16], on the oxidation of organics[14–17], on platinum as substrate for metallic films[18–20].

1.2.2 Palladium

This noble metal (Pd) was discovered by William Hyde Wollaston in July 1802, but he only named it palladium in his lab-book in August[21–24]. The name was derived from the asteroid Pallas, which was discovered in the same year and counted as a planet. Pallas was a daughter of Triton in Greek mythology and she did allusion to

wisdom[21,24,25]. As platinum, this element is a member of the group 10, with atomic number equal to 46. Currently, palladium is largest used in catalysis, being a versatile catalyst accelerating the reaction of hydrogenation and dehydrogenation[26–31]. In 2011, the largest producers of palladium were Russia and South Africa with 46 and 35% of world production, respectively.

The following table highlights the main physical properties of Pd and Pt. We remark that the two metals have the same face centered cubic (fcc) crystal structure and similar atomic radius.

Properties	**Pd**	**Pt**
Atomic Number	46	78
Atomic Weight	106.42	195.08
Electronic Configuration	$[Kr]4d^{10}$	$[Xe]4f^{14}5d^{9}6s^{1}$
Atomic Radius / Å	1.37	1.38
Density / $g \cdot cm^{-3}$	12.02	21.45
Electrical Resistivity (20°C) / nΩ·m	105.4	105.0
Melting Point / °C	1554.9	1768.3
Crystal Structure	Face-centered cubic	Face-centered cubic

Table 1.1 : Properties of Pd and Pt.

The ability of palladium to catalyze a wide variety of heterogeneous reactions is well documented[1]. The propensity of this metal to absorb unusually large amounts of hydrogen is also widely known[32,33]. The investigations on the surface electrochemical properties of palladium have revealed unique phenomena that serve to further establish the remarkably rich interfacial chemistry of this material. Such chemistry may have its origins in the anomalously weak intermetallic palladium-palladium bond: The dissociation enthalpy for Pd-Pd is very low $\left(\Delta H^0_{diss} = 100\ kJ \cdot mol^{-1}\right)$ compared to other metals in the same group (group 10): Ni-Ni $\left(\Delta H^0_{diss} = 203\ kJ \cdot mol^{-1}\right)$; Pt-Pt $\left(\Delta H^0_{diss} = 357\ kJ \cdot mol^{-1}\right)$. Such anomalous behavior is expected to explain the relative facility to break the Pd-Pd bond, the enhancement of the surface mobility and the facility of substrate-adsorbate bonds[34].

1.3 Crystallographic Structure

In the crystalline solids the atoms have an ordered arrangement. They are formed by a periodic sequence of unit cells. The knowledge of physical properties about any arbitrary unit cell in ideal crystals implies their knowledge within any other unit cell. Polycrystalline materials are solids that are composed of many crystallites of varying size and orientation. The long-range order is broken, although a short-range order is still present on a local microscopic scale[35].

1.3.1 Lattice Systems

A crystal may be defined as a solid composed of atoms arranged in a pattern periodic in three dimensions[36]. Describing a crystal, a set of points (point lattice) is considered, so that each point has identical surroundings. This division of space will produce a set of cells each identical in size, shape and orientation to its neighbors. Unit cell is completely described by three vectors (a, b, c) and three angles (α, β, γ). Figure 1.2 shows a unit cell with its lattice parameters.

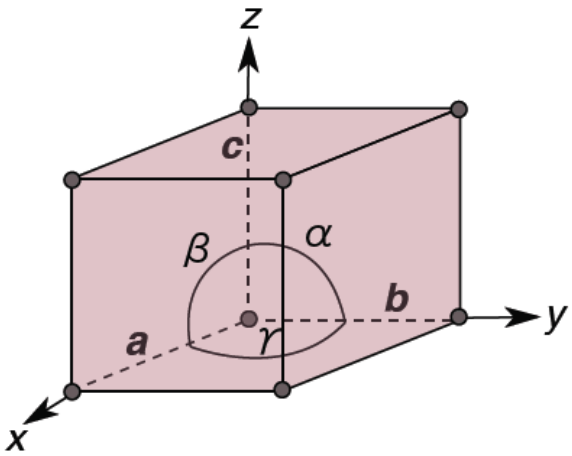

Figure 1.2 : General unit cell with lattice parameters.

Only seven different kinds of cells are necessary to include all the possible point lattices: these correspond to seven crystal systems into which all crystals can be classified (triclinic; monoclinic; orthorhombic, tetragonal; rhombohedra; hexagonal; and cubic). The French crystallographer Bravais showed that only fourteen point lattices are possible. The fourteen Bravais lattices are shown in Figure 1.3.

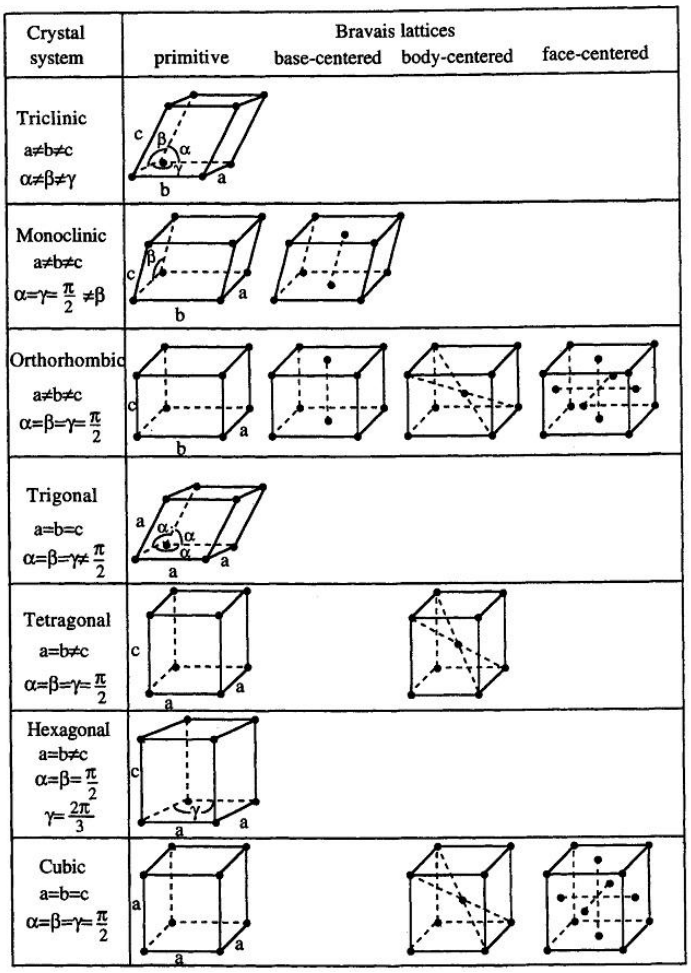

Figure 1.3 : Classification of the fourteen Bravais lattices into the seven crystal systems. The conventional parallelepiped cells are shown[35].

Both platinum and palladium are described by the fcc crystalline lattice, as shown in Figure 1.4 (A).

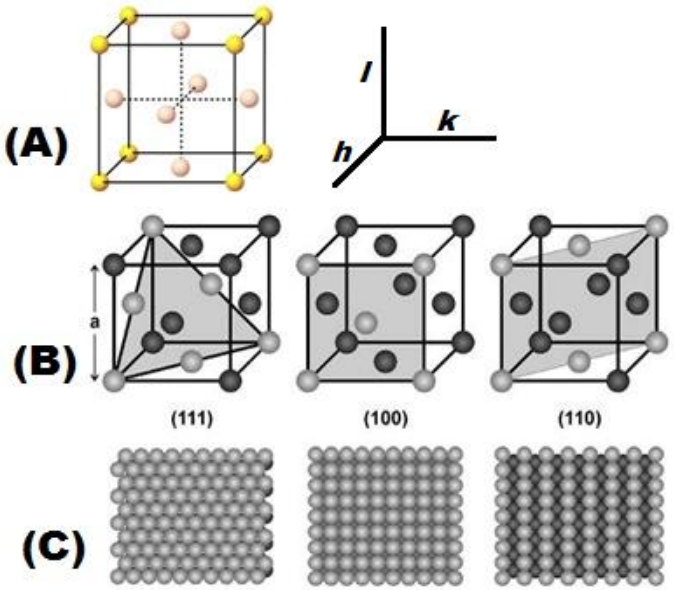

Figure 1.4 : (A) Crystalline lattice fcc ; (B) Crystallographic orientation ; (C) view of the surface plane[10]. The Miller indices are shown as well.

The lattice parameter for Pt and Pd are 3.92 Å and 3.89 Å, respectively. Figure 1.4 (B) shows different surface orientations of the same unit cells. They exhibit different atomic arrangements at the surface as shown by Figure 1.4 (C). In other words, the same crystalline lattice has different surface structures. They are more or less packed, depending on the atomic arrangement. This surface orientation is described by the Miller indices (William Hallowes Miller, British researcher having defined the indices in his "*Treatise on Crystallography"*, 1839). The method consists of describing the atomic planes in a crystal lattice using the Miller index notation (*hkl*). The *h*, *k*, and *l* are directional indices linked to atoms intercepts on the primitive axes[37].

1.3.2 Adsorption sites

A direct relationship between reactivity and surface arrangement was extensively studied since the early single crystal surface preparation[12]. It has been shown that several important surface reactions are directly sensitive to atomic arrangement[14,18,19,38–42].

Figure 1.5 shows the relationship between the different adsorptions sites and the surface planes (111) and (100) (in this work we will consider these orientations for the Pt substrate).

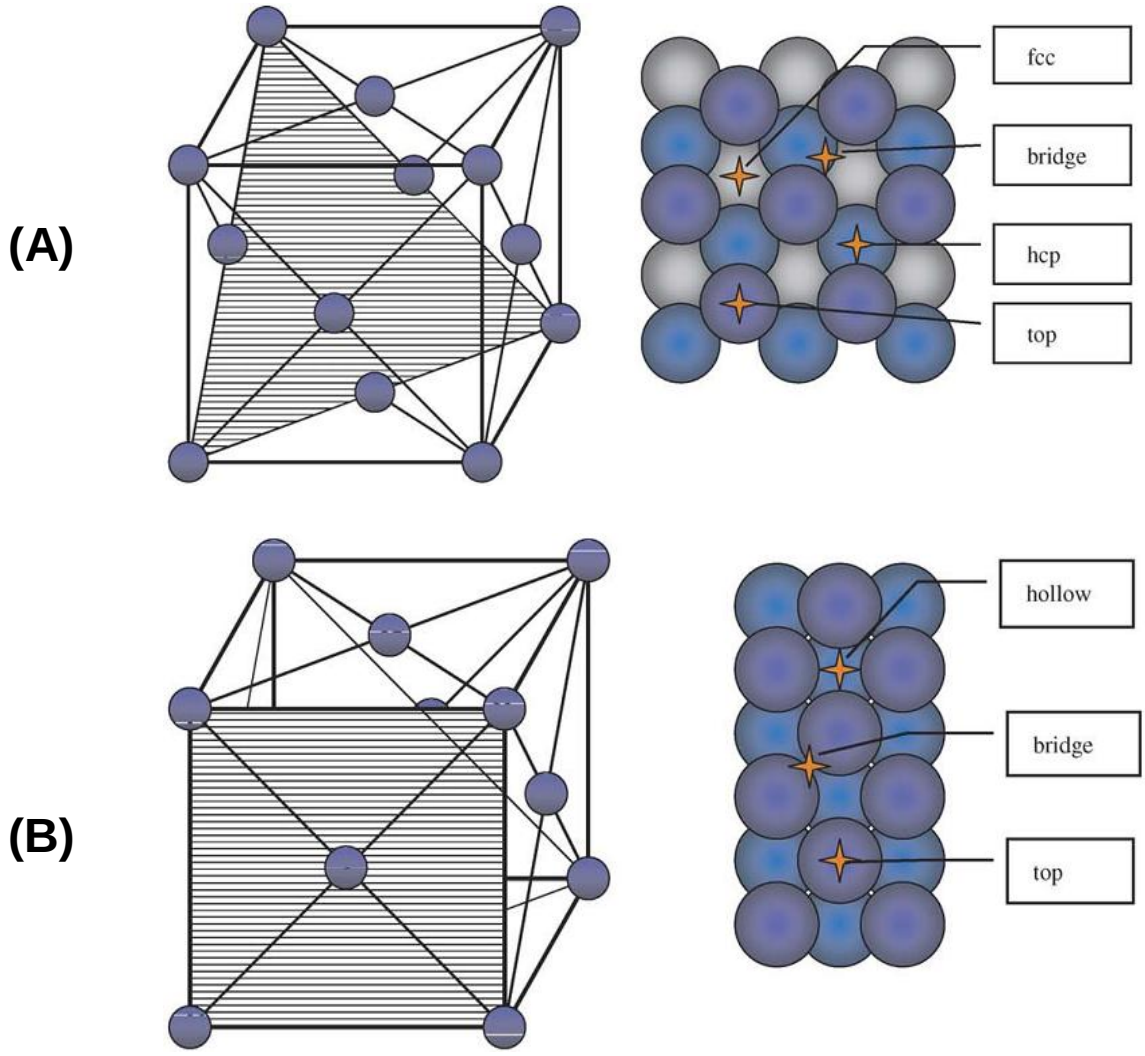

Figure 1.5 : Unit cell FCC (left) and surface view (right) with adsorptions sites: (A) (111)plane and (B) (100)plane[31].

The presence of particular adsorption sites depends on the surface orientation. This can interfere directly on the surface reactions, facilitating or hindering the species adsorption.

1.4 Hydrogen Adsorption as a surface probe

Hydrogen electro-adsorption reaction on metals is a fundamental process in electrocatalysis that has been extensively studied[34,43–45]. It occurs at potentials close

to 0 V *vs*. RHE (Reversible Hydrogen Electrode) and it is described by the following equation:

$$H^+ + e^- \rightleftarrows H_{ads} \qquad \textbf{(Equation 1.1)}$$

This reaction shows different behaviors depending on the considered surface. Theoretical studies[31,46] have for example shown that the hydrogen adsorption energy has different values in the various adsorption sites. Hydrogen adsorption not only occurs at potentials more or less positive depending on the metal of the substrate, but its behavior (ex. quantity of adsorbed hydrogen) strongly depends on the substrate's orientation as well. For this reason hydrogen can be used as a probe in order to to identify the surface profile.

Pt single crystal surfaces are the subject of numerous studies related to the influence of orientation on voltammetric profiles. In this work we will consider two surface orientations, Pt(111) and Pt(100). The first one is a more compact and stable surface compared to the second one. (see Figure 1.4)[10,47].

It is interesting to consider the different behaviors of hydrogen adsorption on the two surface orientations.

1.4.1 Pt(111)

Figure 1.6 presents the voltammetric profile of Pt(111) in sulfuric acid.

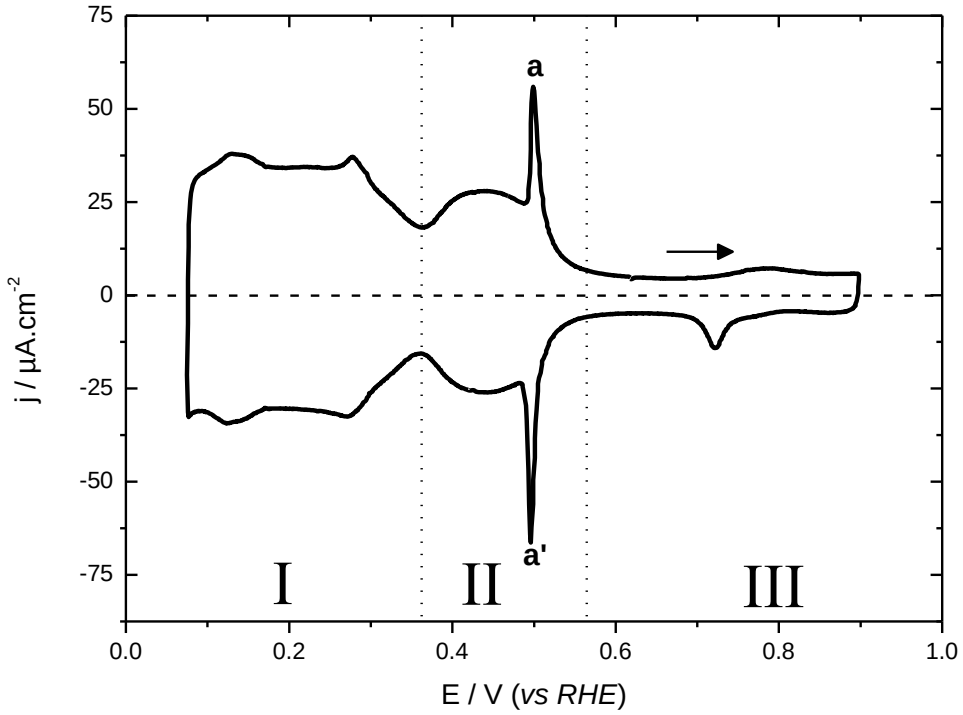

Figure 1.6 : Voltammogram of Pt (111) in 0.1 M H_2SO_4 at 50 mV·s^{-1}.

The voltammogram of Pt(111) exhibits 3 distinct zones (I, II, III) separated by dashed lines.

The first zone (I) corresponds to the hydrogen adsorption region. There is a large plateau associated with small peaks. These peaks are caused by hydrogen adsorption on others orientations than (111) in the crystal side. The contribution of other faces than (111) is due to the experimental hanging meniscus method used for these measurements, where the lateral faces of the single crystal may be partly in contact with the electrolytic solution (see chapter 2, paragraph 2.1.1). The charge density evaluated after the subtraction of the double layer contribution is equal to 162.2 µC·cm^{-2}, corresponding to approximately 0.67 monolayer. This corresponds to a coverage rate of 2 H for 3 Pt atoms[34,48–50]. We recall that one complete monolayer of hydrogen on Pt(111) (one H per Pt atom and one electron exchanged) corresponds to 240 µC·cm^{-2}.

Region II is attributed to (bi)sulfate adsorption. The reversible pronounced spike (a;a') has been attributed to a phase transition of the adsorbed anions (SO_4^{2-}

and HSO_4^-)[48–51]. It is characteristic of the (111) platinum orientation and its presence confirms the absence of contaminants in the solution.

Region III corresponds to the double layer contribution. The two irreversible peaks are attributed to specific anions adsorption[52].

1.4.2 Pt (100)

The cyclic voltammogram profile of the Pt (100) surface in sulfuric acid medium is shown in

Figure 1.7.

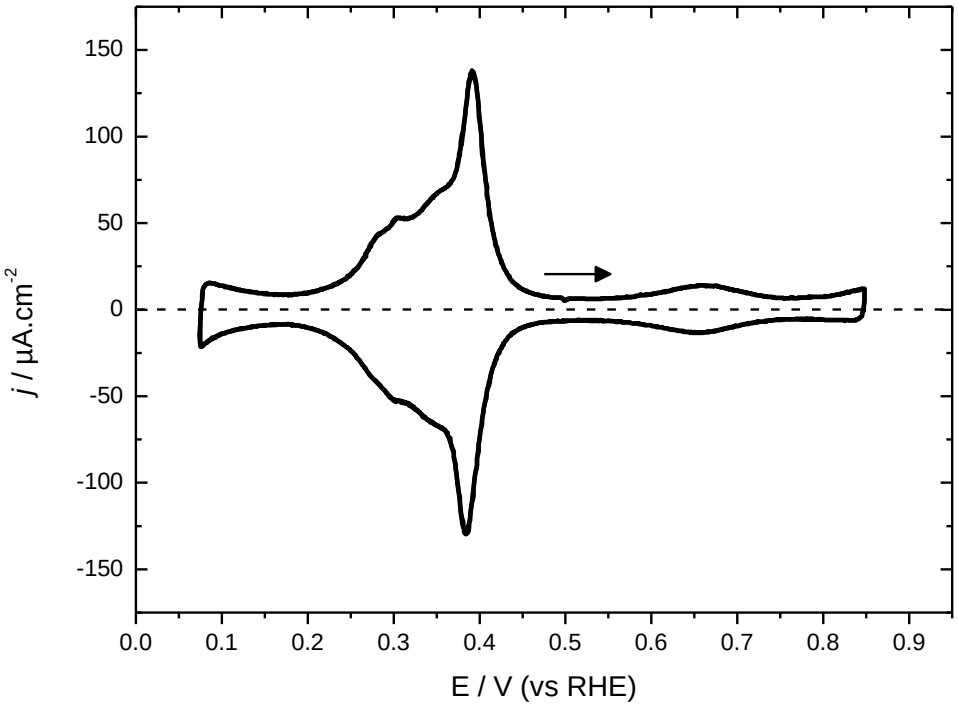

Figure 1.7 : Voltammogram of Pt (100) in 0.1 M H_2SO_4 at 50 $mV \cdot s^{-1}$.

Two reversible peaks at 0.39 V *vs.* RHE are clearly identified, characteristic of a well-ordered Pt(100) surface, and corresponding to specific anions adsorption on the terraces[13,53–56]. The charge calculated after the subtraction of double layer contribution is 204 $\mu C \cdot cm^{-2}$. This value is very close to that of one layer of hydrogen adsorbed on the Pt(100) surface (209 $\mu C \cdot cm^{-2}$)[40].Two other less well defined peaks are seen at lower potentials. These peaks (~0.39 and ~0.30 V vs. RHE) are

connected with a reconstruction of the surface. The peaks at 0.30 V *vs.* RHE have been attributed to hydrogen adsorption on the steps of the surface[56].

Two phases, the reconstructed Pt(100)-hex-R 0.7° one and the unreconstructed Pt(100)-(1 X 1) one, are possible for the Pt(100) surface. The reconstructed phase is stable and its surface energy is lower than the unreconstructed surface energy by about 0.12 eV per (1 x 1) unit cell[57]. Nevertheless the kind of reconstruction obtained depends strongly on the substrate preparation and on the thermal history. For instance, if the sample is heated up to 1000 K during 5 min and then cooled down to RT, small domains of the unrotated Pt-hex phase cover the surface with no traces of rotated domains cell[57]. Attard et al.[55,56] have studied Pt(100) surface reconstruction in ultra-high-vacuum (UHV) with low-energy electron diffraction analysis (LEED) and with cyclic voltammetry. The authors prepared the reconstructed surface by repeated cycles of bombardment with argon ions in presence of oxygen to avoid contamination (10^{-6} mbar and 1300 K). The Pt(100)-(1 X 1) phase was prepared by adsorbing CO onto the hex-surface. This treatment was followed by CO oxidation and removal in the presence of O_2 (10^{-8} mbar and 380 K). Figure 1.8 shows the images of the different Pt(100) reconstructed.

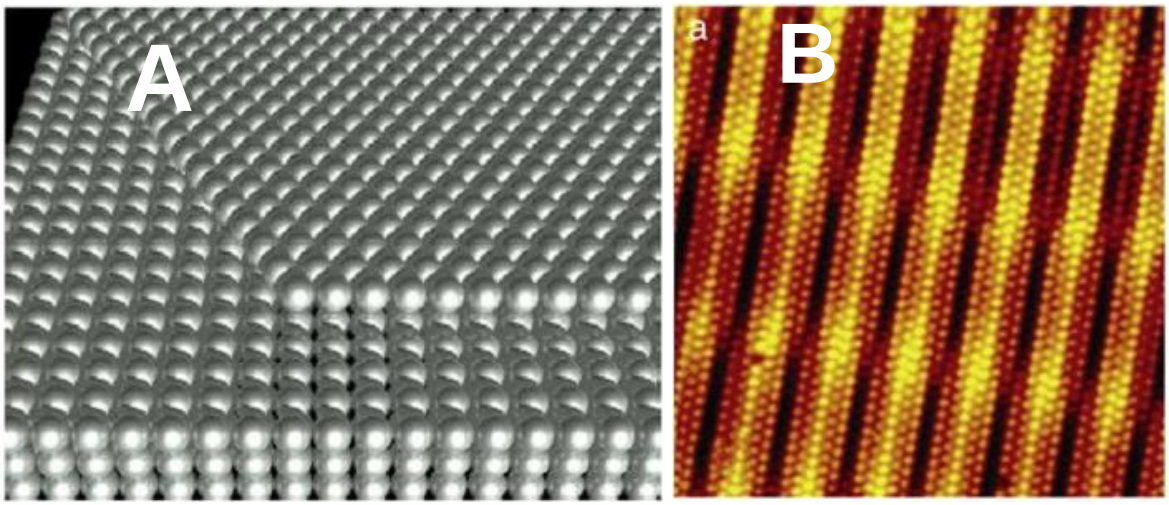

Figure 1.8 : (A) representative scheme of the hex-reconstructed layer on top of the Pt(100)-(1x1) structure[58]. (B) STM image (110 Å × 100 Å) of the Pt(100)-hex-R 0.7° reconstructed[59].

Both surfaces prepared in UHV have been transferred to the electrochemical cell for characterization in H_2SO_4. The authors could clearly show that the hydrogen adsorption peak at 0.39 V vs. RHE corresponds to a good two-dimensional long

range order of the unreconstructed phase. In the presence of the Pt(100)-hex-R 0.7° phase, the magnitude of the peak at 0.30 V *vs.* RHE increases, signature that the extent of the two-dimensional long range order is much reduced compared to Pt(100)–(1x1), as shown in the Figure 1.9.

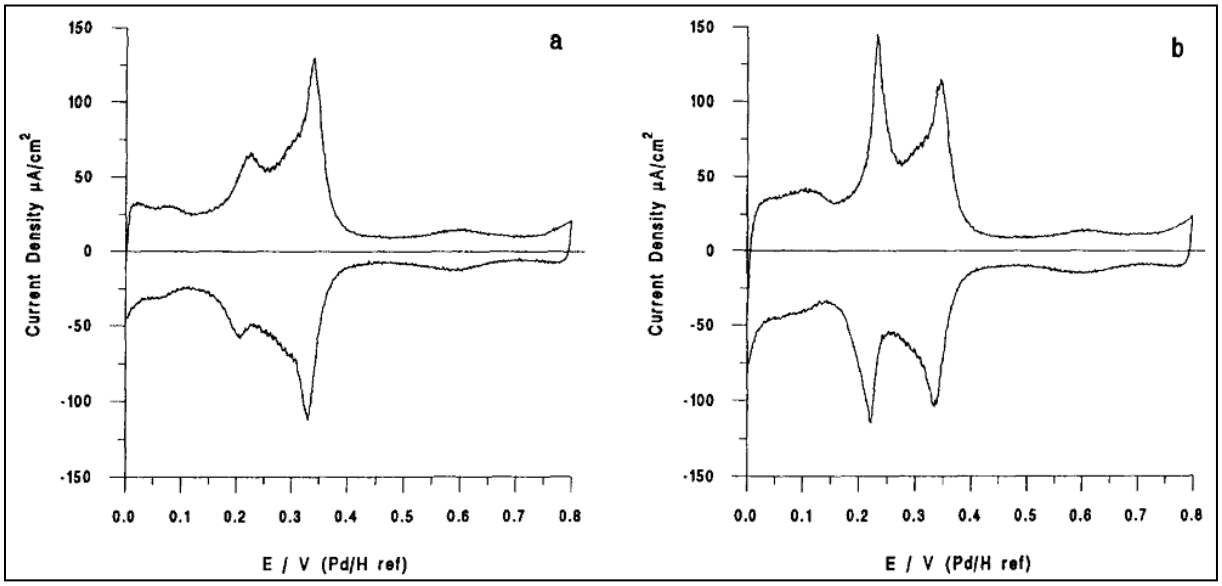

Figure 1.9 : Cyclic voltammograms of UHV prepared (a) Pt(100)-(1 × 1) and (b) Pt(100)-hex-R0.7° electrodes in 0.1 M H_2SO_4, sweep rate 50 $mV \cdot s^{-1}$.[56]

Unlike Pt(100)/vacuum interface, the electrolyte interface was found to be unreconstructed at all potential in 0.1 M KOH , 0.1 M H_2SO_4 and $HClO_4$ [60]. Batina et al.[61] studied the stability of the reconstructed Pt(100) surface in sulfuric acid solutions. These authors also concluded that the hexagonal structure seems to be easily lost upon contact with an electrolyte, where specific adsorption of anions such as bisulfate switches the reconstructed phase to Pt(100)-(1x1).

We recall that in electrochemistry the Pt single crystal surface is typically reorganized using the flame annealing method[12,62]. The crystal is then cooled down in a controlled reductive atmosphere in order to avoid contamination by easily adsorbed molecules. According to the literature[10,63], the atmosphere for cooling down has a direct influence on the surface organization. For example, steps in the (100) surface can be formed if oxygen is thermally adsorbed[13,52,54,61].

As a conclusion, we have shown that there are characteristic voltammetric profiles for each Pt orientation. Using hydrogen as a probe, the electrochemical characterization of the Pt(111) and Pt(100) surfaces allows checking the surface orientation and the absence of contaminations.

1.5 Palladium Nanofilms

The electrochemical deposition of a metal onto a foreign substrate plays a key role in many fields, such as surface chemistry, electrocrystallisation or electrocatalysis. Several parameters are governing the deposition process including applied potential, addition of halides but also the nature of the substrate. Understanding the mechanisms of the deposit growth is very important in building reaction models and then enhancing the kinetic of deposition and the quality of the deposited layer.

Palladium is probably the most studied pure metal able to reversibly absorb hydrogen. Moreover, it acts as a catalyst for hydrogen dissociation and is characterized by a high insertion/desorption kinetic. Compared to bulk Pd, the nanometric size of ultra-thin films is expected to induce deep modifications on the electro-catalytic properties, due to the high ratio between atoms on the surface and in the bulk.

Several studies have been made on palladium deposition onto single crystals, like Pt(hkl)[18,19,56,65–71], Au(hkl)[29,71–78], W(hkl)[79,80], Rh(hkl)[81–83], Ru(hkl)[84] and Ta(hkl)[85]. The type of metallic support and its orientation have a great influence on the films characteristics (structure, electro-catalytic properties,…).

1.5.1 Electrocatalytic properties of Pd/Pt(100) nanofilms

The presence of hetero metallic adlayers can deeply change the electro-catalytic properties of a surface. Indeed, the substrate may induce significant geometric and electronic effects altering the physical and chemical properties of the surface layers. Kibler et al.[86]report the behavior of the hydrogen adsorption and formic acid electro-oxidation for one pseudomorphic Pd layer on different singles crystals, like Au(111), Pt(111), Rh(111), Pd(111),… The catalytic activity varies dramatically as a function of the substrate, due to the different lateral compression or dilatation undergone by the Pd epitaxial layer. The authors revealed a linear correlation between the potentials of hydrogen desorption and the shift of the d-band center of the transition-metal substrates, in agreement with theoretical predictions[87].

Formic acid oxidation

Pd/Pt(100) thin films lead to a considerable enhancement of formic acid oxidation rates[18]. Baldauf et al.[71] measured for this system current densities higher than for massive Pd(hkl), for Pd/Pt(111) and for Pd/Au(hkl) films. Such behavior has been observed up to about Pd_{3ML}/Pt(100), while cyclic voltammograms recorded for higher thicknesses are in very good agreement with the curve for massive Pd(100). Pd/Pt(100) films present a particularly high resistivity against CO poisoning, nicely contrasting with Pt(100) for which CO deactivation during formic acid oxidation is catastrophically fast.

CO oxidation

Unlike for direct oxidation of formic acid, the presence of palladium on the Pt(100) surface has a negative effect on the oxidation of adsorbed CO[53]. This lack of activity for CO oxidation suggests that the active intermediate reaction path in formic acid oxidation does not involve any participation of adsorbed CO.

Hydrogen insertion

Ball et al.[88] observe the enhancement of hydrogen insertion upon CO adsorption onto Pd/Pt(100) multilayers, as shown with *in situ* SXRD by the significant expansion of the Pd layers interplanar distance.

1.5.2 Deposition methods for Pd onto Pt single crystal

Several Pd deposit methods have been considered in the literature, like spontaneous deposition, vacuum evaporation, forced deposition and electrochemical deposition. The different methods are briefly described below.

Spontaneous deposition

Pd chemical reduction on the surface occurs with a simple immersion of the single crystal in a solution containing a palladium salt. The time of immersion of the electrode determines the thickness of the Pd deposition[19,48,89].

Vacuum evaporation

Vacuum evaporation is more complex in its implementation because it requires the use of an UHV system associated with another surface technique. The deposition occurs with metal evaporation in UHV conditions. This is obtained heating through a tungsten filament a high purity palladium wire. The amount of deposited Pd can be monitored by Auger spectroscopy[90,91].

Forced deposition

This method is another way to obtain Pd deposition through a chemical reduction. A droplet of solution containing Pd^{2+} is put on the top of the substrate and the reduction is obtained in the presence of a reducing gas flow (Ar + H2). The amount of deposited Pd is known by the Pd concentration in the drop[18,19,89].

Electrochemical deposition

Pd electrochemical deposition presents the advantage to be relatively simple in its implementation. It is reproducible and allows a good control on the amount of Pd deposited on the surface of an electrode.

Typically, two methods are considered for the electroplating: electrochemical cycling and cathodic sweep.

In the electrochemical cycling method the crystal is typically immersed in a H_2SO_4 solution containing a Pd salt, like $PdSO_4$, PdO or H_2PdCl_4, in different concentrations. Pd deposition is obtained by cycling the potential in the region corresponding to Pd deposition with a scan rate typically equal to 50 $mV \cdot s^{-1}$. The Pd amount deposited increases with the number of cycles, but it cannot be directly measured by coulometry. It can be only monitored through the evolution of the voltammetric profile with Pd film thickness. The amount of deposited Pd can only be calculated up to the first deposited layer, thanks to the presence of specific hydrogen adsorption peaks present in the voltammetric characterization[53,65,68–71,92–96].

The second method, adopted in the present work, consists of depositing Pd by negative scan with a quite slow scan rate, typically 0.1 $mV \cdot s^{-1}$. The amount of deposited Pd is controlled by coulometry, where the integrated charge is directly linked to the number of deposited Pd atoms (two exchanged electrons for each reduced Pd atom).

We will show in chapter 2 (paragraph 2.3) that the choice of the deposition method can deeply change the growth mechanisms, in particular for Pd/Pt(100).

1.6 Pd/Pt(100) nanofilms

Pd deposition onto Pt(100) has been poorly studied[18,19,53,56,88].

Llorca et al.[19] used forced deposition method to obtain Pd films on Pt(100). The solution in the droplet contained 0.5 M H_2SO_4 solution with Pd^{2+} ions in the range 10^{-5}–10^{-3} M. The characterization in 0.5 M H_2SO_4 showed the growth of a reversible adsorption/desorption pair of reversible peaks at around 0.17 V *vs*. RHE up to 0.5 ML (see Figure 1.10).

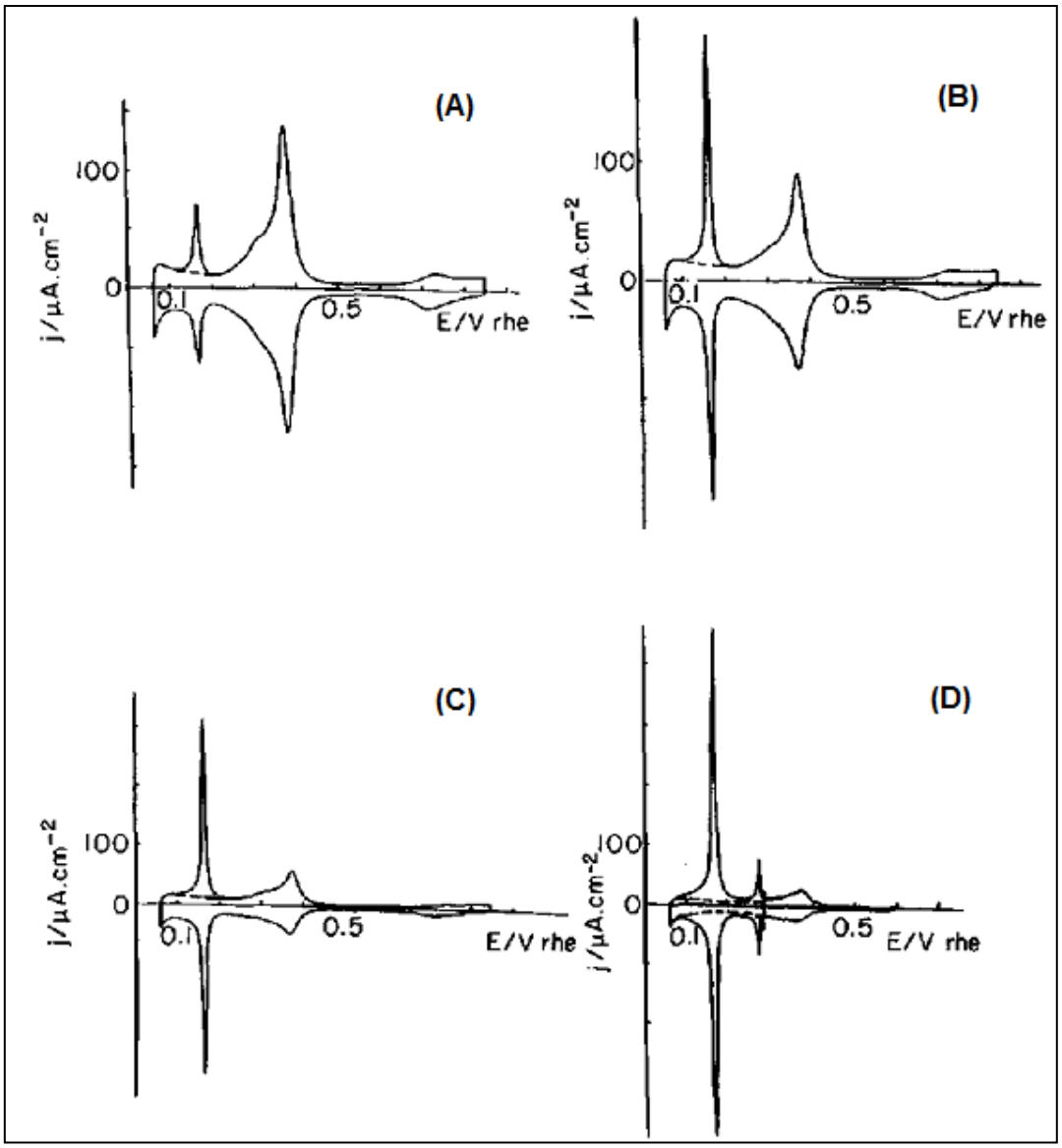

Figure 1.10 : Voltammetric behaviour of irreversibly adsorbed palladium on Pt(100) at various coverages in 0.5 M H_2SO_4 at 50 $mV \cdot s^{-1}$. Coverage is (A) 0.17, (B) 0.40, (C) 0.50 and (D) 0.83.[19]

They have been ascribed to the competitive adsorption/desorption of hydrogen and sulphuric anions on the first Pd layer. The role of sulphate is confirmed by the comparison with the voltammogram obtained in $HClO_4$ 0.1 M, where the sharp peak profile observed in acidic media is transformed in a broader state. With the increase of the coverage, a new adsorption state appears at 0.27 V *vs*. RHE, attributed to the same adsorption/desorption process on the palladium atoms of the second and layer. Such results indicate that the growth of the second layer begins before the completion of the first Pd layer. Electrochemical annealing with cycling allows smoothing the Pd surface, suggesting a lower stability of the atoms in the position of

the second layer. The signature of the first Pd layer is still present up to about Pd_{10ML}/Pt(100), corresponding to an important heterogeneity of the adlayer thickness.

The same authors made CO charge displacement experiments to describe the behaviour of the potential zero total charge (pztc) of the electrode as a function of the Pd coverage. Such value corresponds to the potential at which the total charge density at the electrode surface vanishes. They observed a negative shift of the pztc after Pd deposition, from about 0.4 V vs. RHE down to about 0.2 V vs. RHE at $Pd_{0.8ML}$/Pt(100). Such behaviour was confirmed by *in situ* infrared spectra and indicates a shift of the onset of anion adsorption towards less positive potentials.

The three-dimensional growth of Pd on Pt(100) is confirmed by Alvares et al.[53] for Pd films deposited with electrochemical cycling in 10^{-5} M $PdSO_4$ + 0.1 M H_2SO_4. To obtain a single palladium layer, the authors suggest to resort to electrochemical annealing or to adsorption and reductive stripping of a NO layer.

The epitaxial growth of Pd/Pt(100) is suggested by infrared reflection absorption for the first Pd layer[97] and by *in situ* Fourier Transform infrared spectroscopy[98] experiments for the following layers.

Ball et al.[88] examined the morphology of electrochemically deposited Pd films on the Pt(100) surface through the combination of cyclic voltammetry and *in situ* Surface X-Ray Diffraction (SXRD). The single crystal surface was immersed in H_2SO_4 0.05 M containing 10^{-5} M PdO, Pd being deposited while sweeping the potential at 20 $mV \cdot s^{-1}$. They confirmed the pseudomorphic growth of the Pd layers, at least up to about 7ML. They indicated that the formation of three dimensional islands began to take place prior to the completion of the first monolayer, in agreement with their voltammetric studies. Figure 1.11 summarizes schematically their finding on the Pd films structure as a function of the thickness. The SXS (Surface X-Ray Scattering) results show that in the presence of a monolayer of adsorbed hydrogen the Pt–Pd spacing for Pd_{1ML}/Pt(100), is expanded by ~2% compared to the bulk Pt–Pt spacing. This expansion is similar to that observed for the clean Pt surface. With higher Pd coverage, after 2 ML, the Pd film adopts the bulk Pd(100) lattice spacing.

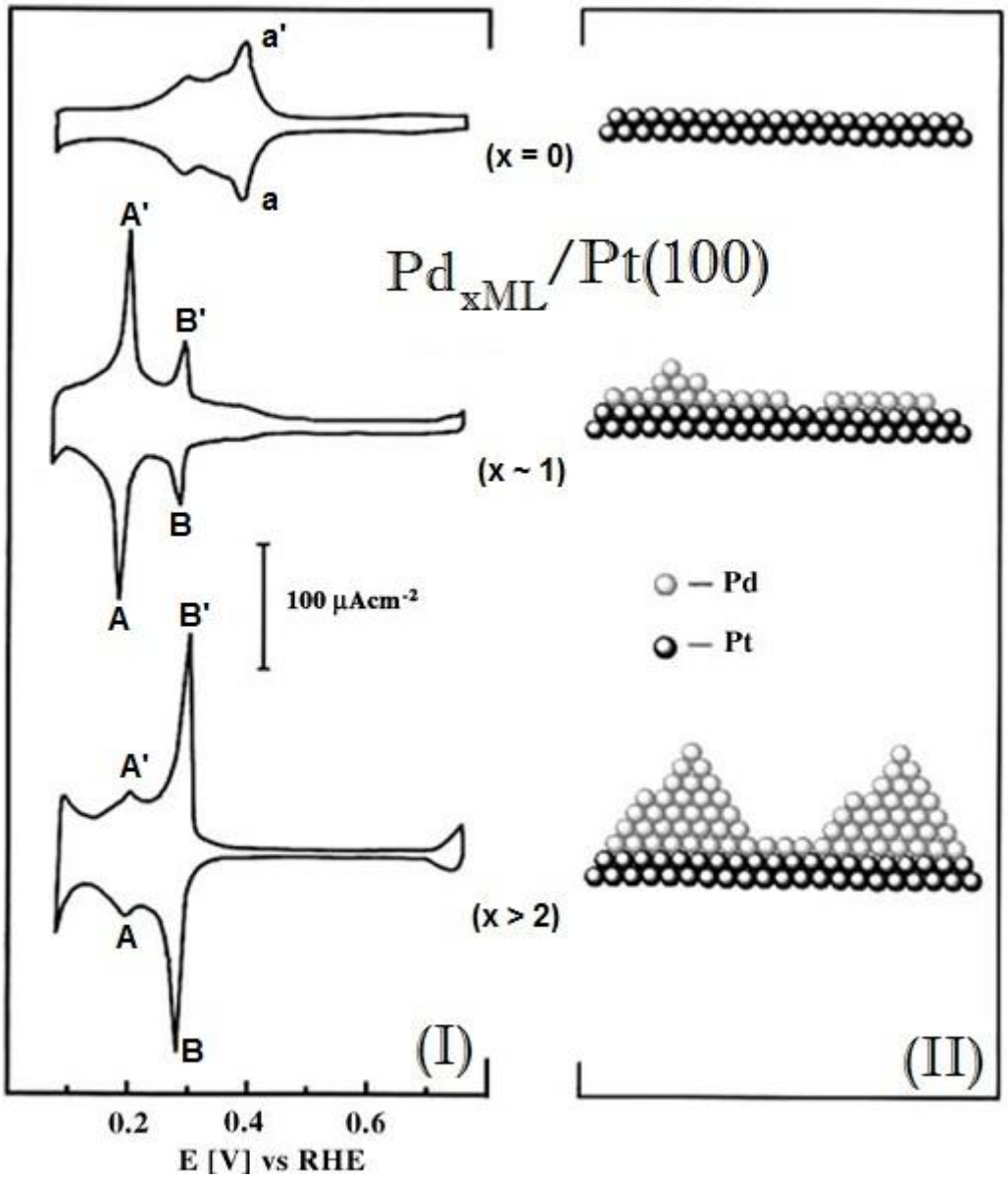

Figure 1.11 : Pd/Pt(100) in 0.05 M H_2SO_4, 20 mV·s^{-1}. (I) evolution of the Pd deposition; (II) schematic of the Pd/Pt(100) structure analyzed by *in situ* surface X-ray scattering (SXS).[88]

Attard et al.[56] studied the growth of palladium on a reconstructed and deconstructed Pt(100) electrode in Ultra High Vacuum (UHV) conditions. They characterized the films with Low Energy Electrons Diffraction (LEED), Auger Electron Spectroscopy (AES). After Pd deposition, the sample was transferred into an electrochemical cell containing 0.1 M H_2SO_4 for cyclic voltammetry. In the UHV conditions used to prepare the Pt(100)–(1x1) surface and to evaporate the Pd adlayers, the authors have demonstrated that essentially layer-by-layer growth of palladium takes place up to the second layer. Such result was confirmed with the electrochemical characterization by the behavior of the typical reversible peaks of

hydrogen/anions adsorption/desorption on the first Pd layer and on palladium atoms of the second and following layers. This is not the case for the reconstructed Pt(100)–hex–R0.7° surface, where Pd islands formation was observed before the completion of the first monolayer completion.

1.7 Conclusion

A layer–by–layer growth mechanism has been revealed up to the second layer for Pd evaporation in UHV.

Contrary to these results, the studies on Pd/Pt(100) films obtained via forced deposition or electrochemical cycling in the absence of chloride always show the presence of a three dimensional growth, where the second layer begins to grow before the completion of the first layer. Such findings are revealed using hydrogen and (bi)sulfate adsorption/desorption as a probe with electrochemical characterization in acid solution. In this way it is possible to discriminate between the presence of only the first Pd adlayer or of Pd atoms on the second and following layers.

We will show in the next chapter that actually Pd/Pt(100) growth mode largely depends on the electrochemical deposition method chosen and that the layer-by-layer growth can be achieved up to two layers. In particular, in this thesis we have considered the cathodic sweeping method with very slow potential rates and we have worked with chloride containing deposition solutions.

1.8 References

(1) Somorjai, G. A. *Introduction to Surface Chemistry and Catalysis*; Wiley, 2010.

(2) Smith, H. A. *Journal of Chemical Education* **1937**, *14*, 479.

(3) Lloyd, L. *Handbook of Industrial Catalysts*; Springer US: Boston, MA, 2011.

(4) Prandtl, W. *Journal of Chemical Education* **1950**, *27*, 176.

(5) Campbell, I. M. *Catalysis at Surfaces*; Springer, 1988.

(6) Vassilis, J. I.; Stavros, G. P. *Adsorption, Ion Exchange and Catalysis - Design of Operations and Environmental Applications*; B.V., E., Ed.; 2006.

(7) Kauffman, G. B. *The Chemical Educator* **1999**, *4*, 186–197.

(8) Collins, P. M. D. *Platinum Metals Review* **1986**, *30*, 141–146.

(9) Redhead, P. A. *Journal of Vacuum Science & Technology A: Vacuum, Surfaces, and Films* **1994**, *12*, 904.

(10) Kibler, L. A. *International Society of Electrochemistry* **2003**, 1–55.

(11) Weeks M.E. *Discovery of the Elements*; EDUCATION, J. O. C., Ed.; 6th ed.; Journal Of Chemical Education, 1960.

(12) Clavilier, J.; Faure, R.; Guinet, G.; Durand, R. *Journal of Electroanalytical Chemistry and Interfacial Electrochemistry* **1979**, *107*, 205–209.

(13) Clavilier, J.; Armand, D.; Wu, B. L. *Journal of Electroanalytical Chemistry and Interfacial Electrochemistry* **1982**, *135*, 159–166.

(14) Gomes, J. F.; Busson, B.; Tadjeddine, A.; Tremiliosi-Filho, G. *Electrochimica Acta* **2008**, *53*, 6899–6905.

(15) Antolini, E. *Journal of Power Sources* **2007**, *170*, 1–12.

(16) Venancio, E. *Electrochimica Acta* **2002**, *47*, 1495–1501.

(17) Boscheto, E.; Batista, B. C.; Lima, R. B.; Varela, H. *Journal of Electroanalytical Chemistry* **2010**, *642*, 17–21.

(18) Llorca, M. J.; Feliu, J. M.; Aldaz, A.; Clavilier, J. *Journal of Electroanalytical Chemistry* **1994**, *376*, 151–160.

(19) Llorca, M. J.; Feliu, J. M.; Aldaz, A.; Clavilier, J. *Journal of Electroanalytical Chemistry* **1993**, *351*, 299–319.

(20) Maciá, M. D.; Herrero, E.; Feliu, J. M. *Journal of Electroanalytical Chemistry* **2003**, *554-555*, 25–34.

(21) Griffith, W. P. *Platinum Metals Review* **2004**, *47*, 175–183.

(22) Wollaston, W. H. *Philosophical Transactions of the Royal Society of London* **1804**, *94*, 419–430.

(23) Wollaston, W. H. *Philosophical Transactions of the Royal Society of London* **1805**, *95*, 316–330.

(24) Usselman, M. C. *Annals of Science* **1978**, *35*, 551–579.

(25) Mauskopf, S. H.; McDonald, D.; Hunt, L. B. *A History of Platinum and Its Allied Metals*; Johnson Matthey, 1982; Vol. 25.

(26) Lebouin, C.; Soldo-Olivier, Y.; Sibert, E.; Millet, P.; Maret, M.; Faure, R. *Journal of Electroanalytical Chemistry* **2009**, *626*, 59–65.

(27) Lebouin, C.; Soldo-Olivier, Y.; Sibert, E.; De Santis, M.; Maillard, F.; Faure, R. *Langmuir* **2009**, *25*, 4251–5.

(28) Soldo-Olivier, Y.; Lafouresse, M. C.; De Santis, M.; Lebouin, C.; De Boissieu, M.; Sibert, E. *The Journal of Physical Chemistry C* **2011**, *115*, 12041–12047.

(29) Baldauf, M.; Kolb, D. M. *Electrochimica Acta* **1993**, *38*, 2145–2153.

(30) Vigier, F.; Jurczakowski, R.; Lasia, A. *Journal of Electroanalytical Chemistry* **2006**, *588*, 32–43.

(31) Jewell, L. L.; Davis, B. H. *Applied Catalysis A* **2006**, *310*, 1–15.

(32) Lewis, F. A. *The palladium hydrogen system*; Academic Press Inc., 1967.

(33) Lewis, F. A. *International Journal of Hydrogen Energy* **1996**, *21*, 461–464.

(34) Wieckowski, A. *Interfacial Electrochemistry: Theory, Experiment, and Applications*; Marcel Dekker, I., Ed.; 1999.

(35) Grosso, G.; Parravicini, G. P. *Solid State Physics*; 2nd ed.; Academic Press, 2003.

(36) Cullity, B. D.; Stock, S. *Elements of X-Ray diffraction, , Addison-Wesley publishing company].*; 3a ed.; Addison-Wesley Publishing Company, Inc., 2001.

(37) Linke, U.; Poelsema, B. *Journal of Physics E: Scientific Instruments* **1985**, *18*, 26.

(38) Grozovski, V.; Climent, V.; Herrero, E.; Feliu, J. M. *Journal of Electroanalytical Chemistry* **2011**, *662*, 43–51.

(39) Clavilier, J.; Albalat, R.; Gomez, R.; Orts, J. M.; Feliu, J. M.; Aldaz, a. *Journal of Electroanalytical Chemistry* **1992**, *330*, 489–497.

(40) Garcia-Araez, N.; Climent, V.; Feliu, J. M. *Journal of Electroanalytical Chemistry* **2010**, *649*, 69–82.

(41) Herrero, E.; Buller, L. J.; Abruña, H. D. *Chemical Reviews* **2001**, *101*, 1897–1930.

(42) Herrero, E.; Chrzanowski, W.; Wieckowski, A. *The Journal of Physical Chemistry* **1995**, *99*, 10423–10424.

(43) Conway, B. E.; Gileadi, E. *Transactions of the Faraday Society* **1962**, *58*, 2493.

(44) Gileadi, E.; Conway, B. E.; Bockris, J. . M. *Modern Aspects of Electrochemistry*; Butterworths, 1964.

(45) Conway, B. E.; Tilak, B. V. *Advances in Catalysis*; Academic Press, 1992.

(46) Dong, W.; Ledentu, V.; Sautet, P.; Eichler, A.; Hafner, J. *Surface Science* **1998**, *411*, 123–136.

(47) Marković, N. M.; Ross, P. N. *Surface Science Reports* **2002**, *45*, 117–229.

(48) Attard, G. A.; Bannister, A. *Journal of Electroanalytical Chemistry and Interfacial Electrochemistry* **1991**, *300*, 467–485.

(49) Lasia, A. *Journal of Electroanalytical Chemistry* **2004**, *562*, 23–31.

(50) Blum, L.; Huckaby, D. a; Marzari, N.; Car, R. *Journal of Electroanalytical Chemistry* **2002**, *537*, 7–19.

(51) Funtikov, a. M.; Stimming, U.; Vogel, R. *Journal of Electroanalytical Chemistry* **1997**, *428*, 147–153.

(52) Garcia-Araez, N.; Climent, V.; Rodriguez, P.; Feliu, J. M. *Electrochimica Acta* **2008**, *53*, 6793–6806.

(53) Álvarez, B.; Berná, a.; Rodes, a.; Feliu, J. M. *Surface Science* **2004**, *573*, 32–46.

(54) Rodes, A.; Zamakhchari, M. A.; El Achi, K.; Clavilier, J. *Journal of Electroanalytical Chemistry and Interfacial Electrochemistry* **1991**, *305*, 115–129.

(55) Al-Akl, A.; Attard, G. A.; Price, R.; Timothy, B. *Journal of Electroanalytical Chemistry* **1999**, *467*, 60–66.

(56) Attard, G. A.; Price, R. *Surface Science* **1995**, *335*, 63–74.

(57) Soares, M. M. Growth, structure and magnetism in exchange coupled AF/F systems: Fundamental approach by surface physics, Grenoble University, 2011.

(58) Bobaru, S. C. High-Pressure STM Studies of Oxidation Catalysis, 2006.

(59) Nilsson, L.; Andersen, M.; Bjerre, J.; Balog, R.; Hammer, B.; Hornekær, L.; Stensgaard, I. *Surface Science* **2012**, *606*, 464–469.

(60) Tidswell, I. M.; Marković, N. M.; Ross, P. *Physical Review Letters* **1993**, *71*, 1601–1604.

(61) Zei, M. S.; Batina, N.; Kolb, D. M. *Surface Science* **1994**, *306*, L519–L528.

(62) Clavilier, J. *Journal of Electroanalytical Chemistry and Interfacial Electrochemistry* **1980**, *107*, 211–216.

(63) Kibler, L. a.; Cuesta, A.; Kleinert, M.; Kolb, D. M. *Journal of Electroanalytical Chemistry* **2000**, *484*, 73–82.

(64) Clavilier, J.; Armand, D.; Sun, S. G.; Petit, M. *Journal of Electroanalytical Chemistry and Interfacial Electrochemistry* **1986**, *205*, 267–277.

(65) Hoyer, R.; Kibler, L. a.; Kolb, D. M. *Electrochimica Acta* **2003**, *49*, 63–72.

(66) Llorca, M. J.; Herrero, E.; Feliu, J. M.; Aldaz, A. *Journal of Electroanalytical Chemistry* **1994**, *373*, 217–225.

(67) Ball, M. J.; Lucas, C. A.; Marković, N. M.; Stamenkovic, V.; Ross, P. N. *Surface Science* **2002**, *518*, 201–209.

(68) Marković, N. M.; Lucas, C. A.; Climent, V.; Stamenković, V.; Ross, P. N. *Surface Science* **2000**, *465*, 103–114.

(69) Arenz, M.; Stamenkovic, V.; Schmidt, T. J.; Wandelt, K.; Ross, P. N.; Marković, N. M. *Surface Science* **2002**, *506*, 287–296.

(70) Álvarez, B.; Climent, V.; Rodes, A.; Feliu, J. M. *Journal of Electroanalytical Chemistry* **2001**, *497*, 125–138.

(71) Baldauf, M.; Kolb, D. M. *The Journal of Physical Chemistry* **1996**, *100*, 11375–11381.

(72) Duncan, H.; Lasia, A. *Electrochimica Acta* **2007**, *52*, 6195–6205.

(73) Takahasi, M.; Hayashi, Y.; Mizuki, J.; Tamura, K.; Kondo, T.; Naohara, H.; Uosaki, K. *Surface Science* **2000**, *461*, 213–218.

(74) Naohara, H.; Ye, S.; Uosaki, K. *The Journal of Physical Chemistry B* **1998**, *102*, 4366–4373.

(75) Tang, J.; Petri, M.; Kibler, L. A.; Kolb, D. M. *Electrochimica Acta* **2005**, *51*, 125–132.

(76) Kibler, L. A.; Kleinert, M.; Randler, R.; Kolb, D. M. *Surface Science* **1999**, *443*, 19–30.

(77) El-Aziz, A. M.; Kibler, L. A. *Journal of Electroanalytical Chemistry* **2002**, *534*, 107–114.

(78) Kibler, L. A.; El-Aziz, A. M.; Kolb, D. M. *Journal of Molecular Catalysis A: Chemical* **2003**, *199*, 57–63.

(79) Kołaczkiewicz, J.; Bauer, E. *Surface Science* **1997**, *374*, 95–103.

(80) Kołodziej, J. J.; Pelhos, K.; Abdelrehim, I. M.; Keister, J. W.; Rowe, J. E.; Madey, T. *Progress in Surface Science* **1998**, *59*, 117–134.

(81) Hoyer, R.; Kibler, L. A.; Kolb, D. M. *Surface Science* **2004**, *562*, 275–283.

(82) Beutler, A.; Strisland, F.; Sandell, A.; Jaworowski, A. .; Nyholm, R.; Wiklund, M.; Andersen, J. *Surface Science* **1998**, *411*, 111–122.

(83) Beutler, A.; Sandell, A.; Jaworowski, A. .; Wiklund, M.; Nyholm, R.; Andersen, J. . *Surface Science* **1998**, *418*, 457–465.

(84) Brankovic, S. R.; McBreen, J.; Adžić, R. R. *Surface Science* **2001**, *479*, L363–L368.

(85) Heitzinger, J. M.; Avoyan, A.; Koel, B. E. *Surface Science* **1993**, *294*, 251–264.

(86) Kibler, L. A.; El-Aziz, A. M.; Hoyer, R.; Kolb, D. M. *Angewandte Chemie (International ed. in English)* **2005**, *44*, 2080–4.

(87) Ruban, A.; Hammer, B.; Stoltze, P.; Skriver, H. .; Nørskov, J. . *Journal of Molecular Catalysis A: Chemical* **1997**, *115*, 421–429.

(88) Ball, M. J.; Lucas, C. a.; Marković, N. M.; Stamenković, V.; Ross, P. N. *Surface Science* **2003**, *540*, 295–302.

(89) Clavilier, J.; Llorca, M. J.; Feliu, J. M.; Aldaz, A. *Journal of Electroanalytical Chemistry and Interfacial Electrochemistry* **1991**, *310*, 429–435.

(90) Attard, G. A.; Price, R.; Al-Akl, A. *Electrochimica Acta* **1994**, *39*, 1525–1530.

(91) Han, M.; Mrozek, P.; Wieckowski, A. *Physical Review B* **1993**, *48*, 8329–8335.

(92) Souza-Garcia, J.; Berná, A.; Ticianelli, E. A.; Climent, V.; Feliu, J. M. *Journal of Electroanalytical Chemistry* **2011**, *660*, 276–284.

(93) Álvarez, B.; Rodes, A.; Pérez, J. M.; Feliu, J. M. *The Journal of Physical Chemistry B* **2003**, *107*, 2018–2028.

(94) Álvarez, B.; Climent, V.; Rodes, A.; Feliu, J. M. *Physical Chemistry Chemical Physics* **2001**, *3*, 3269–3276.

(95) Arenz, M.; Stamenkovic, V.; Schmidt, T. J.; Wandelt, K.; Ross, P. N.; Marković, N. M. *Surface Science* **2003**, *523*, 199–209.

(96) Climent, V.; Marković, N. M.; Ross, P. N. *The Journal of Physical Chemistry B* **2000**, *104*, 3116–3120.

(97) Inukai, J.; Ito, M. *Journal of Electroanalytical Chemistry* **1993**, *358*, 307–315.

(98) Gómez, R.; Rodes, A.; Pérez, J. M.; Feliu, J. M.; Aldaz, A. *Surface Science* **1995**, *344*, 85–97.

2 Pd thin films electrodeposited on Pt(100)

This chapter will present the study on the electro-deposition of Pd films onto Pt(100). We will discuss the choice for the various parameters, as the potential interval for deposition and the chloride concentration. Electrochemical characterization of the deposit surface will be shown, as well as an *ex situ* atomic force microscopy (AFM) study. A comparison between Pd/Pt(100) and Pd/Pt(111) nanofilms will be presented as well.

2.1 Experimental

2.1.1 Electrochemical Setup

Two electrochemical cells were used for the Pd films deposition, as represented in Figure 2.1. The double-walled cells made of Pyrex glass allowed the control of the temperature. The two cells had distinct purposes. One was used for the electrochemical characterization and the other one for the Pd electro-deposition.

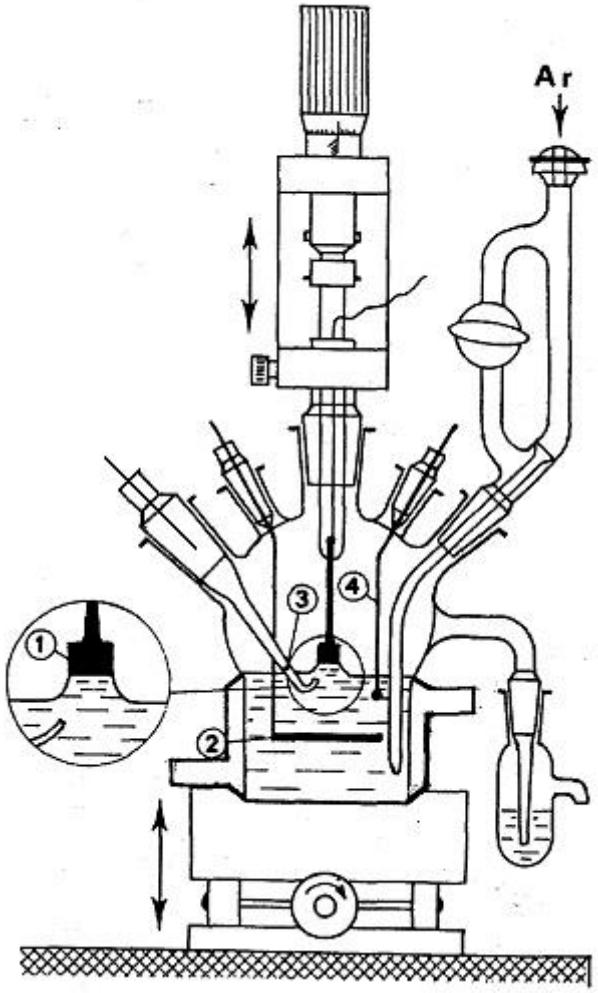

Figure 2.1: Scheme of the electrochemical cell used for Pd deposition. (1) working electrode, (2) counter-electrode, (3) reference electrode, (4) auxiliary electrode.

Working Electrode (WE): a Pt(100) single crystal was used as WE (MaTecK GmbH, diameter 5 mm). The electrode was always handled in hanging meniscus configuration, as shown in Figure 2.1. Such configuration allows the control of the (111) exposed surface, excluding the contribution of the lateral faces.

Counter Electrode (CE) and Auxiliary Electrode (AE): both electrodes were made of polycrystalline Pt. AE is connected to the reference electrode through a capacitive device filtering the electrical noise.

Reference Electrode (RE): A reversible hydrogen electrode (RHE) was used as RE in this study. The advantage of using this type of electrode is that it is less sensitive to possible ions contamination from the deposition solution. It is also well adapted to the type of studied reaction, i.e. hydrogen insertion. A new RHE was prepared before each experiment with 0.1 M H_2SO_4 solution.

The cell was coupled to a PAR 273A potentiostat/galvanostat controlled by CorrWare®software. The temperature control was made by a thermostated water circuit through Thermostats/Cryostats LAUDA RM6. All electrochemical measurements were made at 25 °C. The electrolyte was prepared from H_2SO_4 (Merck, Suprapur), $PdCl_2$ (Alfa Aesar, 99.99%), HCl (Merck, Suprapur) and MilliQ grade ultra-pure water (18.2 MΩ·cm, 3 ppb Total Organic Carbon). Before starting the electrochemical measurements, the electrolyte was purged by bubbling with an Argon 6.0 flux (MESSER).

2.1.2 Pt(100) surface preparation

The absence of contaminations and the well-defined orientation of the surface have both a major influence on the quality of the deposited films. It is therefore necessary to apply a thermal treatment allowing the surface cleaning and regeneration before each measurement. This procedure, firstly developed by Clavilier et al.[1], consists in a flame annealing for few minutes (about 10 min). In the case of platinum single crystals, hydrogen 5.0 (MESSER)/air flame is usually used, as its temperature remains below the melting temperature of this metal (1770 °C). This procedure not only induces the bulk orientation (100 in our case) on the surface layers, but it also eliminates the organic compounds by pyrocatalysis. After heating, the still red crystal is rapidly transferred into a flask containing ultrapure water in a reducing atmosphere composed of argon and hydrogen in the 9:1 ratio (hydrogen 5.0 and argon 5.0, MESSER). This reductive gas mixture prevents the oxides formation

on the crystal during the cooling down process. Oxides formation would induce transformations in the platinum surface planes[2,3]. Cooling down action must be controlled, as the mechanical contractions induced by a too fast procedure (i.e. the crystal touching the water while being too hot) can cause a surface disorganization.

To verify the cleanness and the surface orientation of the Pt(100) electrode, a standard electrochemical measurement was performed and compared with the data in the literature[1–3]. During the transfer to the electrochemical cell dedicated to the surface characterization, the crystal surface was protected by a drop of Milli-Q water, preventing its contamination.

In the characterization cell, the supporting electrolyte was a solution of sulfuric acid 0.1 M. The crystal was introduced at 0.5 V *vs.* RHE in the double-layer region, where no reaction occurs. Current was monitored by chronoamperometry in order to verify its stabilization, corresponding to the fact that the system was ready for the electrochemical characterization.

The electrochemical characterization was performed with a potential sweep from 0.075 V *vs.* RHE up to 0.85 V *vs.* RHE, avoiding the oxide formation zone at higher potential values to prevent surface disorganization (see next paragraph). The potential cycling was performed until reproducibility of the cyclic voltammograms, which was normally obtained after about 5 cycles. The potential sweep rate was 50 $mV \cdot s^{-1}$. The voltammogram corresponding to a clean Pt(100) surface was presented in Chapter 1 (paragraph 1.4.2).

2.1.3 Stability of Pt(100) surface as a function of the potential

In the literature several authors point out the influence of the cooling down procedure after flame annealing on the Pt(100) surface structure. In particular, they underline the fact that oxygen may induce surface irregularities (steps)[3–6]. This happens thermally by adsorbing oxygen or electrochemically by cycling at high oxygen coverages[6,7].

For this reason we decided to study the potential region where Pt(100) surface oxidation occurs. Therewith, we could find the maximum potential value achievable without the occurrence of transformations in the surface state. This value will be considered as the limiting initial potential in the cathodic scan deposition.

We recorded voltammetry cycles of Pt(100) in 0.1 M H_2SO_4. Five cycles were necessary to achieve stability in the voltammogram profile. The higher potential was gradually increased from 0.8 up 1.1 V *vs.* RHE, as shown in

Figure 2.2. The observed profile changes are due to Pt(100) surface evolution caused by oxides formation.

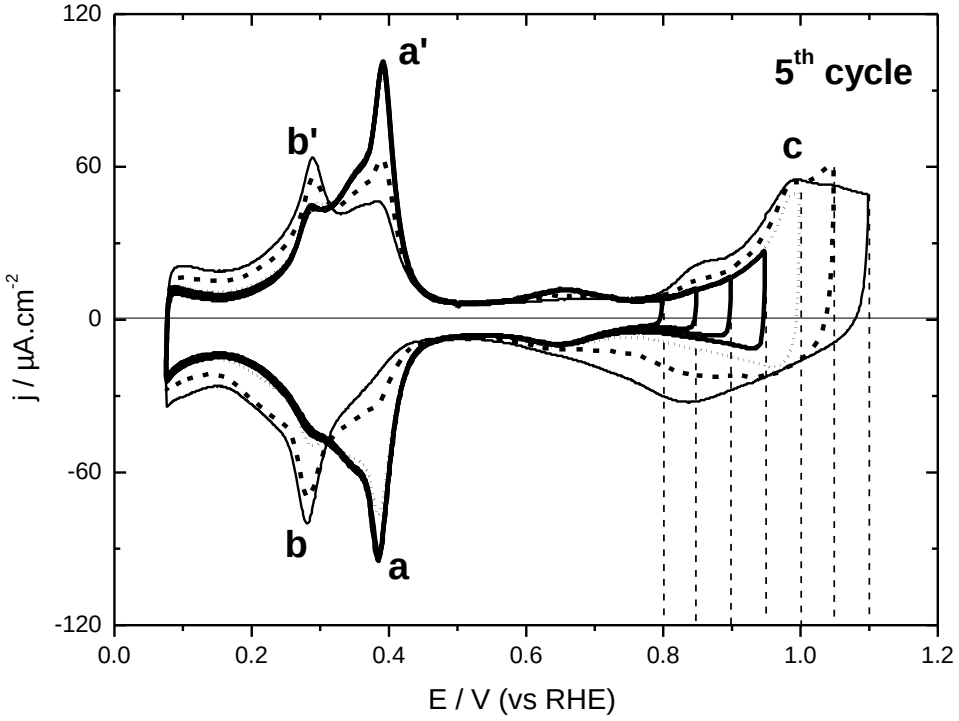

Figure 2.2 : Cyclic voltammetries (only the 5th cycle is shown for each potential limit) for Pt(100) in 0.1 M H_2SO_4, scan rate 50 mV·s^{-1}. Different upper potential limits are shown: 0.8; 0.85; 0.9; 0.95; 1.0; 1.05 and 1.1 V *vs.* RHE.

Three different region called a, b and c, are clearly seen. The peaks a;a' has already been described in chapter 1 (paragraph 1.4.2): they are associated with hydrogen/(bi)-sulfate adsorption/desorption on Pt (100). Peaks b;b' were attributed in the literature to adsorption/desorption on surface steps[3–6,8,9]. Region c is related to oxide formation on the Pt surface.

The voltammogram profile does not change up to 0.95 V vs. RHE. Increasing the upper potential limit beyond this value, the oxide formation in region c is revealed by the growth of a large peak. Correspondingly, peak's a intensity decreases, while peak b rises. Hence, oxide formation induces important changes on the surface, which recedes more and more from the ideal Pt(100) one.

As a conclusion of our study, the potential region beyond about 1.0 V *vs.* RHE must be avoided during Pd deposition. From a practical point of view, no potential higher than 0.95 V *vs.* RHE were applied for all experiments.

2.1.4 Pd electrochemical deposition

After electrochemical characterization, the Pt(100) electrode was transferred into the cell for Pd deposition in deaerated 0.1 M H_2SO_4 + 10^{-4} M $PdCl_2$ + x HCl (x=$3\cdot10^{-3}$ M, $6\cdot10^{-3}$ M, $9\cdot10^{-3}$ M) electrolyte. Pd deposition started after solution bubbling with argon for about 20 minutes. The WE was inserted into the solution for current stabilization at 0.95 V *vs.* RHE. This potential was chosen so that no reaction (oxide formation or Pd deposition) occurs during the WE insertion.

In the intent to get a film as flat as possible, the deposition was made by a negative scan at 0.1 $mV\cdot s^{-1}$ down to the potential corresponding to the diffusion limit of Pd^{2+} ions. The potential was hold at this potential, until the wanted amount of Pd was deposited. Such deposition method were used for Pd deposition onto Pt(111) by Lebouin et al.[10,11] to obtain quite flat pseudomorphic films up to about 10 ML.

The amount of deposited Pd atoms was estimated through the measured coulometry. Assuming a two-electron transfer process and one deposited Pd atom per surface Pt atom, the charge corresponding to one monolayer (Q_{ML}) is equal to 418 $\mu C\cdot cm^{-2}$. The palladium coverage is expressed as an equivalent number x ML of complete monolayers corresponding to the measured charge $Q = x\,Q_{ML}$. As palladium deposition may not follow a layer-by-layer growth mode, x ML does not refer to the real number of deposited atomic layers[11].

It is important to highlight the necessity to work in a well de-aerated deposition solution, in order to avoid contribution from oxygen and correctly estimate the amount of deposited Pd atoms.

After deposition, the crystal was removed from the solution, rinsed with ultra-pure water and transferred back to the characterization cell in 0.1 M H_2SO_4. Palladium film electrochemical characterization was made before each insertion experiment, in order to verify the film quality.

The palladium deposit was removed at the end of each experiment by applying a high potential (~3 V *vs.* RHE) between the counter electrode and the

single crystal in 0.1 M $HClO_4$ for 1 minute. The oxidized film is then dissolved in HCl solution (20% by volume) for about 15 seconds. This operation was repeated three times to ensure the complete removal of palladium.

2.2 Deposition solution

In order to better understand the Pd electro-deposition onto Pt(100), we made a theoretical study about the species present in the deposition solution as a function of the chloride concentration.

2.2.1 Palladium complex

Deposition solutions were prepared from $PdCl_2$ palladium chloride salt. The total initial Pd^{2+} concentration $[Pd^{2+}]_{initial}$ in solution was 10^{-4} M, while different HCl concentrations have been considered, $3{\cdot}10^{-3}$, $6{\cdot}10^{-3}$ and $9{\cdot}10^{-3}$ M. In the presence of chloride ions, several tetravalent complex are present, as $PdCl(H_2O)_3^+$, $PdCl_2(H_2O)_2$, $PdCl_3(H_2O)^-$ and $PdCl_4^{2-}$. For the sake of clarity, water molecules will be removed from complex notation in the following. $PdCl^+$, $PdCl_2$, $PdCl_3^-$ and $PdCl_4^{2-}$ notations will be used. The different species in solution are described by complexation reactions[12] (Equation 2.1):

$$PdCl_{(n-1)}^{(2-n+1)} + Cl^- \overset{K_n}{\Leftrightarrow} PdCl_{(n-1)}^{(2-n)} \qquad \textbf{(Equation 2.1)}$$

$$n = \{1,2,3,4\}$$

The calculated complex concentrations from the equilibrium constants K_n[13] are shown in Table 2.1. The details of the calculation are given in Annex I. The amount of chloride from the $PdCl_2$ salt ($[Cl^-]_{PdCl_2}$ = $2{\cdot}10^{-4}$ M) was added to the HCl concentration. However, we underline that disagreements are present in the literature for values of the equilibrium constants[13–16]. For this reason we will mainly comment the behavior of the calculated quantity and not their absolute value.

Species	$[Cl^-]_{initial}$		
	($3.2\cdot10^{-3}$ M)	**($6.2\cdot10^{-3}$ M)**	**($9.2\cdot10^{-3}$ M)**
$[Cl^-]_{sol}$	*$2.31\cdot10^{-3}$ M*	*$4.78\cdot10^{-3}$ M*	*$7.38\cdot10^{-3}$ M*
$[Pd^{2+}]_{sol}$	*$1.55\cdot10^{-10}$ M*	*$1.62\cdot10^{-11}$ M*	*$3.60\cdot10^{-12}$ M*
$[PdCl^+]$	*$4.50\cdot10^{-7}$ M*	*$9.74\cdot10^{-8}$ M*	*$3.34\cdot10^{-8}$ M*
$[PdCl_2]$	*$4.14\cdot10^{-5}$ M*	*$1.85\cdot10^{-5}$ M*	*$9.82\cdot10^{-6}$ M*
$[PdCl_3^-]$	*$3.03\cdot10^{-5}$ M*	*$2.80\cdot10^{-5}$ M*	*$2.29\cdot10^{-5}$ M*
$[PdCl_4^{2-}]$	*$2.79\cdot10^{-5}$ M*	*$5.33\cdot10^{-5}$ M*	*$6.73\cdot10^{-5}$ M*

Table 2.1 : Calculated concentrations of the various Pd complex species in 0.1 M H_2SO_4 + x HCl solution, x = $3\cdot10^{-3}$, $6\cdot10^{-3}$ and $9\cdot10^{-3}$ M.

The predominant Pd complex are $PdCl_2$, $PdCl_3^-$ and $PdCl_4^{2-}$ for almost all the three chloride concentrations. With the increase of [Cl^-] there is a reduction of $[PdCl_2]$ coupled to the increase of $[PdCl_4^{2-}]$.

Harrison et al.[17,18] studied kinetics of the electro-deposition of Pd in the presence of chloride. They used highly concentrated chloride species, 0.2 M, in the electrolyte. We have estimated (see Annex I) that in this case the $PdCl_4^{2-}$ concentration is close to 100% of the complex species in solution. The authors[15,17] reported that the complex specie effectively reduced at the electrode surface is $PdCl_2$. More in details, they related that the Pd reduction is delayed in a highly concentrated chloride solution, due to the reactions allowing $PdCl_2$ species formation. The slow chemical step shown in (Equation 2.2) is followed by the fast equilibrium expressed by (Equation 2.3) and by the charge transfer indicated in (Equation 2.4)[15,17–19].

$$PdCl_4^{2-} \rightarrow PdCl_3^- + Cl^- \qquad \textbf{(Equation 2.2)}$$

$$PdCl_3^- \leftrightarrows PdCl_2 + Cl^- \qquad \textbf{(Equation 2.3)}$$

$$PdCl_2 + 2\,e^- \rightarrow Pd^0 + 2\,Cl^- \qquad \textbf{(Equation 2.4)}$$

We underline that, unlike to this study, we use a lower chloride concentration in the solution. The deposition mechanisms can therefore be different and in particular different complex species can be involved in Pd deposition.

The potential of zero total charge (pztc) can give interesting indications on the species involved in the adsorption phenomenon. From its value it is possible to deduce which species (cationic or anionic) will be favored in the adsorption process. Attard et al.[20] studied the pztc for Pd on Pt(100) and concluded that the pztc value decreases with Pd coverage increasing. More in details, pztc is equal to about +0.33 V *vs.* RHE for Pt(100) and to about +0.14 V *vs.* RHE for Pd_{1ML}/Pt(100). Alvarez et al.[21] concluded to a similar pztc behavior as a function of the Pd coverage, but pztc value were found equal to about +0.39 V *vs.* RHE for Pt(100) and to about +0.19 V *vs.* RHE for Pd_{1ML}/Pt(100).

However, our Pd deposition procedure never goes below 0.7 V *vs.* RHE, a potential value definitely higher than the pztc value range. Hence the adsorption on the Pt(100) surface of anionic species, $PdCl_3^-$ and $PdCl_4^{2-}$, should be favored. In paragraph 2.3.1, we will discuss the effect of chloride concentration on the Pd electro-deposition.

2.2.2 Thermodynamic Potential

Using the Nernst equation, we have calculated the equilibrium potential between the solution and a bulk Pd electrode. We did the calculation for several chloride concentrations.

We found several values for the standard potential of Pd^{2+}/Pd^0 in the literature[22–27] ranging over about 150 mV. We decided to work instead with $PdCl_4^{2-}/Pd^0$ standard potential, which present a lower distribution (20 mV)[23,25,27]. We decided to choose 0.62 V vs. RHE for the standard potential of $PdCl_4^{2-}/Pd^0$, which gives the best agreement with our experimental potentials.

The calculations have been made for the reduction of $PdCl_4^{2-}$[19], as shown by the following equations:

$$PdCl_4^{2-} + 2\,e^- \underset{\leftarrow}{\rightarrow} Pd^0 + 4\,Cl^- \qquad \textbf{(Equation 2.5)}$$

$$E_2 = E^0_{(PdCl_4^{2-}/Pd^0)} + 0.0296 \log\left(\frac{a_{(PdCl_4^{2-})}}{a^4_{(Cl^-)}}\right) \qquad \textbf{(Equation 2.6)}$$

The activity of metallic Pd, $a_{(Pd^0)}$, is equal to 1. The specie's activity is given by (Equation 2.7):

$$a_{(specie)} = \gamma . C \qquad \textbf{(Equation 2.7)}$$

where C is the concentration of the species involved in the reaction and γ is the activity coefficient.

Typically, the activity may be replaced by the concentration if it is lower than about 0.001 M[26]. Using the concentrations for the different species present in the deposition solution listed in Table 2.1, we have calculated the equilibrium potentials for the two considered Pd electro-deposition reactions, as shown in Table 2.2.

Species	$[Cl^-]_{initial}$ **/ M**		
	$3.2 \cdot 10^{-3}$	**$6.2 \cdot 10^{-3}$**	**$9.2 \cdot 10^{-3}$**
$E_2(PdCl_4^{2-}/Pd^0)$ V *vs*. RHE	*0.797*	*0.767*	*0.748*

Table 2.2 : Theoretical equilibrium potential values.

Theoretical calculation shows significant modifications in the equilibrium potential value as a function of the chloride concentration. The Nernst potential value increases when decreasing the chloride concentration. This is connected to the influence of $[Cl^-]$ on the complex species concentrations, as we related in the previous paragraph: the increase of chloride concentration induces the presence of a smaller amount of Pd^{2+}.

2.3 Electro-deposition of Pd/Pt(100)

After preparing and characterizing the Pt(100) surface in sulfuric acid (see chapter 1 paragraph 1.4.2), the electrode is transferred protected by a droplet of electrolyte into the deposition cell under potential control at 0.95 V *vs.* RHE, where neither Pd deposition nor Pt(100) surface oxidation are occur.

Figure 2.3 shows the cyclic voltammetry of Pt(100) in 10^{-4} M $PdCl_2$ + $3 \cdot 10^{-3}$ M HCl + 0.1 M H_2SO_4 at a speed rate equal to 0.1 mV·s^{-1}.

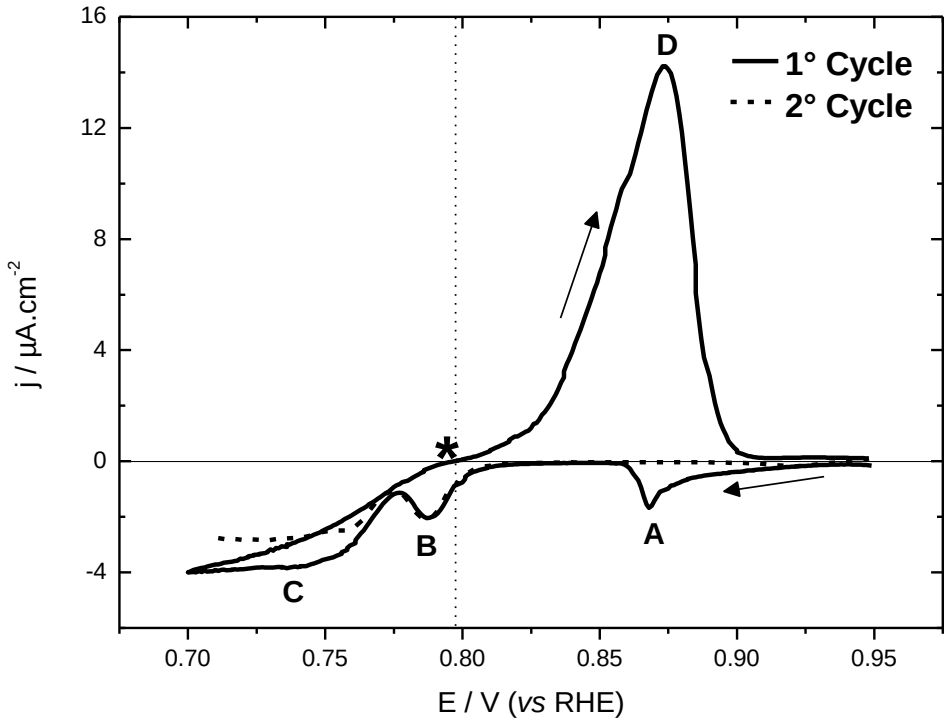

Figure 2.3 : Pt(100) in 10^{-4} M $PdCl_2$ + $3 \cdot 10^{-3}$ M HCl + 0.1 M H_2SO_4 at 0.1 mV·s^{-1}. The black line is the first cycle and the dashed line is the positive scan of the second cycle. Theoretical (dotted line, see paragraph 2.2.2) and experimental (*) equilibrium potential value are also shown.

Two peaks A (0.87 V *vs.* RHE) and B (0.78 V *vs.* RHE) are present in the negative scan. Region C is characterized by diffusion limitation, as indicated by the constant current value. A similar current profile was found for Pd deposition onto Pt(111)[11], except for the presence of peak B and for the absence of a small oxidation peak at high potential. The theoretical thermodynamic potential (paragraph 2.2.2), indicated by the dotted line, is in agreement with the point of zero current pointed out by the asterisk (*) in the positive scan.

The peak A position always remains above the Nernst potential. It corresponds to an under potential deposition (UPD) process, i.e. the electrochemical deposition of surface (sub) monolayers at higher potentials than the reversible Nernst potential corresponding to bulk deposition. According to the literature[11,28], the UPD phenomenon is observed in the first adlayer(s) and is due to the different interaction energies between adsorbate–adsorbate and adsorbate–substrate. The charge of Peak A is equal to 395 µC·cm^{-2}. This value is close to the theoretical charge of one

monolayer (418 µC·cm^{-2}). It is suggesting that peak A corresponds to the deposition of a first Pd monolayer.

Most of the peak B is below the Nernst potential but it is starting above equilibrium potential. This second point would suggest an UPD process. In opposite, the peak B is not well separated from bulk deposition (current is not back to zero between peaks B and C). The charge of peak B is calculated by current integration from high potential down to the current minimum between peaks B and C. It is equal to 415 µC.cm^{-2}. It is suggesting that peak B corresponds to the deposition of a second Pd monolayer. Although peaks A and B correspond to one Pd monolayer each, we do not know the morphology of the corresponding deposits. The assignment of these peaks will be discussed in detail in paragraph 2.4, with the help of the electrochemical characterization of the film's surface. Peak C is more likely a plateau. It is well below Nernst potential. It is associated with bulk Pd deposition. The plateau corresponds to the diffusion limit of Pd^{2+} species coming from the solution's bulk.

Only one dissolution peak D (0.87 V *vs.* RHE) is observed in the positive scan, preventing from separating the different Pd contributions (dissolutions of peaks A, B and C). Peak D's potential is significantly above the ones of peaks B and C. In opposite, peak A is overlapping the highest part of peak D.

During the second negative scan (Figure 2.3), the UPD peak A is no more present. This observation can only be explained by the fact that the first Pd layer dissolution does not occur at least below 0.95 V *vs.*RHE. So, the dissolution peak D does not include the UPD associated with peak A. Such phenomenon has already been reported by Lebouin et al.[11] in the Pd/Pt(111) case, even if the first layer could be at least partly dissolved. Above 0.95 V vs.RHE it would be anyhow difficult to separate UPD dissolution from surface's oxide formation.

In opposite the charge under peak B during the second scan does not significantly evolve (410 µC·cm^{-2}), corresponding also in this case to the deposition of a complete second layer. So, for sure, the dissolution associated to peak D does include the deposit associated with peak B. Peak D corresponds to the dissolution of both second Pd layer and bulk Pd deposits.

In the region C, we notice that the current intensity decreases with cycling, even if we cannot find an explanation for this behavior.

2.3.1 Effect of chloride concentration

The influence of chloride concentration on the theoretical equilibrium potential for a Pd electrode in the corresponding deposition bath has been previously discussed in paragraph 2.2. It is now interesting to compare the theoretically predicted behavior with an experimental study. Figure 2.4 shows the Pd deposition curves obtained in 10^{-4} M $PdCl_2$ + 0.1 M H_2SO_4 + x HCl, with different chloride concentrations (x = $3{\cdot}10^{-3}$ M, $6{\cdot}10^{-3}$ M, $9{\cdot}10^{-3}$ M).

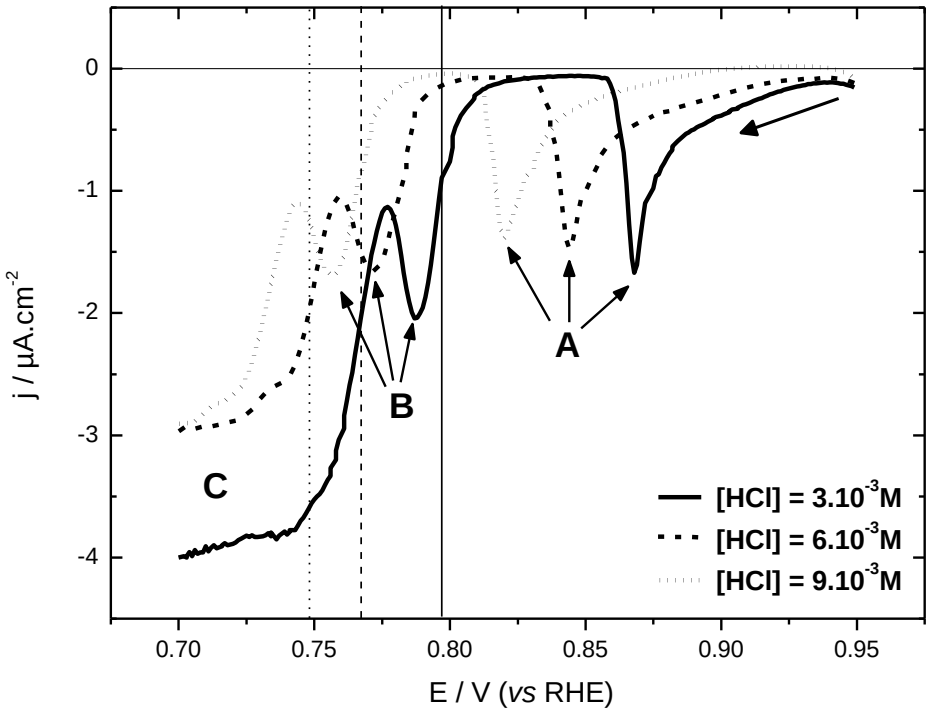

Figure 2.4 : Pt(100) in 10^{-4} M $PdCl_2$ + 0.1 M H_2SO_4 + x HCl (x = $3{\cdot}10^{-3}$ M continuous line; $6{\cdot}10^{-3}$ M dashed line; $9{\cdot}10^{-3}$ M dotted line), 0.1 mV·s^{-1}. Vertical lines correspond to the theoretical thermodynamic potential (see paragraph 2.2.2).

Varying the concentration of HCl does not modify the general deposition profile, but the whole curve is shifted towards lower potential values with [HCl] increasing, in agreement with theoretical calculation. As discussed in paragraph 2.2.2, chloride concentration has a major role in the Pd complex concentrations in the solution. A higher chloride concentration is lowering the concentration of free Pd^{2+} in solution and so shifting down the Nernst potential.

Each curve is composed by the 3 distinct zones (peak A, peak B and region C) already discussed in the previous sections. Table 2.3 show the potential position of peaks A and B.

[HCl] / M	**Peak A** / V *vs.* RHE	**Peak B** / V *vs.* RHE
$3 \cdot 10^{-3}$	0.868	0.787
$6 \cdot 10^{-3}$	0.844	0.771
$9 \cdot 10^{-3}$	0.820	0.757

Table 2.3: Potential positions for peaks A and B of Figure 2.4.

The potential of peak A is shifting toward lower values (about 48 mV from $3 \cdot 10^{-3}$ M up to $9 \cdot 10^{-3}$ M) in a very similar way to the Nernst potential (vertical lines, 49 mV). In opposite, peak B is less shifting (32 mV). First this finding evidences the presence of different deposition mechanisms for the first and for the second layers. Secondly, in correspondence with chloride concentration increase, peak B is better separated from the Nernst potential. For $9 \cdot 10^{-3}$ M, the potential of current maximum of peak B is 9 mV higher than the Nernst potential. Moreover, nearly all peak B is at potential higher than Nernst potential although it is still not completely separated from bulk deposition (peak C). It is highlighting the UPD character of peak B.

As explained in paragraph 2.1.3, the electrode is inserted into the electrochemical cell at 0.95 V *vs.* RHE in order to avoid oxide formation. Unfortunately, Pd deposition already begins at this potential value for the lowest chloride concentration, $3 \cdot 10^{-3}$ M. It is then necessary to consider higher concentration to prevent from Pd deposition when inserting the crystal into the electrolytic solution. For this reason we have chosen to work with the highest chloride concentration, $9 \cdot 10^{-3}$ M. In this way the initial potential set at 0.95 V *vs.* RHE corresponds to a domain where neither oxide forms non Pd deposits, allowing a good control of the film deposition process.

2.4 Pd/Pt(100): electrochemical characterization

After Pd deposition, the electrode is transferred to the cell containing 0.1 M H_2SO_4 for the electrochemical surface characterization. This is the same cell

previously used for the free Pt(100) surface characterization (chapter 1 paragraph 1.4.2). We recall that the insertion potential was 0.4 V *vs.* RHE, corresponding to the double layer region, where no reaction occurs.

Even if the number of required cycles before reaching a stable CV may vary from sample to sample, such process is always present. Figure 2.5 presents the ten first voltammograms obtained for Pd_{1ML}/Pt(100) in 0.1 M H_2SO_4 at 10 $mV \cdot s^{-1}$.

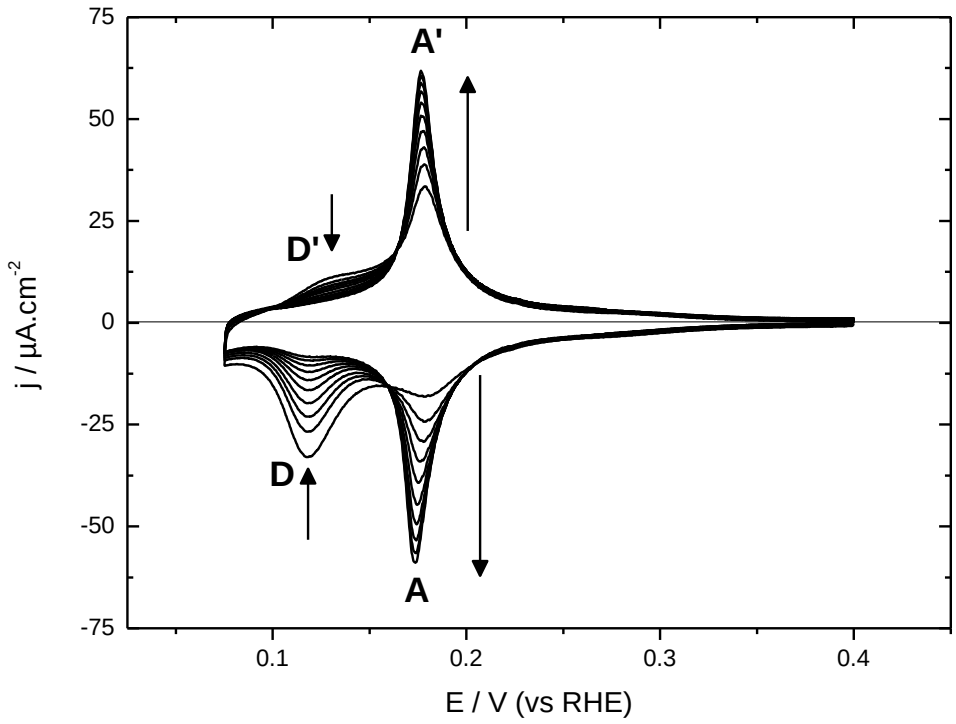

Figure 2.5: Ten first voltammograms for Pd_{1ML}/Pt(100) in 0.1 M H_2SO_4, 10$mV \cdot s^{-1}$.

The first cycle shows the presence of two pair of peaks A;A' and D;D'. With cycling, peaks D;D' intensity reduces, while peaks A;A' increase. Rearrangements with cycling (electrochemical annealing) were already reported for Pd/Pt(100)[31] but also for Pd/Au(111)[21,29–31], suggesting that the initially grown Pd islands undergo coalescence during cycling and form a uniform layer.

The same behavior is observed for films with thickness higher than 1 ML, but in this case two peaks D_2;D_2' are observed at about 0.26 and 0.25 V *vs.* RHE, their signature disappearing with cycling.

With the purpose of a clear presentation of the results, the sets of experiments are presented in two sections: from 1 ML up to 2 ML and beyond 2 ML.

If not differently specified, the presented curves correspond to the 10th cycle.

2.4.1 From 1 ML up to 2 ML

Figure 2.6 shows the electrochemical characterization of Pd films from 1 up to 2 ML as equivalent thickness. The Pt(100) profile measured in the same experimental conditions is presented as well.

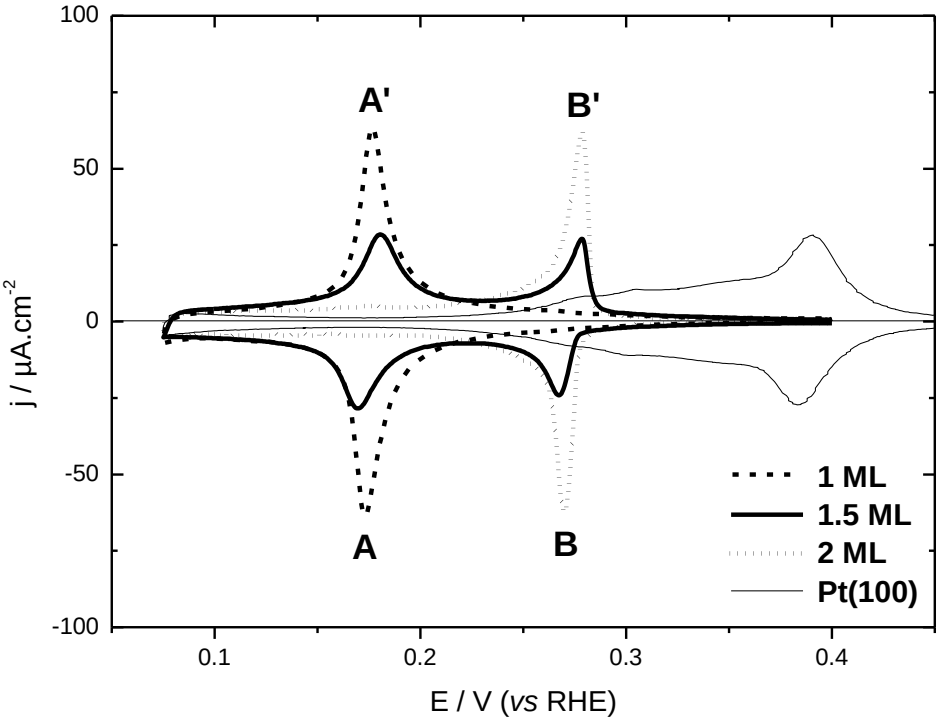

Figure 2.6 : Pd_{xML}/Pt(100) voltammograms in 0.1 M H_2SO_4, 10 mV·s^{-1}: 1 ML (dashed line), 1.5 ML (bold line), 2 ML (dotted line) and Pt(100) (thinner line).

As expected, the difference between the Pd films and the Pt(100) profiles is remarkable. For $Pd_{1M}L$/Pt(100) two reversible peaks A and A' are observed, at 0.175 V *vs.* RHE. According to the literature[9,21,32], these peaks are associated with hydrogen/(bi)-sulfate adsorption/desorption on the first Pd layer. The signature of Pt(100) surface has completely disappeared, showing that the first Pd layer completely deposits before the second layer growth.

As the film thickness increases up to 1.5 ML, the intensity of A and A' peaks decreases, signature of the fact that the 1st Pd layer is progressively covered. We note that they are less reversible than for Pd_{1ML}/Pt(100). This can be attributed to the

fact that the Pd first layer free surface is now composed of islands separated by the 2nd Pd layer. At the same time two other peaks B and B' are growing. They are related to the same adsorption/desorption phenomena as for (A;A')[9,21,32], but this time on the free surface of deposit's regions higher than one atomic layer. In particular, their presence is directly due to adsorption/desorption process on the second Pd layer. Electronic effects of the Pd-Pt and Pd-Pd surface on hydrogen/(bi)-sulfate adsorption/desorption are surely responsible for the observed difference in the potential position[33]. We also remark that peaks B;B', at 0.267 V and 0.278 V *vs.* RHE, are less reversible than A;A'. Again, this can be connected to the presence of different Pd sites, like Pd-Pd steps.

For Pd_{2ML}/Pt(100) peaks A and A' have completely disappeared and only peaks B and B' are present. We notice that their position has not changed between 1.5 ML to 2 ML. This is the clear signature that the first Pd layer has been completely covered and that two complete monolayers have been deposited on Pt(100). This observation clearly indicates that we are in the presence of a layer–by–layer (also called Frank-van der Merwe) growth mechanism up to two layers. This layer by layer growth is in agreement with a UPD process for the two corresponding layers.

Contrary to all the studies previously published with other electrochemical deposition methods and in the absence of chloride (see chapter 1, paragraph 1.6), we have succeeded in obtaining a layer–by–layer Pd growth on Pt(100) up to two monolayers. Our results are in agreement with the growth mechanism found for Pd deposition in UHV by Attard et al.[8]. The negative scan method at very low deposition rate (0.1 $mV \cdot s^{-1}$) has surely an important role in the growth mechanisms, but we cannot neglect the effect of chloride in the electrolytic solution. Indeed, it has been shown that chloride have a main role in favoring the layer-by-layer growth in the metallic depositions[34,35].

2.4.2 Beyond 2ML

Figure 2.7 shows the electrochemical characterization for Pd films beyond 2 ML in H_2SO_4 0.1 M, 10 $mV \cdot s^{-1}$.

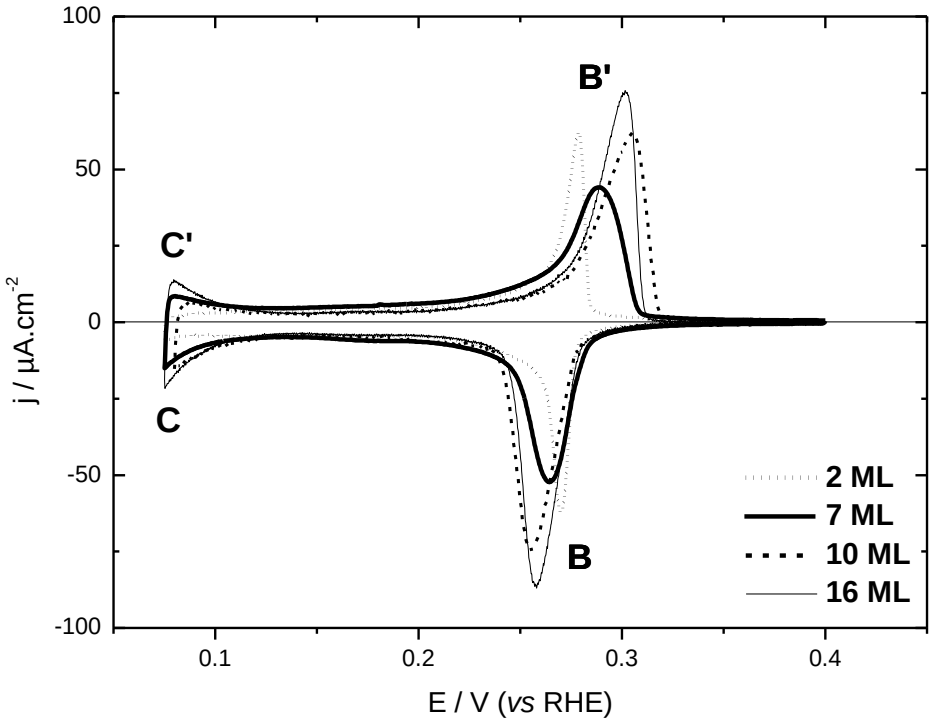

Figure 2.7 : PdxML/Pt(100) in 0.1 M H_2SO_4, 10 $mV.s^{-1}$; 2 ML (dotted line), 7 ML (thicker continuous line), 10 ML (dashed line), and to 16 ML (thinner continuous line).

The thickness increase from 2 ML up to 16 ML does not induce the growth of other peaks, but it produces a worsening of the (B;B') peaks irreversibility and an enlargement of its *full width at half maximum* (*FWHM*) at least from 2 ML up to 7 ML. A similar phenomenon is related in the literature for Pd/Pt(111)[11,36–38] and Pd/Au(111)[29]. This finding has been associated with an increase of the surface roughness with the film thickness due to expected 3D growth beyond the second Pd layer[36–38].

The increase of roughness in our system will be confirmed by atomic force microscopy experiments, as we will show in paragraph 2.5.

The peaks at lower potential (C and C') are mainly due to the hydrogen insertion/desinsertion, even if hydrogen adsorption/desorption contribution cannot be excluded. Such contributions were not present in the thinner films (up to 2 ML). Hydrogen insertion seems to occur only beyond 2 ML.

The integrated charges in the 0.325–0.125 V *vs.* RHE interval (see Figure 2.7) as a function of the Pd films thickness are shown in Figure 2.8.

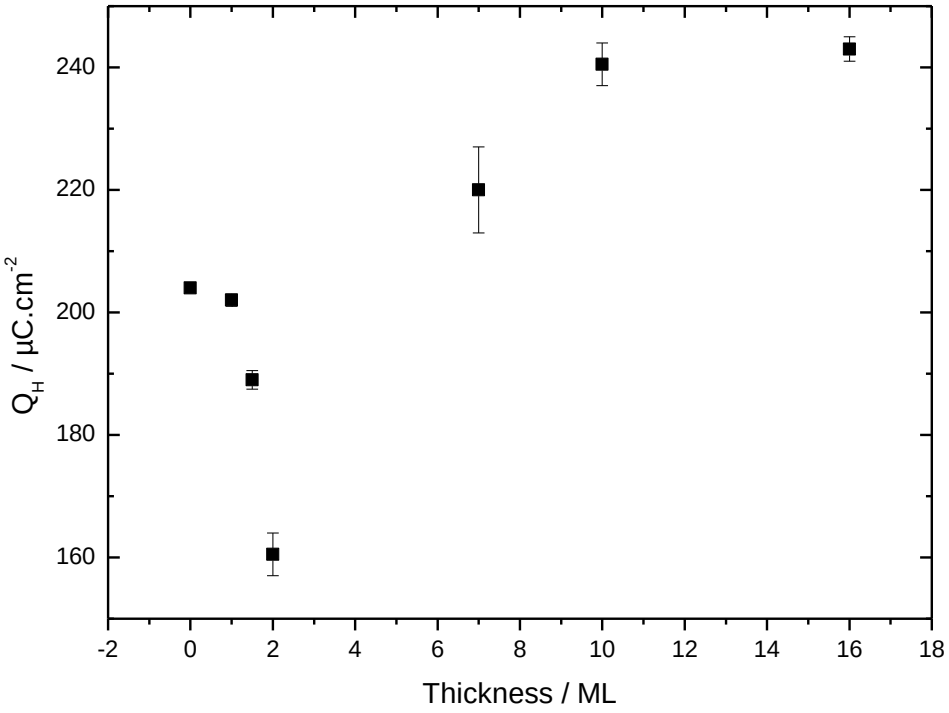

Figure 2.8: Pd_{xML}/Pt(100): evolution of the integrated charge Q_H (0.325-0.125 V vs. RHE) from voltammetries shown in Figure 2.6 and Figure 2.7 as a function of the thickness. QH is calculated as the mean value between cathodic and anodic values, the half of their difference being the uncertainty. The corresponding value for Pt(100) is shown as well (0.150-0.450 V vs. RHE)

Three different behaviors for the integrated charge Q_H are observed. The charges due to hydrogen (bi)-sulfate adsorption/desorption on Pt(100) and on Pd_{1ML}/Pt(100)° are very similar. From 1 ML up to 2 ML, Q_H decreases to reach a minimum value of about 160 $\mu C \cdot cm^{-2}$. Such behavior has been observed also by Lebouin[39] for Pd/Pt(111), but in this system, characterized by a Stranski–Krastanov* growth model, the integrated charge has a minimum in correspondence of the first complete Pd adlayer. Why do we observe a minimum of the quantity of adsorbed/desorbed anions on the Pd atoms in correspondence of the complete layer preceding the 3D growth (the second for Pd/Pt(100) and the first for Pd/Pt(111))? Such intriguing result should be further studied, from the experimental (for example with replacement of sulfate by other anions) and from the theoretical point of view.

The electronic influence of the substrate on the first and on the second Pd layer should be considered. DFT (density functional theory) calculation has been made by

**Stranski–Krastanov growth model*: this mode follows a two step process: initially the films grow in a layer–by–layer fashion on a crystal substrate. Beyond a critical layer thickness growth continues through the nucleation and coalescence of adsorbate islands.

Roudgar et Groß[33] for Pd/Au(111). The authors have shown that the adsorption energy of hydrogen presents a minimum in correspondence of two complete Pd adlayers.

The charge increases beyond 2 ML, probably reflecting a 3D growth of the Pd/Pt(100) film. Indeed, such a behavior has been already observed for Pd/Pt(111)[11], where the increase of the integrated charge corresponding to hydrogen (bi)-sulfate adsorption/desorption has been attributed to the increase of the surface roughness. We will show in paragraph 2.5 that such a description is confirmed by AFM images.

2.4.3 Comparison between Pd/Pt(100) and Pd/Pt(111) films

It is interesting to consider the influence of the crystallographic orientation comparing Pd deposition on Pt(100) and Pt(111). Pd/Pt(111)° films have been studied by several authors[30,31,36,37,40–50] and in particular at LEPMI by Lebouin et al.[10,11,34,39]. These authors used the same deposition method we have considered during this thesis. We also did Pd deposition and characterization on Pt(111) for hydrogen insertion studies (see chapter 4, paragraph 4.2). In the following we will show the deposition and characterization curves obtained on both systems following in the same experimental conditions.

Pd electrochemical deposition

Figure 2.9 shows Pd deposition curves onto Pt(100) and onto Pt (111) in 10^{-4} M $PdCl_2$ + 0.1 M H_2SO_4 + $3 \cdot 10^{-3}$ M HCl at 0.1 $mV \cdot s^{-1}$.

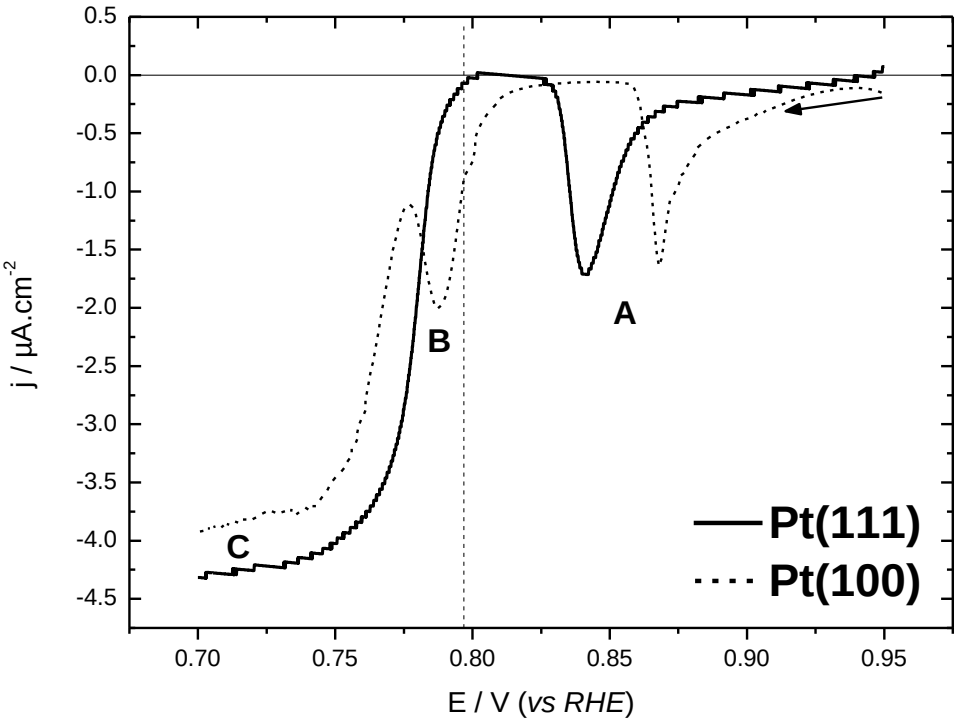

Figure 2.9 : Pt(111) (continuous line) and Pt(100) (dotted line) in 10^{-4} M $PdCl_2$ + 0.1 M H_2SO_4 + $3 \cdot 10^{-3}$ M HCl at 0.1 mV·s^{-1}. The vertical dotted line indicates the theoretical equilibrium potential.

Pd deposition onto both Pt(100) and Pt(111)[11] presents the UPD peak for the first layer deposition, even if the deposition seems to be easier on the more open surface. Indeed Pd UPD on Pt(100) is at higher potentials (0.87 V *vs*. RHE) than on Pd/Pt(111) (0.84 V *vs*. RHE). This is not surprising, as adsorption reactions on the several fcc faces can have different energies[28,51,52]. In particular, chemical bounding between the adsorbate and the substrate is different for the threefold sites of the (111) surface compared to the fourfold sites of the (100) surface. The adsorption is strongest on the open (100) surface compared to the dense (111).plane.

It is difficult to compare bulk deposition onset in the two systems, as peak B is not present for Pd/Pt(111). Nevertheless, we can say that the second layer deposition begins also at higher potential for Pd/Pt(100).

The charge calculated under the UPD peaks are 393 and 459 µC·cm^{-2} for Pt(100) and Pt(111), respectively. These values are close to the theoretical ones, 418 µC·cm^{-2} for Pt(100) and 480 µC·cm^{-2} for Pt(111). Due to the higher packing

density of Pt(111) compared to Pt(100), the corresponding charge for 1 ML deposition is higher.

Diffusion limited zone C is present in the Pd deposition on both surfaces and begins in the same potential region, at about 0.75 V *vs*. RHE.

Finally, the geometric effect of the different packing characterizing the two surfaces has a great effect on the Pd growth mechanisms. Compared to the more dense Pt(111) surface, the UPD phenomenon for the first layer deposition is maintained, even if shifted towards lower potential. The signature of a second layer deposition separated from bulk contribution is clearly seen only for Pd/Pt(100), even if we could not clearly assign it to UPD. This finding indicates that the electronic influence of the substrate on the adlayer is very different according to the orientation. In particular, it seems to extend beyond the first layer for the more open surface.

Pd film electrochemical characterization

Figure 2.10 represents the electrochemical characterizations of Pd films deposited on Pt(111) and on Pt(100) with different thicknesses.

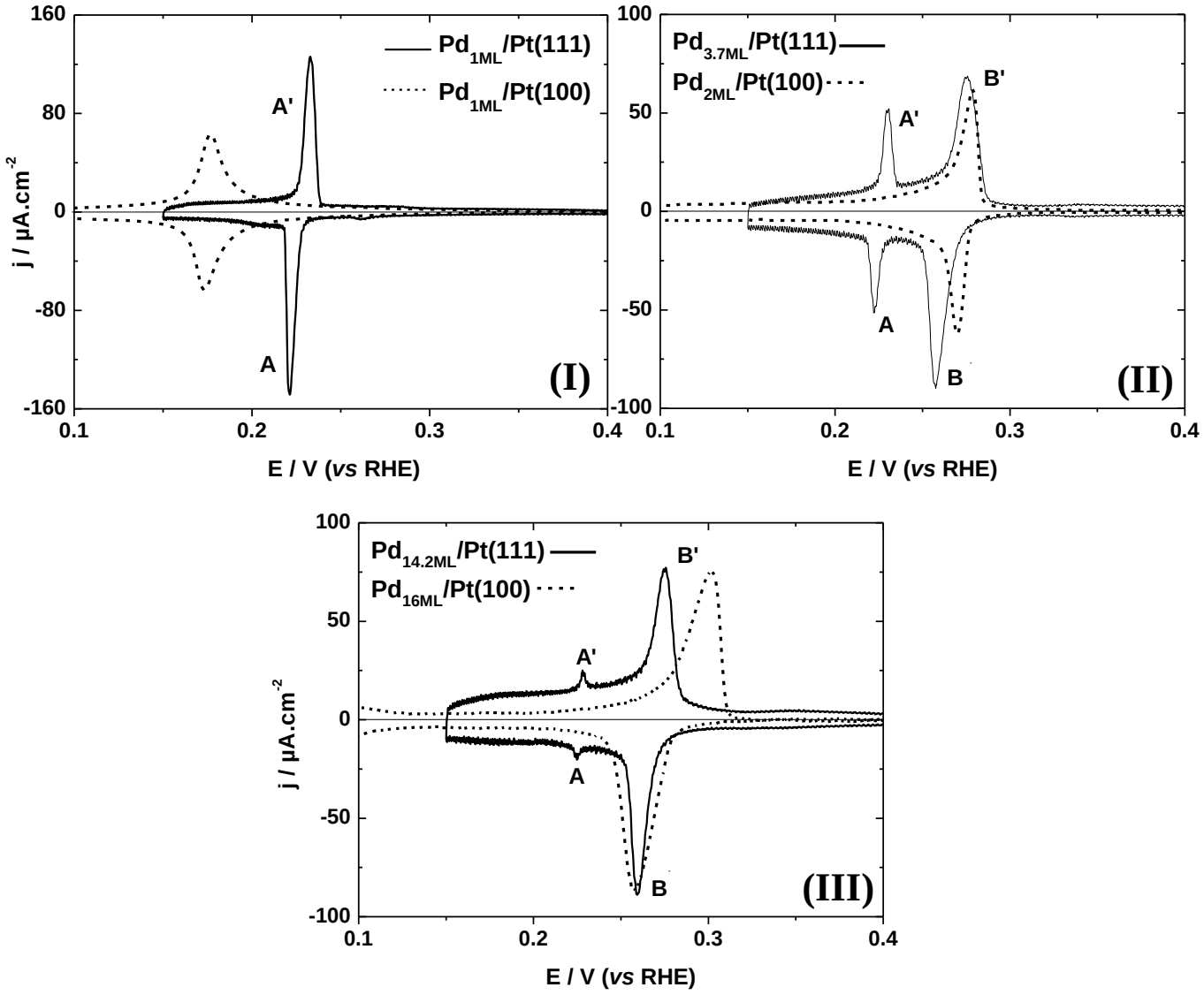

Figure 2.10 : Cyclic voltammetries of Pd_{xML}/Pt(111) and Pd_{xML}/Pt(100) for various thicknesses in 0.1 M H_2SO_4 at 10 mV.s^{-1}. (I) 1 ML, (II) middle thicknesses and (III) higher thicknesses.

For 1 ML (Figure 2.10 – I), both systems present a couple of peaks A;A' characteristic of the co-adsorption/desorption of hydrogen and (bi)sulfates on the first Pd monolayer. Indeed, in both cases there is the completion of the first Pd layer with UPD process[11]. Nevertheless, the peaks position is shifted by about 50 mV starting at higher potential for Pd/Pt(111) and they are reversible only for Pd_{1ML}/Pt(100). The integrated charge for Pd_{1ML}/Pd(111) is close (185 µC·cm^{-2}) to that observed for Pd_{1ML}/Pd(100) (200 µC·cm^{-2}), these values being close to those found in the literature[11,21].

The Peaks (B and B') (see Figure 2.10 – II) are related to the same adsorption/desorption phenomena but on deposit regions higher than one atomic

layer. They are in the same potential position at about 0.27 V vs. RHE in the two systems. However, while the layer-by-layer growth is complete up to two layers for Pd/Pt(100), this is not the case of Pd/Pt(111), as indicated by the presence of peaks A;A' for 4 ML but also for 14 ML. Indeed, the Stransky-Krastanov growth mode (completion of the first Pd layer is followed by 3D growth) has already been shown for Pd/Pt(111)[11].

As already discussed in the previous paragraph, peaks A;A' are still present for the Pd_{14ML}/Pt(111) (Figure 2.10 – II), showing that the first Pd layer has still some free surface even at this higher thickness. The charges calculated are 275 and 280 $\mu C.cm^{-2}$ for $Pd_{14.2ML}$/Pt(111) and Pd_{16ML}/Pt(100), respectively, in agreement with Lebouin et al.[11]. These authors found that the integrated charge value increases with thickness and attributed this behavior to the increase of the surface roughness.

Concluding, the influence of the substrate orientation on the hydrogen–(bi) sulfate binding energies with the first Pd layer over Pt is important. In opposite, these energies seem to be very similar on the following layers. For the adsorption aspect, the influence of the crystallographic orientation is strongly decreasing after the first Pd layer. For the peaks reversibility, it is difficult to extract any conclusion versus the thickness and the influence of the substrate.

Contrarily to the layer-by-layer growth mode for Pd/Pt(100), the Stranski–Krastanov growth is characteristic of the Pd/Pt(111) films at least up to about 15 layers.

2.5 Atomic Force Microscopy characterization

In order to have a better insight into the surface morphology of the Pd/Pt(100) films, we made *ex situ* characterization with atomic force microscopy (AFM). We considered different film thicknesses with the aim to rely AFM observations to the electrochemical characterizations.

2.5.1 Introduction to AFM

High resolution microscopy was firstly developed by Gerd Binnig and Heinrich Rohrerin in the early 1980s as an offspring of the Scanning Tunneling Microscopy (STM)[53,54]. Indeed, they observed that relatively strong forces act between the tip and a surface in close proximity.

The AFM consists of a cantilever with a sharp tip at its end used as a probe and scanning the sample surface. The cantilever is typically made of silicon or silicon nitride with a tip size of the order of nanometers. In this study, we used an AFM system in the topographic mode produced by Veeco. The tip–sample interaction force is described by the Lennard Jones potential, where the interaction is attractive at certain distances (typically, beyond a few tenths of a nanometer) due to van der Waals interaction, and repulsive at very short distances due to the impenetrability of the electron clouds associated with the two surfaces. In topographic mode, the cantilever oscillates at a constant frequency with a certain amplitude, according to the Hooke's law of elasticity[55].

The images are created by scanning the tip on the surface area described by the in plane coordinates (x, y), as is represented in Figure 2.11. The morphology of the surface leads to different deflections of the laser on cantilever (Figure 2.11). This is recorded by a photodiode detector allowing the reconstruction of the topographic surface (z) as a function of (x,y).

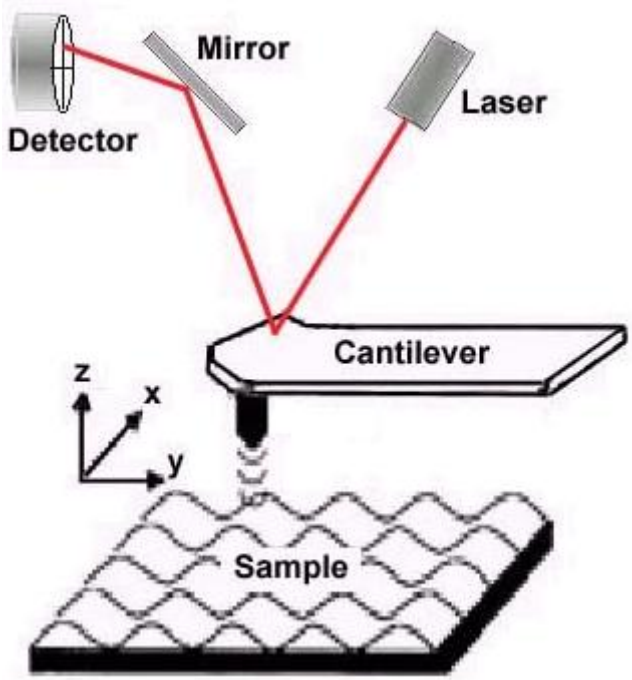

Figure 2.11: Scheme of AFM operation[56].

2.5.2 Experimental procedure

The topographic AFM images were collected *ex situ* on Pd/Pt(100) films with thickness of 2, 4 and 14 ML at SIMAP (Science et Ingénierie des MAtériaux et des Procédés, St. Martin d'Hères) in collaboration with Dr. Mireille Maret. Each Pd film has been deposited and electrochemically characterized in the chemical laboratory, following the procedures previously described. About 10 cycles have been applied to each film in order to obtain a stable electrochemical surface response. It was then quickly transferred to the AFM system in argon atmosphere protected by an ultra-pure water drop in order to prevent from contamination.

The images have been processed using the WSxM software, version 2.0 beta 6.0, developed by Nanotec Electronica S.L. This software allows analysing the surface topographic profile of the film. The roughness (σ) is evaluated calculating the Root Mean Square (RMS)[57–59], as shown in (Equation 2.8).

$$\sigma = \mathrm{RMS} = \sqrt{\sum_{n=1}^{N} \frac{\left(Z_n - \overline{Z}\right)^2}{N}} \qquad \textbf{(Equation 2.8)}$$

where N is the number of measured point in the considered sample area, Z_n is the surface vertical height in a given point and $\overline{Z}$ is the average of the surface vertical height within the given area. The roughness value can be expressed in nanometers. It can be translated into a number of atomic planes, where the interplanar distance for the (100) orientation is equal to 1.94 Å. In the following the roughness values have been calculated on the whole AFM image considered.

2.5.3 Results

Pd_{2ML}/Pt(100)

Figure 2.12 shows the AFM images (left) obtained for Pd_{2ML}/Pt(100). This is a topview of the sample. Dark colors refer to the lowest parts of the surface, while brigh colors refer to highest parts. The blue lines in the AFM images represent the profile shown on the right side of the image.

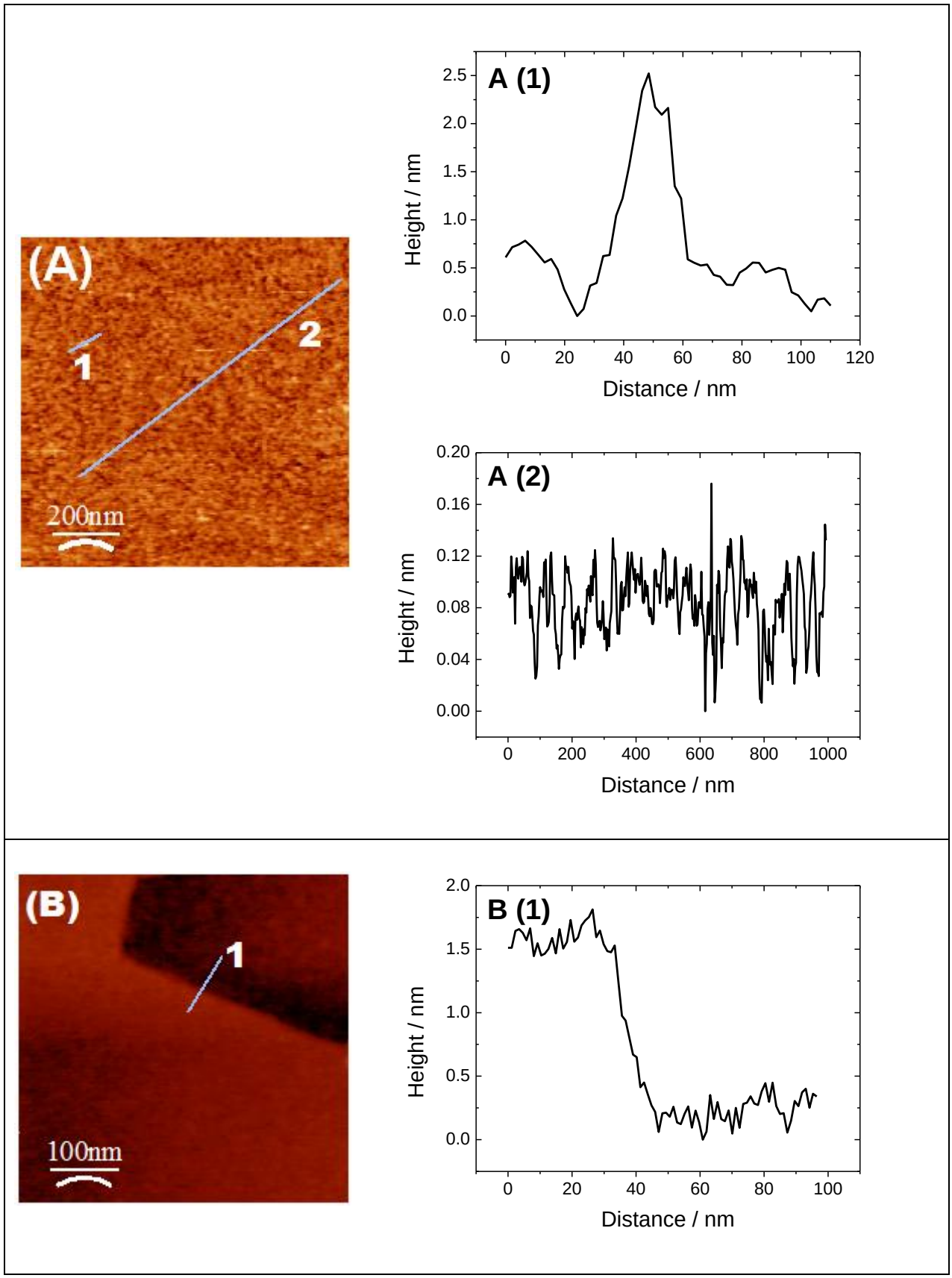

Figure 2.12: *Ex situ* AFM images of the Pd_{2ML}/Pt(100) sample. The analyzed regions are indicated by the blue lines and the corresponding surface profiles are shown to the right.

Pd_{2ML}/Pt(100) surface seems to be quite flat. The roughness (RMS) has been calculated and estimated equal to 0.27 nm corresponding to about 1.4 atomic planes. Few Pd islands have been observed (Figure 2.12 - A1). The analyzed one was about 2 nm high and 40 nm wide. In the other image (Figure 2.12 – B) the important difference in height is probably due to the presence of a step (about 1.5 nm high) on the Pt(100) substrate.

Pd_{4ML}/Pt(100)

Figure 2.13 shows the AFM images (left) and the z-profiles measured (right) obtained for Pd_{4ML}/Pt(100).

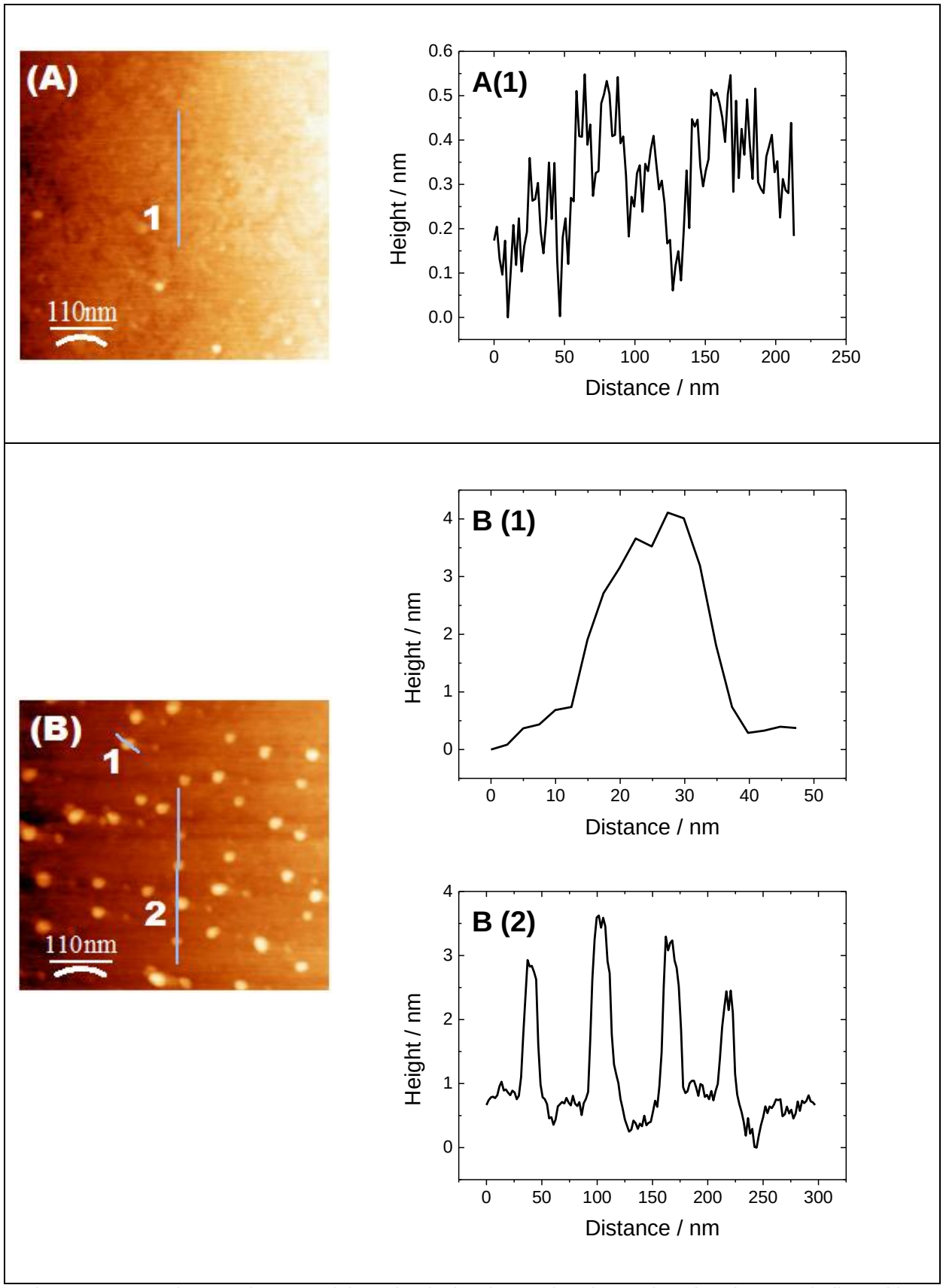

Figure 2.13: *Ex situ* AFM images of the Pd_{4ML}/Pt(100) sample. The analyzed regions are indicated by the blue lines and the corresponding surface profiles are shown to the right

Two distinct regions have been observed. In the first one (Figure 2.13 – A) the surface is relatively flat, even if some islands are present. The RMS calculated is equal to 0.89 nm (about 4.5 atomic planes). In the other zone (Figure 2.13 – B) the presence of islands is more important. Indeed, the RMS value corresponds to about 6.5 atomic planes (1.27 nm). The profile analysis of these islands shows a height from 2.5 up to 4 nm (Figure 2.13 – B2) corresponding to 13 – 20 atomic planes. The width of the island is equal to about 25 nm (Figure 2.13 - B1).

Pd_{14ML}/Pt(100)

Figure 2.14 shows the AFM images (left) obtained for Pd_{14ML}/Pt(100).

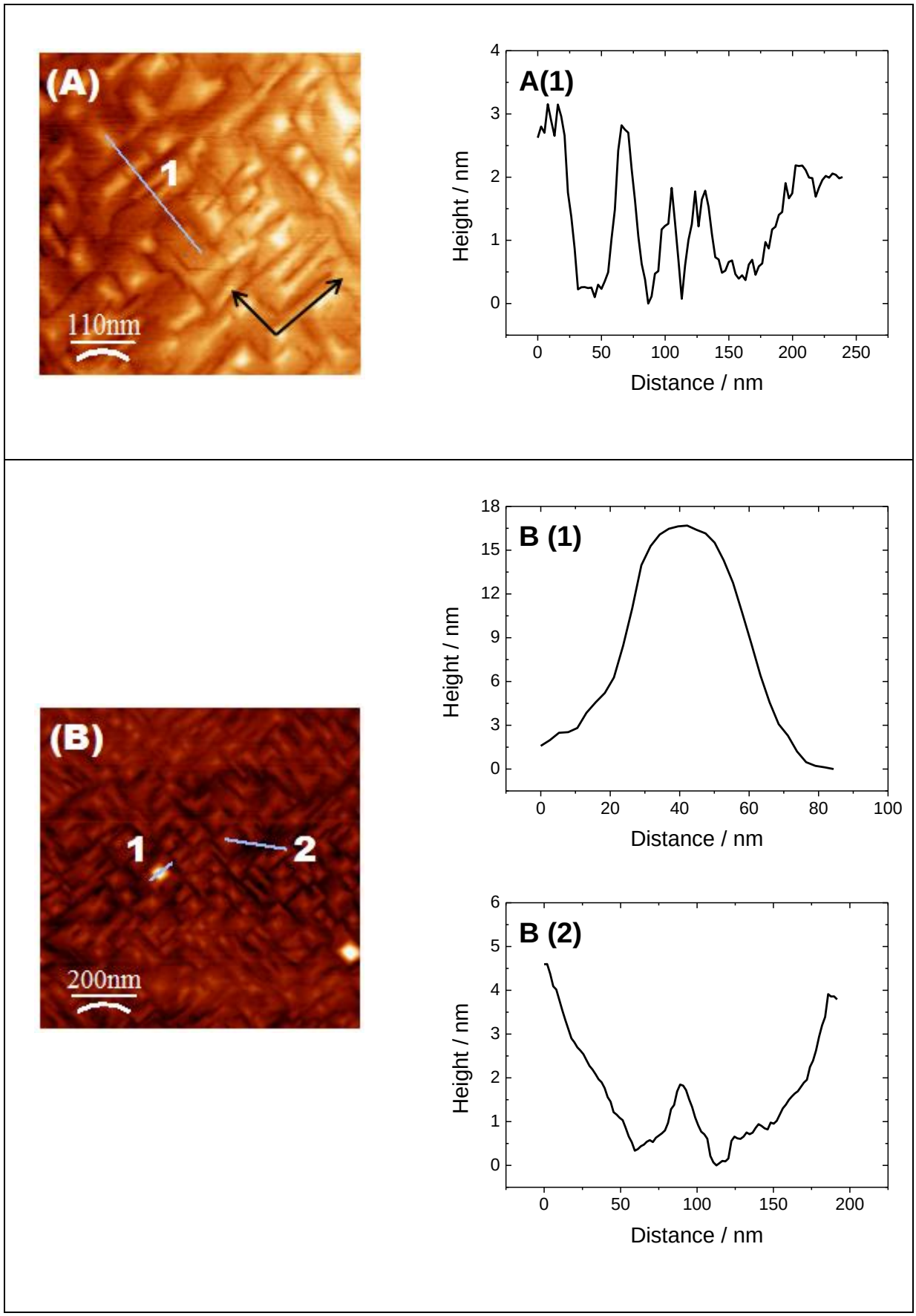

Figure 2.14: *Ex situ* AFM images of the Pd_{14ML}/Pt(100) sample. The analyzed regions are indicated by the blue lines and the corresponding surface profiles are shown to the right

This film (Figure 2.14) showed a quite different surface morphology compared to the thinner ones. No flat zones have been observed for this sample, presenting large square based pyramids as indicated by the black arrows in Figure 2.14 – A. This phenomenon is very different from the Pd growth on Pt(111)[11] where flat (111) areas are widely preserved during the deposition. From a theoretical point of view, bulk deposition on crystallites presenting several surface orientations is supposed to favor the emergence of orientations with the slower deposition kinetic. In this way, the kinetic on (111) would be the slow one compared to (100). So, on Pt(111), the (111) would be preserved. In opposite, on Pt(100), new (111) orientations are created by steps formation between the (100) terraces. The RMS is equal to 1.3 nm (6.8 atomic planes) for Figure 2.14 – A and 1.17 nm for Figure 2.14 – B. However, in the film analysis of the transversal cuts troughs down to 4 nm (23 atomic planes) is found, this value being equal to almost twice the expected thickness. Figure 2.14 – B1 shows the profile of a very large pyramid, presenting a height of 17 nm (87 atomic planes) and a width of 55 nm. In the hypothesis of a growth favoring the (111) orientation, pyramids may have only (111) facets. Such pyramids would have a 45° slope. This is not the case for the last pyramid. The deposit should still have (100) terraces with a large number of (111) steps.

For the comparative studies that will follow, the Table 2.4 presents a summary of the main points analyzed with the AFM images.

Thickness		RMS (nm)	Observations
2 ML		0.27 *(1.4 at. plans)*	• *Quite flat* • *Rare islands*
4 ML	Region A	0.89 *(4.6 at. plans)*	• *Quite flat* • *Few islands*
	Region B	1.27 *(6.4 at. plans)*	• *Many islands* • *2.5 – 4 nm(height); ~25 nm(width)*
14 ML		1.25±0.1 *(~6.5 at. plans)*	• *Numerous square based islands* • *~17 nm (height); ~55 nm (width)* • *troughs up to 23 atomic planes*

Table 2.4: Films characteristics obtained from the AFM images

Concluding, AFM images indicate that the surface is quite flat for Pd_{2ML}/Pt(100). Beyond this thickness, the roughness rapidly increases, corresponding to a 3D growth, and reaches the value of 1.25 nm for the thickest film Pd_{14ML}. Nevertheless, we remark that the roughness abruptly increases beyond 2 ML, but only slightly changes from 4 ML up to 14 ML. These findings are in agreement with the electrochemical characterization of the Pd films. Indeed, they confirm that the irreversibility of peaks B;B' (anions adsorption/desorption on the Pd atoms of the second and following layers) beyond Pd_{2ML} can be attributed to the larger roughness of the surface. The absence of a clear evolution of the peaks behavior with thickness (if > 2 ML) corroborates such assignment, as roughness only slightly evolves for higher thicknesses.

2.6 Conclusion

This chapter presented the study of the electro-deposition and the characterization of Pd/Pt(100) films.

The theoretically predicted influence of the chloride concentration on the species present in the deposition solution and on the equilibrium potentials have been confirmed experimentally. The deposition curves undergo a shift towards lower potentials with increasing of [HCl].

A chloride concentration equal to $9 \cdot 10^{-3}$ M has been chosen for a better separation between oxide formation on the Pt(100) surface and Pd deposition. The Pd deposition has been performed by introducing the clean Pt(100) electrode at 0.95 V vs. RHE. Then, the potential was scanned down at 0.1 mV s^{-1}. The UPD deposition of the first Pd layer has been observed. Contrary to Pd/Pt(111), the second layer deposition is separated from the following bulk deposition. It is also showing an UPD character. In opposite to the Pd films obtained with forced deposition or with cycling, we could observe a layer-by-layer deposition up to two layers. Such a growth was only observed with vapor deposition in UHV.

The film surfaces have been characterized in sulfuric acid solution. We could confirm the assignment of two different peaks in the voltammograms to the adsorption on the first Pd layer and on Pd atoms of the second and following layers. This study suggested the presence of a 3D growth beyond the two first complete

layers. An intriguing behavior of the integral charge for the hydrogen/(bi)-sulfate adsorption/desorption processes has been observed, showing a minimum value in correspondence of Pd_{2ML}/Pt(100).

Ex situ AFM images have been measured on several samples. The flat surface of the Pd_{2ML}/Pt(100) sample rapidly evolves with thickness. For Pd_{4ML}/Pt(100), two regions are observed; they are characterized by 3D growth with roughness being at least three times greater (0.89 nm) than for 2 ML. Roughness slightly increases for 14 ML, but the surface is here uniformly composed by square based pyramids following the (100) orientation of the substrate. The description of the surface morphology as obtained by AFM is in complete agreement with the electrochemical characterizations.

The comparison with Pd/Pt(111) has shown the important effects of the orientation on the film growth model.

2.7 References

(1) Clavilier, J.; Faure, R.; Guinet, G.; Durand, R. *Journal of Electroanalytical Chemistry and Interfacial Electrochemistry* **1979**, *107*, 205–209.

(2) Clavilier, J.; Armand, D.; Wu, B. L. *Journal of Electroanalytical Chemistry and Interfacial Electrochemistry* **1982**, *135*, 159–166.

(3) Kibler, L. A. Preparation and Characterization of Noble Metal Single Crystal Electrode Surfaces, *International Society of Electrochemistry* **2003**, 1–55.

(4) Kibler, L. A.; Cuesta, A.; Kleinert, M.; Kolb, D. M. *Journal of Electroanalytical Chemistry* **2000**, *484*, 73–82.

(5) Clavilier, J.; Armand, D.; Sun, S. G.; Petit, M. *Journal of Electroanalytical Chemistry and Interfacial Electrochemistry* **1986**, *205*, 267–277.

(6) Rodes, A.; Zamakhchari, M. A.; El Achi, K.; Clavilier, J. *Journal of Electroanalytical Chemistry and Interfacial Electrochemistry* **1991**, *305*, 115–129.

(7) Wagner, F. T.; Ross, P. N. *Journal of Electroanalytical Chemistry and Interfacial Electrochemistry* **1983**, *150*, 141–164.

(8) Attard, G. A.; Price, R. *Surface Science* **1995**, *335*, 63–74.

(9) Al-Akl, A.; Attard, G. A.; Price, R.; Timothy, B. *Journal of Electroanalytical Chemistry* **1999**, *467*, 60–66.

(10) Soldo-Olivier, Y.; Lafouresse, M. C.; De Santis, M.; Lebouin, C.; De Boissieu, M.; Sibert, E. *The Journal of Physical Chemistry C* **2011**, *115*, 12041–12047.

(11) Lebouin, C.; Soldo-Olivier, Y.; Sibert, E.; Millet, P.; Maret, M.; Faure, R. *Journal of Electroanalytical Chemistry* **2009**, *626*, 59–65.

(12) Skoog, D. A. *Fundamentals of Analytical Chemistry*; Boeck, D., Ed.; 8th ed.; Brooks Cole, 2004.

(13) Kibler, L. A.; Kleinert, M.; Randler, R.; Kolb, D. M. *Surface Science* **1999**, *443*, 19–30.

(14) Sassani, D. C.; Shock, E. L. *Geochimica et Cosmochimica Acta* **1998**, *62*, 2643–2671.

(15) Crosby, J. N.; Harrison, J. A.; Whitfield, T. A. *Electrochimica Acta* **1981**, *26*, 1647–1651.

(16) Droll, H. A.; Block, B. P.; Fernelius, W. C. *The Journal of Physical Chemistry* **1957**, *61*, 1000–1004.

(17) Harrison, J. A.; Hill, R. P. J.; Thompson, J. *Journal of Electroanalytical Chemistry and Interfacial Electrochemistry* **1973**, *47*, 431–440.

(18) Harrison, J. A.; Sierra Alcazar, H. B.; Thompson, J. *Journal of Electroanalytical Chemistry and Interfacial Electrochemistry* **1974**, *53*, 145–150.

(19) Harrison, J. A.; Thompson, J. *Electrochimica Acta* **1973**, *18*, 829–834.

(20) Attard, G. A.; Hazzazi, O.; Wells, P. B.; Climent, V.; Herrero, E.; Feliu, J. M. *Journal of Electroanalytical Chemistry* **2004**, *568*, 329–342.

(21) Álvarez, B.; Berná, a.; Rodes, a.; Feliu, J. M. *Surface Science* **2004**, *573*, 32–46.

(22) Paunovic, M.; Schlesinger, M. *Fundamentals of electrochemical deposition*; second.; John Wiley & Sons, Inc., 2006.

(23) Schlesinger, M.; Paunovic, M.; Abys, J. A. *Modern Electroplating*; 5th ed.; Wiley, 2010.

(24) Bard, A. J.; Faulkner, L. R. *ELECTROCHEMICAL METHODS Fundamentals and Applications*; JOHN WILEY & SONS, I., Ed.; 2nd ed.; 2001.

(25) Haynes, W. M. *Handbook of Chemistry and Physics*; 93rd ed.; CRC Press, 2012.

(26) Schlesinger, M.; Paunovic, M. *Modern Electroplating*; 5th ed.; Wiley, 2010.

(27) Castellan, G. W. *Physical Chemistry*; 3rd ed.; Addison-Wesley Publishing Company, Inc., 1983.

(28) Leiva, E. P. M. *Electrochimica Acta* **1996**, *41*, 2185–2206.

(29) Duncan, H.; Lasia, A. *Electrochimica Acta* **2007**, *52*, 6195–6205.

(30) Llorca, M. J.; Feliu, J. M.; Aldaz, A.; Clavilier, J. *Journal of Electroanalytical Chemistry* **1994**, *376*, 151–160.

(31) Llorca, M. J.; Feliu, J. M.; Aldaz, A.; Clavilier, J. *Journal of Electroanalytical Chemistry* **1993**, *351*, 299–319.

(32) Ball, M. J.; Lucas, C. a.; Marković, N. M.; Stamenković, V.; Ross, P. N. *Surface Science* **2003**, *540*, 295–302.

(33) Roudgar, A.; Groß, A. *Journal of Electroanalytical Chemistry* **2003**, *548*, 121–130.

(34) Lebouin, C.; Soldo-Olivier, Y.; Sibert, E.; De Santis, M.; Maillard, F.; Faure, R. *Langmuir* **2009**, *25*, 4251–5.

(35) Sibert, E.; Ozanam, F.; Maroun, F.; Behm, R. J.; Magnussen, O. M. *Surface Science* **2004**, *572*, 115–125.

(36) Duncan, H.; Lasia, A. *Journal of Electroanalytical Chemistry* **2008**, *621*, 62–68.

(37) Ball, M. J.; Lucas, C. A.; Marković, N. M.; Stamenkovic, V.; Ross, P. N. *Surface Science* **2002**, *518*, 201–209.

(38) Hoyer, R.; Kibler, L. A.; Kolb, D. M. *Electrochimica Acta* **2003**, *49*, 63–72.

(39) Lebouin, C. Films d'épaisseurs nanométriques de Pd sur Pt(111): élaboration, caractérisations et étude de l'électro-insertion de l'hydrogène, Grenoble University, 2008.

(40) Inukai, J.; Ito, M. *Journal of Electroanalytical Chemistry* **1993**, *358*, 307–315.

(41) El-Aziz, A. M.; Hoyer, R.; Kibler, L. A.; Kolb, D. M. *Electrochimica Acta* **2006**, *51*, 2518–2522.

(42) Climent, V.; Marković, N. M.; Ross, P. N. *The Journal of Physical Chemistry B* **2000**, *104*, 3116–3120.

(43) Arenz, M.; Stamenkovic, V.; Schmidt, T. J.; Wandelt, K.; Ross, P. N.; Marković, N. M. *Surface Science* **2003**, *523*, 199–209.

(44) Attard, G. A.; Bannister, A. *Journal of Electroanalytical Chemistry and Interfacial Electrochemistry* **1991**, *300*, 467–485.

(45) Arenz, M.; Stamenkovic, V.; Schmidt, T. J.; Wandelt, K.; Ross, P. N.; Marković, N. M. *Surface Science* **2002**, *506*, 287–296.

(46) Álvarez, B.; Climent, V.; Rodes, A.; Feliu, J. M. *Physical Chemistry Chemical Physics* **2001**, *3*, 3269–3276.

(47) Álvarez, B.; Climent, V.; Rodes, a.; Feliu, J. M. *Journal of Electroanalytical Chemistry* **2001**, *497*, 125–138.

(48) Marković, N. M.; Lucas, C. A.; Climent, V.; Stamenković, V.; Ross, P. N. *Surface Science* **2000**, *465*, 103–114.

(49) Álvarez, B.; Feliu, J. M.; Clavilier, J. *Electrochemistry Communications* **2002**, *4*, 379–383.

(50) Clavilier, J.; Llorca, M. J.; Feliu, J. M.; Aldaz, a. *Journal of Electroanalytical Chemistry and Interfacial Electrochemistry* **1991**, *310*, 429–435.

(51) Schmickler, W. *Chemical Physics* **1990**, *141*, 95–104.

(52) Lehnert, W.; Schmickler, W. *Journal of Electroanalytical Chemistry and Interfacial Electrochemistry* **1991**, *310*, 27–37.

(53) Binnig, G.; Quate, C. F. *Physical Review Letters* **1986**, *56*, 930–933.

(54) Giessibl, F. J. *Reviews of Modern Physics* **2003**, *75*, 949–983.

(55) Dupas, C.; Houdy, P.; Lahmani, M. *Nanoscience: Nanotechnologies and Nanophysics*; Springer, verlag B., Ed.; 2007.

(56) Núñez, M. E. Biophysics of Bacterial Biofilms http://www.mtholyoke.edu/~menunez/ResearchPage/AFM.html.

(57) Miller, J. D.; Veeramasuneni, S.; Drelich, J.; Yalamanchili, M. R.; Yamauchi, G. *Polymer Engineering & Science* **1996**, *36*, 1849–1855.

(58) Khulbe, K. C.; Feng, C. Y.; Matsuura, T. *Synthetic Polymeric Membranes*; Springer Berlin Heidelberg: Berlin, Heidelberg, 2008.

(59) Boussu, K.; Van der Bruggen, B.; Volodin, A.; Snauwaert, J.; Van Haesendonck, C.; Vandecasteele, C. *Journal of colloid and interface science* **2005**, *286*, 632–8.

3 Bibliographic study: Hydrogen insertion into palladium

A bibliographic study on the subjects involving the process of hydrogen insertion into palladium will be conducted in this chapter. We will discuss the problems and the current developments concerning this storage form. Hydrogen insertion isotherms, the hysteresis phenomenon and the differences between Pd bulk, Pd nanoparticles and Pd thin films will be discussed in detail.

3.1 Introduction

The world energy consumption is increasing every year. This consumption passed from $5 \cdot 10^{12}$ kWh/year in 1860 to $1.2 \cdot 10^{14}$ kWh/year today. The main part of energy production, $1.0 \cdot 10^{14}$ kWh/year (80%), is based on fossil fuels (coal, oil and gas). World population has increased in the last century by a factor of 6 but energy consumption has risen by a factor of 80. This increase is 13 times higher than the one of population. The world-wide average continuous power consumption today is equal to 2 kW/person. But this consumption is unbalanced. For example, in Europe and USA, the power consumption is around 5 and 10 kW/person, respectively. Otherwise, there are two billion people on earth who do not consume any fossil fuels. The fossil fuels reserves on earth are very limited, spread irregularly in the world. While the Arab league produces around 25% the all consumption, many countries are not petroleum producer or in other cases they consume more than they produce like USA and European Union (EU). Moreover, predictions based on the present evolution of the energy consumption show that demand will soon exceed supply. Furthermore, the consumption of fossil fuels is responsible for the increase in the carbon dioxide in the atmosphere of approximately $3 \cdot 10^{12}$ kg·C/year, the cause of a greenhouse gas and increase in the temperature on earth[1]. A potential solution is to develop a low-carbon future, where fossil fuel use is reduced, replacing it with zero-carbon energy sources such as from renewable. Dihydrogen can be used as convenient energy carrier for renewable energy sources. It exhibits the highest heating value per mass of all chemical fuels[2].

But there are two reasons why hydrogen is not the major fuel of today energy consumption:

(1) The cost for production, although it is the most abundant element in the universe, it has to be produced, since on earth it only exists in the form of water and hydrocarbons and its transformation is an expensive process;

(2) Hydrogen is a molecular gas at atmospheric temperature and it is a very reactive gas. For these reasons its transport is very dangerous and complicated.

A modern car optimized for mobility burns about 24 kg of petrol in a combustion engine, with a range of 400 km. To cover the same range, 8 kg of hydrogen are needed for a combustion engine version or 4 kg hydrogen for an electric car with a fuel cell[1–4]. The volume occupied by 4 kg of hydrogen is 45 m^3, such a reservoir being hardly a practical solution for a vehicle (the great villain in the consumption of fossil fuel). Even if the energy produced from hydrogen doesn't produce pollution helping the environmental purpose, hydrogen production is currently realized from a hydrocarbon with CO_2 generation (byproduct). Research is being developed on clean hydrogen production from water hydrolysis.

Several storage methods are under study, using high-pressure, liquid hydrogen, adsorbed or absorbed hydrogen... In particular, a large number of investigations are conducted concerning the storage by absorption of hydrogen in metals. Such phenomenon was discovered in the 19th century. Deville and Troost in 1863 carried out experiments on iron and platinum, observing the permeability to hydrogen of transition metals. In 1866, the Scottish chemist Thomas Grahan[5] observed the hydrogen insertion into palladium. He discovered that a large volume of hydrogen were absorbed by a small volume of palladium[3,6,7].

Currently, the metal-hydrogen (MH) and intermetallic compound-hydrogen (IMCH) systems are known to be of great practical interest for different applications such as gaseous storage of hydrogen and metal-hydride batteries[8–10]. There are numerous works about the subject of MH and IMCH in the literature. Various metals are used for hydrogen absorption, but the palladium is probably the most studied[10–19]. Palladium represents a model system from which the main features of most hydride forming metals or IMC can be derived[7,10].

3.2 Pd bulk

Solid insertion is an important phenomenon in chemistry, specifically in physical-chemistry. Absorption of gas molecules into the solid is indicated by the decrease of pressure. In the case of palladium, hydrogen insertion can be obtained also in electrochemical environment, as firstly reported by Thomas Graham (1868). When applying a certain potential to a Pd sample, hydrogen insertion into the metal will occur from proton in the solution. From the quantity of inserted hydrogen, either

from gas phase or in electrolytic solution, it is possible to build a thermodynamic relationship called insertion isotherm. At constant temperature, it is defined by the ratio between the number of inserted hydrogen atoms and the Pd ones [20,21] versus the gas pressure or the electrochemical potential.

3.2.1 Pd bulk hydrogen insertion-desorption isotherm

The insertion isotherm is experimentally measured at constant temperature. The goal of this measurement is to quantify the hydrogen inserted into a metallic sample. Figure 3.1 is the hydrogen insertion isotherm in bulk Pd, showing the number of inserted H atoms per Pd atoms as a function of the electrochemical potential.

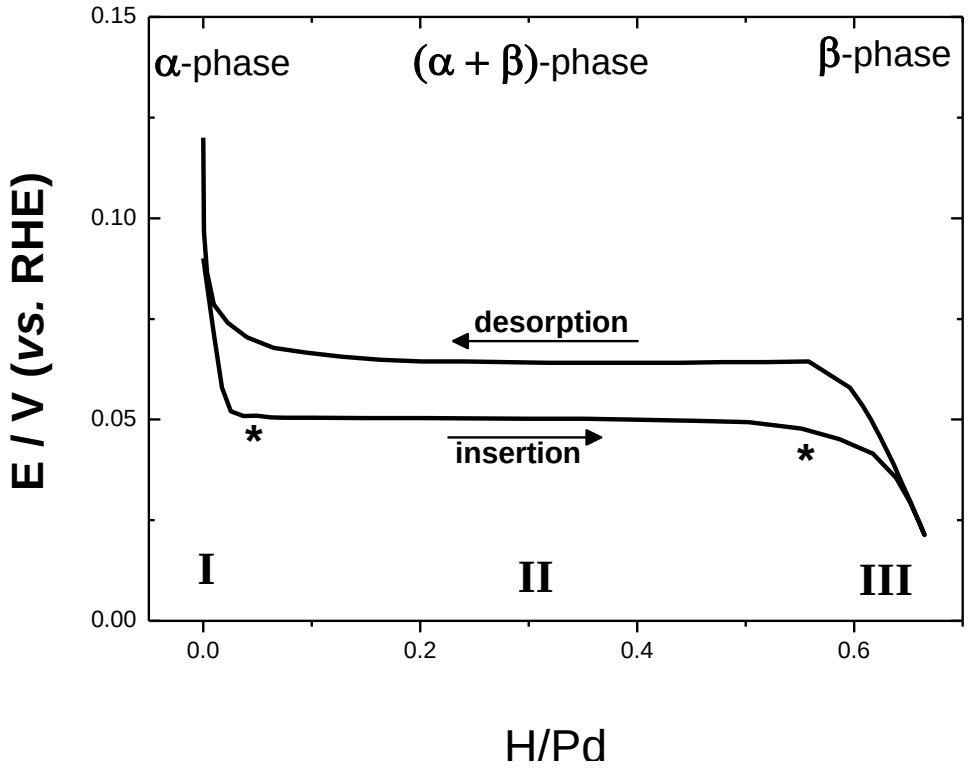

Figure 3.1 : Isotherm of hydrogen insertion into palladium bulk[10].

The asterisks separate 3 distinct regions related to different phases of the Pd-H system[10]. For low hydrogen concentrations, only the α-phase (Figure 3.1 - I) is present, corresponding to a solid solution. As concentration increases beyond α_{max} (* about 0.05 H/Pd) the β phase appears, corresponding to hydride formation, and

coexisting with the α phase. This zone is the so called two-phase region and is characterized by the increase of hydrogen insertion at constant potential. For concentrations higher than β_{min} (* about 0.55 H/Pd) only the β-phase is present (Figure 3.1 – III) and a solid solution forms.

Gibbs law

The presence of two phases in the hydrogen insertion isotherm of bulk Pd obeys the phase rule deduced by Josiah Willard Gibbs[22,23]. The Gibbs phase rule is represented by the (Equation 3.1).

$$f = (C - P + 2) \qquad \textbf{(Equation 3.1)}$$

where f is the degree of freedom, C is the number of components and P is the number of phases. In the α–phase, the system has two degree of freedom (f=2), i.e. the hydrogen concentration increases with the variation of potential. In the two phase region, the Pd/H system has 3 phases (α, β and hydrogen in solution) and two components (palladium and hydrogen). The system has just one degree of freedom. This means that the coexistence of two phases for a fixed value of temperature corresponds to only one potential value. Therefore, in the two-phase region (II) the concentration increases while the hydrogen potential (pressure) is constant. Once β_{min} is reached, with the complete disappearance of the α-phase, the system has two degrees of freedom again. The hydrogen passes to solid solution in the β-phase and the hydrogen potential (pressure) rises with concentration[22,24].

Temperature effect

Temperature is a very important parameter for hydrogen insertion isotherm. Figure 3.2 shows the evolutions of the isotherms versus temperature.

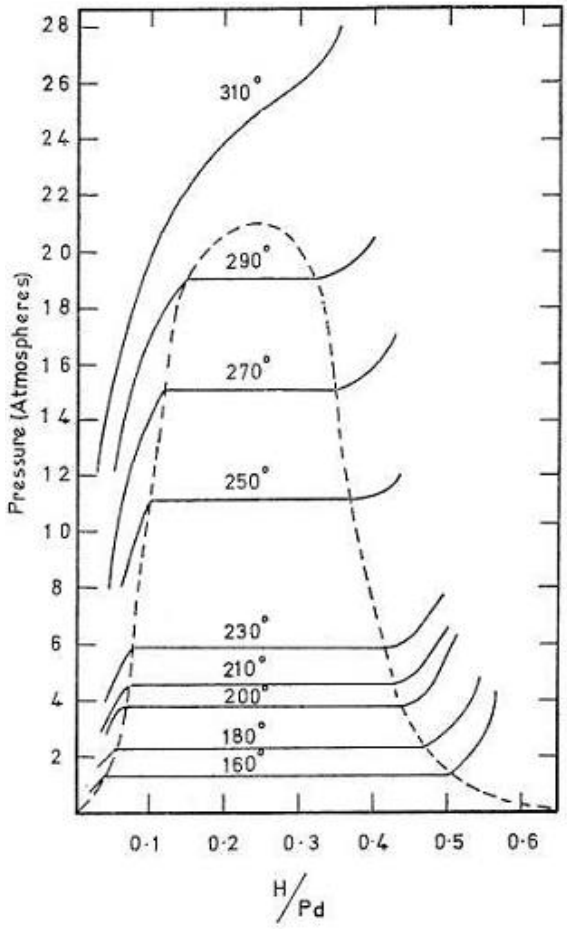

Figure 3.2 : The phase diagram for isotherm of hydrogen insertion versus temperature[3].

The isotherm profile is changing while increasing the temperature: the two-phase domain width reduces, α_{max} increases and β_{min} decreases (at room temperature $\alpha_{max} = 0.025$ and $\beta_{min} = 0.550$). In particular, beyond the critical temperature the plateau disappears (T=310 °C) and only one phase is present. Figure 3.2 shows that the temperature deeply influences also the maximum hydrogen insertion rate. The increase of the temperature causes a decrease of the total amount of inserted hydrogen.

Phases properties

The hydrogen inserted into bulk palladium samples induces large distortions in the crystal lattice, with deterioration of the metal morphology. Figure 3.3 shows the structural macroscopic changes caused by hydrogen insertion into a palladium foil.

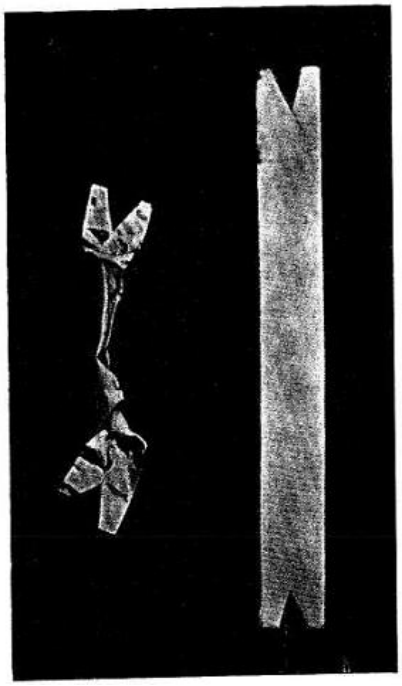

Figure 3.3 : Morphology of palladium (left) after 30 cycles of insertion/desorption, (right) sample of palladium alloy with the same geometric area of palladium before experiment[3].

One can observed the strong deformations after (left) and before (right) 30 cycles of full insertion/desorption. This cycling caused the irreversible changes in the Pd sample. One can see it strongly after 30 cycles. The degradation effect is related to the volume increase generated by hydrogen phase transformation. To understand this effect it is necessary to have more details on the process of the hydrogen insertion inside the Pd sample.

In the fcc lattices, the hydrogen atoms can occupy the space between the Pd atoms, it is called the specific interstitial sites. However, there are two forms in which H atoms can accommodate: octahedral (O) and tetrahedral (T) sites. Figure 3.4 shows the hydrogen (black ball) on Pd (gray ball) in the different sites of the crystal structures.

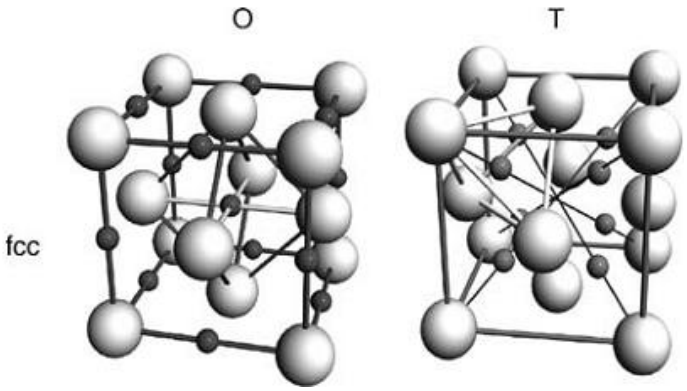

Figure 3.4 : Interstitial octahedral (O) and tetrahedral (T) sites in face centered cubic (fcc) lattice. Black balls are hydrogen atoms and gray balls are palladium atoms[24].

In the scheme, one can see that the hydrogen interaction with Pd is very different depending on the site position in the lattice. Only neutron diffraction measurements allowed seeing hydrogen position.

At low or medium concentration, neutron diffraction on the deuterium insertion into bulk Pd has shown that D atoms preferentially occupy the octahedral sites of the fcc lattice in the α and β phases[7,24,25]. It is than generally assumed that H atoms occupy the same sites, even if the behavior may change for each isotopic specie[3,25].

Hydrogen insertion into palladium in the α-phase does not induce important changes on the lattice parameters. Values for the lattice parameters are very close, *a*(bulk Pd) = 3.890 Å and *a*(Pd α phase) = 3.894 Å. This is not the case for the β–phase, which is characterized by a much larger lattice parameter, *a*(Pd β phase) = 4.025 Å. This corresponds to the fact that hydrogen insertion induces a volume increase of around 10%. This fact causes huge stresses in the Pd structures and produces defects. At each cycle of insertion/desorption, new defects are added to the sample, making mechanical transformation and after many cycles, the sample is completely deformed.

Hysteresis in the hydrogen insertion/desorption isotherm

The hysteresis in the cycles of hydrogen insertion/desorption in bulk Pd was observed for the first time by Brodowsky and Paeschel (1965). They noted the hysteresis phenomenon between the absorption and desorption isotherms over the regions where the α → β–phase and β → α–phase transformations occur. Figure 3.5

shows the scheme of a generic isotherm, where it is possible to note the hysteresis phenomenon.

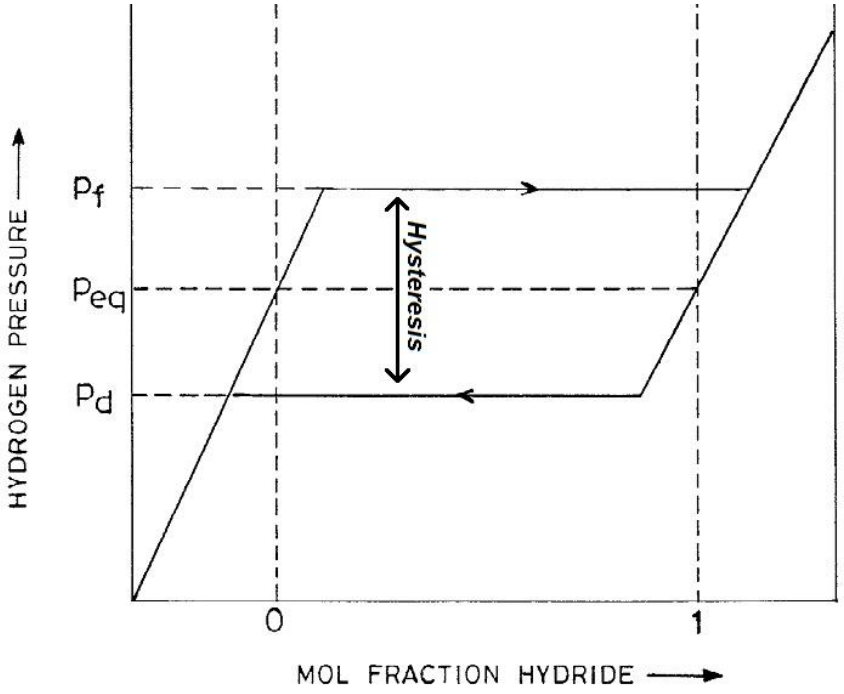

Figure 3.5 : Schematic pressure–composition isotherm[26].

In this isotherm the absorption plateau is at a higher pressure than the desorption plateau, thus forming a hysteresis. The phenomenon has been attributed to dissipative phenomena such as the generation of a large density of misfit dislocations. In this case, it is due to the volume increase caused by different lattice parameters between the phases α and β[26–28].

The hysteresis is a common, although somewhat neglected, phenomenon in solid state chemistry and physics and is of both fundamental and technological significance. It occurs in structural transformations, phase separation transformations and some order/disorder phenomena. This subject is largely discussed in the literature[3,24,26,28–33].

For practical applications, hysteresis is an important feature, because it has an important impact on the storage. In fact, it could translate to a loss in the efficiency of the material due to irreversible deformation during absorption and desorption of hydrogen.

3.2.2 Thermodynamic

Gas Phase

In the gas phase, the metallic sample is put in contact with hydrogen gas (H_2). Hydrogen molecules interact with the metal surface. Exposure of a metal surface to gaseous hydrogen can lead to a variety of phenomena ranging from a weak (molecular) adsorption called physisorption, activated atomic (dissociative) adsorption, and to spontaneous dissociative chemisorption which may be accompanied by the population of so-called subsurface sites and eventually by the formation of hydride compounds. In all these cases, the primary step must be the collision of a H_2 molecule with the solid surface, followed by trapping. Dissociative adsorption is the more interesting phenomenon. (Equation 3.2) shows the dissociation process[7,34,35]:

$$\mathrm{H_{2\,(gas)}} + 2\mathrm{M} \leftrightarrows \mathrm{M-(H-H)_{(ads)}} - \mathrm{M} \leftrightarrows 2\mathrm{M-H_{(ads)}} \qquad \textbf{(Equation 3.2)}$$

Once the hydrogen molecules are adsorbed and dissociated by the metallic surface, they diffuse into the metal:

$$2\mathrm{M-H_{(ads)}} \leftrightarrows 2\mathrm{M-H_{(abs)}} \qquad \textbf{(Equation 3.3)}$$

- **Thermodynamic**

At equilibrium, the chemical potential of hydrogen absorbed in the metal $\mu_{H(abs)}$ is equal to the one of hydrogen gas$\mu_{\mathrm{H(g)}}$:

$$\mu_{\mathrm{H(abs)}} = \mu_{\mathrm{H(g)}} \qquad \textbf{(Equation 3.4)}$$

The chemical potential of hydrogen dissolved in metal can be set equal to

$$\mu_{\mathrm{H(abs)}} = \mu_{\mathrm{H}}^{0} + \mathrm{RT}\ln\left(\frac{\mathrm{H/M}}{(1-\mathrm{H/M})}\right) + \Delta\mu_{\mathrm{H}} \qquad \textbf{(Equation 3.5)}$$

Where μ_H^0, is the standard chemical potential, R is the gas constant and T is the temperature. $\Delta\mu_H$ stands for the deviations from the ideal solution behavior[7], where hydrogen atoms have a statistic distribution on the insertion sites.

In the case of solution in equilibrium with hydrogen gas we have:

$$\mu_{H(g)} = \frac{1}{2}\,\mu_{H_2} = \frac{1}{2}\,(\,\mu_{H_2}^0 + RT\ln P_{H_2}) \qquad \textbf{(Equation 3.6)}$$

Where, $\mu_{H_2}^0$ is standard chemical potential of gas hydrogen and P_{H_2} is partial pressure of hydrogen in equilibrium. Introducing Sieverts' constant

$$K = \exp\left(\frac{\mu_H^0 - \frac{1}{2}\,\mu_{H_2}}{RT}\right) \qquad \textbf{(Equation 3.7)}$$

one obtains:

$$\ln\left(\sqrt{P_{H_2}}\right) = \ln\left(K\,\frac{H/M}{(1-H/M)}\right) + \frac{\Delta\mu_H}{RT} \qquad \textbf{(Equation 3.8)}$$

In the ideal solution state case, the $\Delta\mu_H/RT$ term is negligible. This is true for low hydrogen insertion rates, i.e. in the α–phase. (Equation 3.9) represents the Sieverts' law

$$\sqrt{P_{H_2}} = K\,\frac{H/M}{(1-H/M)} \qquad \textbf{(Equation 3.9)}$$

With H/Pd << 1, in the α–phase

$$\sqrt{P_{H_2}} = K\,\frac{H}{Pd} \qquad \textbf{(Equation 3.10)}$$

Liquid Phase

Two mechanisms are proposed for hydrogen absorption in electrochemical solution: direct and indirect insertion. The direct absorption mechanism was postulated by Bagotskaya and later by Frumkin. It considers that hydrogen atoms

directly enter into the metal, without going through an intermediate adsorbed state[36]. This mechanism is described by (Equation 3.11):

$$H^+ + e^- + M \leftrightarrows M - H_{(abs)} \quad \textbf{(Equation 3.11)}$$

Another postulated absorption mechanism is composed by two steps[35], as shown in (Equation 3.12) and (Equation 3.13):

A. Adsorption step:

$$H^+ + e^- + M \leftrightarrows M - H_{(ads)} \quad \textbf{(Equation 3.12)}$$

B. Absorption step:

$$M - H_{(ads)} \leftrightarrows M - H_{(abs)} \quad \textbf{(Equation 3.13)}$$

Hydrogen evolution reaction (HER)

When the potential of the electrode is close or lower than 0 V *vs*. RHE, hydrogen evolution reaction is present. Hydrogen protons in solution are coupled on the electrode surface to form gaseous hydrogen. HER can occur following two different mechanisms, Heyrovsky (Equation 3.15) and Tafel (Equation 3.16). Nevertheless, in both cases the adsorption step precedes HER (Volmer mechanism).

(A) *Volmer*: Adsorption step

$$H^+ + e^- \leftrightarrows H_{(ads)} \quad \textbf{(Equation 3.14)}$$

(B) *Heyrovsky*: Electrochemical recombination

$$H_{(ads)} + e^- + H^+ \leftrightarrows H_{2(g)} \quad \textbf{(Equation 3.15)}$$

(C) *Tafel*: Chemical recombination

$$2H_{(ads)} \leftrightarrows H_{2(g)} \quad \textbf{(Equation 3.16)}$$

Some authors consider the Volmer-Heyrovsky[37] path as predominant, whereas others consider Volmer-Tafel[38]. However, it is important to note that in the case of hydride formation, one part of hydrogen adsorbed on the electrode surface

will diffuse into the Pd sample, and the other part will recombine to form hydrogen gas.

Relation between electrochemical and gas-phase hydrogen isotherms

As it was presented previously, the hydrogen insertion for gas phase (Equation 3.2 and (Equation 3.**3**) and liquid phase (Equation 3.11, (Equation 3.**12** and (Equation 3.**13**), it is possible to associate the two phases.

We consider the reaction simplified bellow

Gas Phase: $$H^+ + e^- \rightleftarrows H_{(abs)}$$ **(Equation 3.17)**

Liq. Phase: $$^1/_2\ H_{2\,(gas)} + e^- \rightleftarrows H_{(abs)}$$ **(Equation 3.18)**

In the equilibrium, the chemical potential in the equilibrium system can get:

Gas Phase: $$\mu^E_{H^+} + \mu^E_{e^-} = \mu_{H_{(abs)}}$$ **(Equation 3.19)**

Liq. Phase: $$\frac{1}{2}\mu_{H_{2(gas)}} = \mu_{H_{(abs)}}$$ **(Equation 3.20)**

Combining equations (Equation 3.19) and (Equation 3.20), yields:

$$\frac{1}{2}\mu_{H_{2(gas)}} = \mu^E_{H^+} + \mu^E_{e^-}$$ **(Equation 3.21)**

with:

$$\mu_{H_2} = \mu^0_{H_2} + RT\ln\frac{P_{H_2}}{P^0}$$ **(Equation 3.22)**

Where $P^0 = 1\ \mathrm{atm}$. It has to close the standard for measuring electrochemical potential and chemical potential. If electrode potential is quoted against RHE, it means the solutions are the same for working electrode (WE) and reference electrode (RE). For the gas, we define that $\mu_{H_2} = 0$, when $P_{H_2} = P^0$.

$$\frac{1}{2}\mu_{H_{2(RHE)}} = \mu^{E}_{H^+(RHE)} + \mu^{E}_{e^-(RHE)} \quad \textbf{(Equation 3.23)}$$

When the solution is the same, $\mu^{E}_{H^+(RHE)} = \mu^{E}_{H^+}$, and $P_{H_2} = P^0$. From the (Equation 3.22), one has $\mu_{H_{2(RHE)}} = \mu^{0}_{H_2}$, using these in the (Equation 3.23).

$$\frac{1}{2}\mu^{0}_{H_2} = \mu^{E}_{H^+} + \mu^{E}_{e^-(RHE)} \quad \textbf{(Equation 3.24)}$$

By junction of (Equation 3.22) and (Equation 3.24).

$$\mu^{E}_{H^+} - \mu^{E}_{e^-(RHE)} = \frac{RT}{2}\ln\frac{P_{H_2}}{P^0} \quad \textbf{(Equation 3.25)}$$

So

$$-F(E_{vs.\,RHE}) = \frac{RT}{2}\ln\frac{P_{H_2}}{P^0} \quad \textbf{(Equation 3.26)}$$

And one can get:

(R = 8.314 J·K^{-1}·mol^{-1}; T = 298 K and F = 9.648·10^4 C·mol^{-1})

$$E_{vs.\,RHE} = -\frac{RT}{2F}\ln\frac{P_{H_2}}{P^0} = -0.0296 \cdot \log\frac{P_{H_2}}{P^0} \quad \textbf{(Equation 3.27)}$$

According to this equation, the equilibrium potential and equilibrium hydrogen pressure can be associated by the (Equation 3.27).

3.3 Pd nanoparticles

The discovery of new size-related physical properties for nano-structured materials has induced many studies in fundamental research and for applications in industrial domains, such as in catalysis. Nanoparticles are typically supported on substrates (for instance polymers, carbon powder, carbon nanotubes, etc.) to prevent

the particles agglomeration[39–44], even if Pd-clusters can be found in the non-supported form[10,15,16,45–48].

Figure 3.6 shows the hydrogen insertion isotherms for Pd nanoparticles of different sizes.

(A)

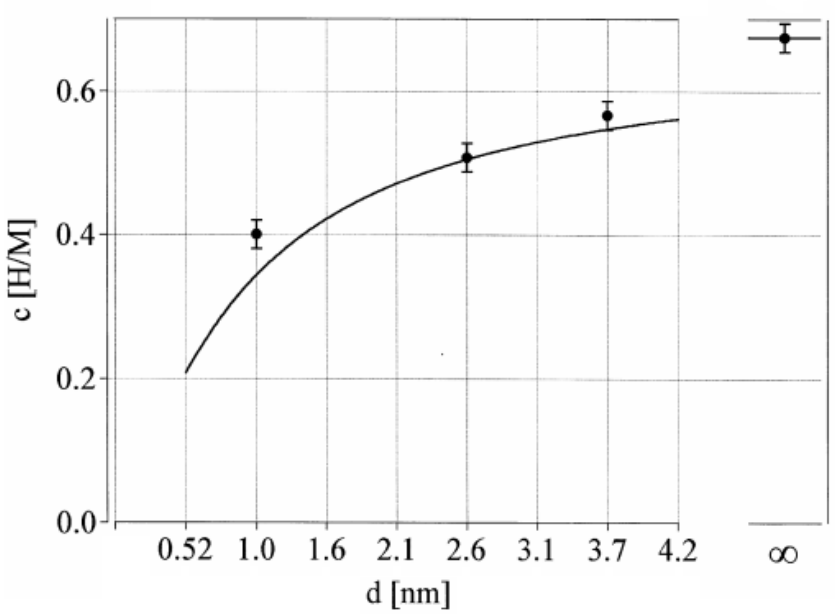

(B)

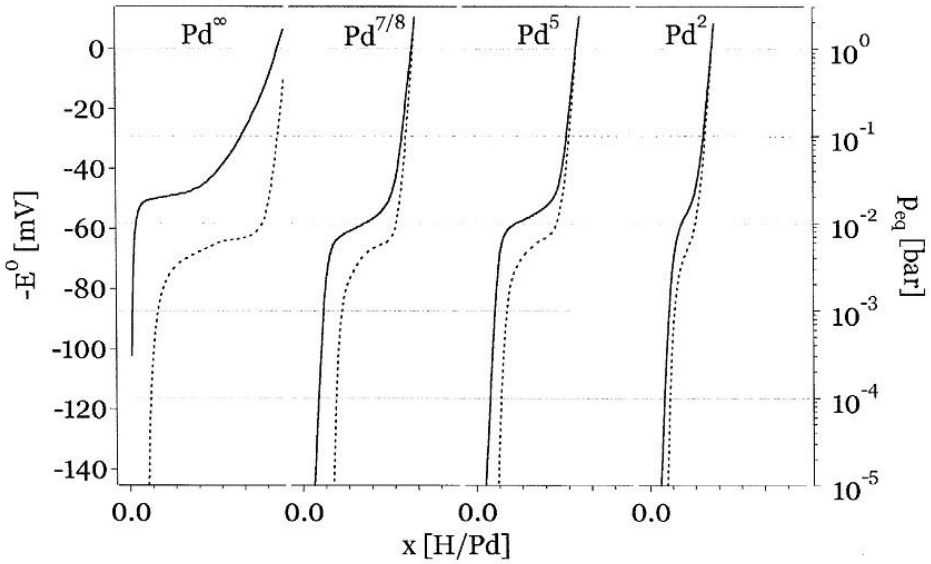

Figure 3.6 : (A) Hydrogen capacity as a function of Pd clusters size. The line represents the calculated capacity and the markers stand for the measured capacities. Bulk Pd is placed at an infinite number of shells. 100% of capacity corresponds to (H/Pd) = 0.67[46]. (B) Equilibrium pressure isotherms for crystalline Pd bulk (~50 µm) and $Pd^{7/8}$ (3.7 – 4.2 nm), Pd^{5} (2.6 nm), Pd^{2} (2 nm) clusters. Solid lines represent absorption and broken lines represent desorption[47].

Zuttel et al.[46] investigated the hydrogen interaction with Pd–clusters with size range of 55 atoms (1 nm) up to bulk Pd (50 mm). Pd–clusters were hydrided and dehydrided in gas phase. X–ray diffraction pattern of the clusters was checked before and after hydrogenation, revealing the stability of these samples structures upon hydrogenation. The authors calculated the capacities for different cluster sizes using

closed shell model (cuboctahedron, icosahedron), assuming that the fcc structure offers 1 octahedral and 2 tetrahedral interstitial sites per metal atom for hydrogen and with the simple assumption that surface atoms provide less interstitial sites for hydrogen. They obtain 0.25 H/M (H atoms per metal atom) at corners, 0.4 H/M at edges and 0.5 H/M at faces. The total hydrogen insertion rate is shown in Figure 3.6 – A, nicely corresponding to the experimental results. As a conclusion they find that the hydrogen capacity increases with the Pd–clusters size. From the density of states calculations (DoS), they also found that the critical temperature for the hydride formation of the clusters is probably size dependent and decreases with decreasing cluster size. In another work[47] the same authors evaluated the thermodynamic aspects of the interaction of hydrogen with Pd–clusters. The absorption (solid line) as well as desorption (broken line) hydrogen isotherms are shown in Figure 3.6 – B for all the investigated Pd–samples. The capacity, i.e. the concentration at the end of the plateau, decreases with decreasing cluster size. According to the authors, the increasing ratio of surface atoms to volume atoms with decreasing cluster size leads to the decreasing reversible hydrogen capacity. However, the hysteresis between the absorption and the desorption decreases with decreasing cluster size.

Pundt et al.[15] studied the structural effect on the Pd-clusters (3.0 and 5.2 nm) of the hydrogen insertion using X-ray powder diffraction. The authors concluded that the Pd–H clusters isotherms drastically differ from the one of the Pd–H bulk system. Indeed, they look similar to the bulk Pd isotherms recorded above the critical point. Their results show an increased solubility in the low concentration range (α_{max}), a decreased solubility in the high concentration range (β_{min}) and a sloped isotherm in the two-phase domain. They attributed the changes in the solubility to the hydrogen sorption in subsurface sites. Measurements of hysteresis have shown that phase transitions must occur in clusters even though the isotherms show no flat plateau region. In Pd bulk the hysteresis phenomenon was understood as resulting from dislocations generation and movement during the phase transition[29,49]. However, in small clusters dislocations will not occur and the hysteresis in cluster isotherms must have a different origin[15]. Pundt et al.[15] attributed the ‘sloped plateau’ of clusters to mechanical stress occurring between the Pd-cluster and its surfactants during hydrogen sorption.

Yamauchi and Kitagawa[43] studied the hydrogen absorption of Pd nanoparticles dispersed in a coated polymer (polyvinylpyrrolidone – PVP). Transmission Electron Microscopy (TEM) images show particles with average size equal to 2.6±0.4 nm. The hydrogen insertion into the Pd nanoparticles was recorded in gas phase. According to the authors, the hydrogen solubility of the hydride phase in the Pd-PVP (0.5 H/Pd) was slightly smaller than for Pd bulk (0.67 H/Pd). They ascribe such finding to the large surface area and to peculiar electronic state of the nanoparticles.

Lebouin et al.[10] studied the hydrogen insertion into palladium nanofilms supported on Pt(111). They compared the isotherm behavior of the nanofilms (16 ML) to the one of non-suported nanoparticles (3.6 nm). They concluded that the parameters α_{max}, β_{min} and $(H/Pd)_{max}$ described in the isotherms were very close. They deduced that different nano-sized systems characterized by similar dimensions and surface/volume ratio seem to have close thermodynamic values for hydrogen insertion. On the contrary, a different behavior has been observed for the two-phase region, characterized by a slope five times higher for nanofilms. The authors attributed the slope in the Pd films to the constraints due to the substrate.

3.4 Pd nanofilms

The materials that exhibit large capacities for hydrogen storage have typically two main drawbacks, the low kinetic for di-hydrogen bond breaking and a high sensitivity to oxidation. In this case, Pd films may be associated as a protecting barrier with a metal hydride electrode having high hydrogen storage capacity. Thanks to its large permeability to hydrogen atoms, Pd film can enhance the hydrogen permeation and act as a protective membrane against oxygen[50–55].

Of course very thin Pd films are expected to present original properties compared to bulk Pd. As discussed in chapter I, several studies have been made on the Pd deposition onto single crystals, and in particular onto platinum. The various authors have underlined the separation between adsorption and insertion signals for Pd/Pt(111) and Pd/Pt(100) films. Nevertheless, very few studies have been dedicated to the phenomenon of hydrogen electro-insertion into Pd/Pt(111)[10,19,56], while as far as we know no contribution is present in the literature for Pd/Pt(100)–H.

Figure 3.7 shows the comparison of hydrogen insertion isotherms for bulk Pd and for Pd films with 10 and 16 ML as equivalent thickness deposited on Pt(111)[10].

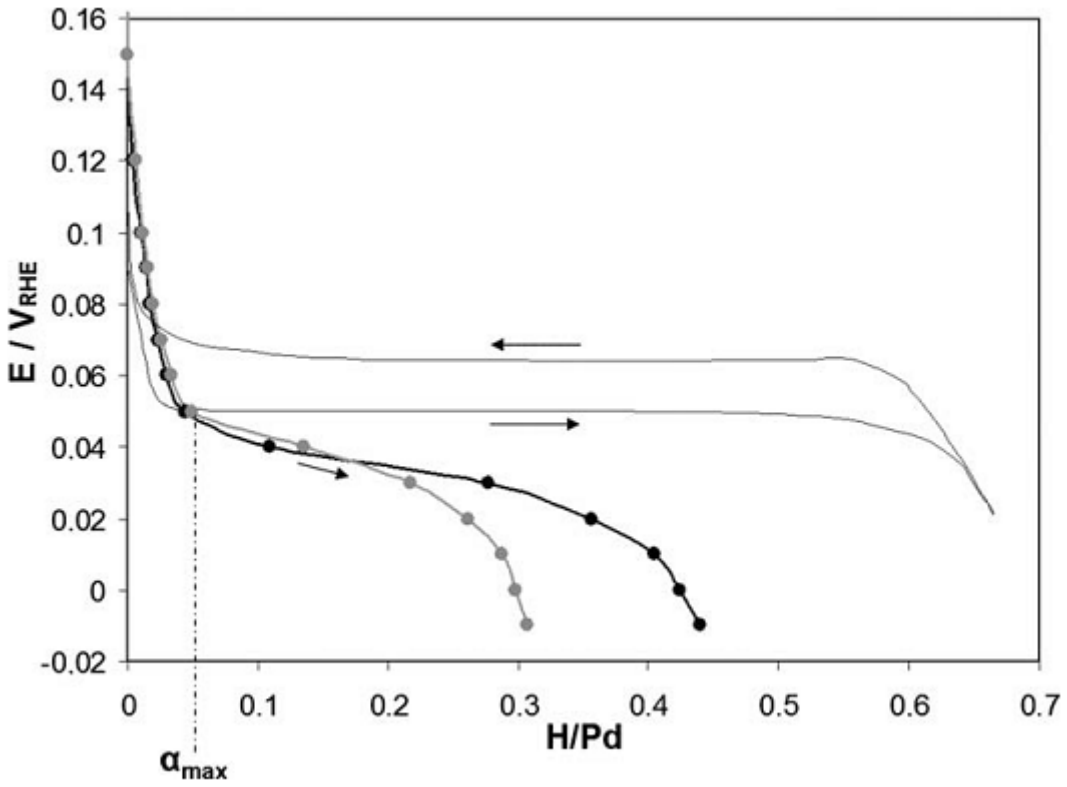

Figure 3.7 : Experimental hydrogen electrochemical isotherms in H_2SO_4 0.1 M: Pd_{10ML}/Pt(111) (continuous line with gray dots) and Pd_{16ML}/Pt(111) (continuous line with black dots)[10]. Bulk Pd (gray line) is shown as well[10].

The maximum hydrogen insertion rate $(H/Pd)_{max}$ is close to 0.7 for bulk Pd. In Pd films this rate is reduced to 0.43 and to 0.3 in 16 ML and 10 ML, respectively. In opposite, α_{max} is slightly larger in nanofilms compared with bulk Pd. The biphasic domain width is also reduced. The Pd films show similar phenomena as observed on Pd nanoparticles[47] in relation to the α_{max} and β_{min} values and to the total amount of inserted hydrogen as a function of the insertion length.

Nevertheless Lebouin et al.[10] could not measure isotherms for thicknesses smaller than about 10 ML, due to the parallel HER contributions interfering in the inserted hydrogen amount calculation. Such phenomenon can be neglected for the thicker films, thanks to their high hydrogen insertion capacity. But this contribution becomes significant when the amount of inserted hydrogen is comparable with the amount of hydrogen produced with HER during the measurement.

We will present in the next chapter a new method that we have developed in order to measure electrochemical isotherms for very thin Pd/Pt(111) films thanks to the use of the hanging-meniscus rotating disk electrode allowing a better control of the $H_{2(g)}$ contribution and finally its elimination.

We will also show the results obtained on the isotherms for Pd/Pt(100) films and we will compare the two studied systems.

3.5 Conclusion

We have discussed the properties of the isotherm obtained for hydrogen insertion into bulk Pd at room temperature. The solid solution (α phase) at very low hydrogen insertion rates is followed by the coexistence of the α and β (hydride) phases. This so called two-phase region is characterized by an increase of the hydrogen insertion rate at constant potential (pressure). At higher insertion rates, palladium is completely hydrided. A hysteresis phenomenon is present between insertion and desinsertion branches.

Nanoparticles are characterized by smaller maximum hydrogen insertion rates compared to bulk Pd, decreasing with the size. The hysteresis phenomenon decreases with the clusters size as well.

In the same way, Pd ultra-thin films deposited onto Pt(111) present a smaller total amount of inserted hydrogen, its value decreasing with thickness. Nevertheless, the isotherms are characterized by a slope in the two-phase region, which has been attributed to the substrate induced constraints. No experimental isotherms are present in the literature for films thinner than 10ML, where HER contribution becomes non-negligible and hinders a correct evaluation of the amount of inserted hydrogen.

As far as we know, no studies are present in the literature on the Pd/Pt(100)-H system.

3.6 References

(1) Züttel, A. *Die Naturwissenschaften* **2004**, *91*, 157–72.

(2) Schlapbach, L.; Züttel, A. *Nature* **2001**, *414*, 353–8.

(3) Lewis, F. A. *The palladium hydrogen system*; Academic Press Inc., 1967.

(4) Walker, G. *Solid-state hydrogen storage materials and chemistry*; Woodhead Publishing Limited, 2008.

(5) Graham, T. *Philosophical Transactions of the Royal Society of London* **1866**, *156*, 399–439.

(6) Manchester, F. D.; San-Martin, A.; Pitre, J. M. *Journal of Phase Equilibria* **1994**, *15*, 62–83.

(7) Wicke, E.; Brodowsky, H.; Ztichner, H. *Hydrogen in Metals II*; Alefeld, G.; Völkl, J., Eds.; Springer Berlin Heidelberg: Berlin, Heidelberg, 1978; Vol. 29.

(8) Goodell, P. D.; Rudman, P. S. *Journal of the Less Common Metals* **1983**, *89*, 117–125.

(9) Sakai, T. *Journal of The Electrochemical Society* **1990**, *137*, 795.

(10) Lebouin, C.; Soldo-Olivier, Y.; Sibert, E.; Millet, P.; Maret, M.; Faure, R. *Journal of Electroanalytical Chemistry* **2009**, *626*, 59–65.

(11) Bernardini, M.; Comisso, N.; Fabrizio, M.; Mengoli, G.; Randi, A. *Journal of Electroanalytical Chemistry* **1998**, *453*, 221–230.

(12) Czerwiński, A.; Kiersztyn, I.; Grdeń, M. *Journal of Electroanalytical Chemistry* **2000**, *492*, 128–136.

(13) Czerwiński, A.; Kiersztyn, I.; Grdeń, M.; Czapla, J. *Journal of Electroanalytical Chemistry* **1999**, *471*, 190–195.

(14) Gabrielli, C.; Grand, P. P.; Lasia, A.; Perrot, H. *Electrochimica Acta* **2002**, *47*, 2199–2207.

(15) Pundt, A.; Suleiman, M.; Bähtz, C.; Reetz, M. T.; Kirchheim, R.; Jisrawi, N. M. *Materials Science and Engineering: B* **2004**, *108*, 19–23.

(16) Suleiman, M.; Faupel, J.; Borchers, C.; Krebs, H.-U.; Kirchheim, R.; Pundt, a. *Journal of Alloys and Compounds* **2005**, *404-406*, 523–528.

(17) Tateishi, N.; Yahikozawa, K.; Nishimura, K.; Suzuki, M.; Iwanaga, Y.; Watanabe, M.; Enami, E.; Matsuda, Y.; Takasu, Y. *Electrochimica Acta* **1991**, *36*, 1235–1240.

(18) Lebouin, C.; Soldo-Olivier, Y.; Sibert, E.; De Santis, M.; Maillard, F.; Faure, R. *Langmuir* **2009**, *25*, 4251–5.

(19) Soldo-Olivier, Y.; Lafouresse, M. C.; De Santis, M.; Lebouin, C.; De Boissieu, M.; Sibert, E. *The Journal of Physical Chemistry C* **2011**, *115*, 12041–12047.

(20) Holman, R. W. *Journal of Chemical Education* **1995**, *72*, A151.

(21) Myers, A. L. *Thermodynamics of Adsorption*; RSC, 2004.

(22) Castellan, G. W. *Physical Chemistry*; 3rd ed.; Addison-Wesley Publishing Company, Inc., 1983.

(23) Atkins, P.; Paula, J. D. E. *Physical Chemistry*; PRESS, O. U., Ed.; 8th ed.; 2006.

(24) Hirscher, M. *Handbook of Hydrogen Storage*; Hirscher, M., Ed.; Wiley-VCH Verlag GmbH & Co. KGaA: Weinheim, Germany, 2010.

(25) Lässer, R.; Klatt, K. *Physical Review B* **1983**, *28*, 748–758.

(26) Balasubramaniam, R. *Journal of Alloys and Compounds* **1997**, *253-254*, 203–206.

(27) Millet, P. *Electrochemistry Communications* **2005**, *7*, 40–44.

(28) Schwarz, R. B.; Khachaturyan, A. G. *Acta Materialia* **2006**, *54*, 313–323.

(29) Schwarz, R. B.; Khachaturyan, A. *Physical Review Letters* **1995**, *74*, 2523–2526.

(30) Flanagan, T. B.; Clewley, J. D. *Journal of the Less Common Metals* **1982**, *83*, 127–141.

(31) Flanagan, T. B.; Park, C. N.; Everett, D. H. *Journal of Chemical Education* **1987**, *64*, 944.

(32) Flanagan, T. B.; Park, C.-N.; Oates, W. A. *Progress in Solid State Chemistry* **1995**, *23*, 291–363.

(33) Rabkin, E.; Skripnyuk, V. M. *Scripta Materialia* **2003**, *49*, 477–483.

(34) Christmann, K. *Progress in Surface Science* **1995**, *48*, 15–26.

(35) Jerkiewicz, G. *Journal of The Electrochemical Society* **1996**, *143*, 1240.

(36) Zheng, G. *Journal of The Electrochemical Society* **1995**, *142*, 154.

(37) Lasia, A. *Journal of The Electrochemical Society* **1995**, *142*, 3393.

(38) Zhang, W.-S.; Zhang, X.-W.; Li, H.-Q. *Journal of Electroanalytical Chemistry* **1997**, *434*, 31–36.

(39) Yang, Y.; Zhou, Y.; Cha, C.; Carroll, W. M. *Electrochimica Acta* **1993**, *38*, 2333–2341.

(40) Lee, C.-L. **2007**, 1313–1317.

(41) Zheng, J.-S.; Zhang, X.-S.; Li, P.; Zhu, J.; Zhou, X.-G.; Yuan, W.-K. *Electrochemistry Communications* **2007**, *9*, 895–900.

(42) Nishimiya, N.; Kishi, T.; Mizushima, T.; Matsumoto, A.; Tsutsumi, K. *Journal of Alloys and Compounds* **2001**, *319*, 312–321.

(43) Yamauchi, M.; Kitagawa, H. *Synthetic Metals* **2005**, *153*, 353–356.

(44) Rose, A.; Maniguet, S.; Mathew, R. J.; Slater, C.; Yao, J.; Russell, A. E. *Physical Chemistry Chemical Physics* **2003**, *5*, 3220.

(45) Kishore, S.; Nelson, J. A.; Adair, J. H.; Eklund, P. C. *Journal of Alloys and Compounds* **2005**, *389*, 234–242.

(46) Züttel, A.; Nützenadel, C.; Schmid, G.; Chartouni, D.; Schlapbach, L. *Journal of Alloys and Compounds* **1999**, *293-295*, 472–475.

(47) Züttel, A.; Nützenadel, C.; Schmid, G.; Emmenegger, C.; Sudan, P.; Schlapbach, L. *Applied Surface Science* **2000**, *162-163*, 571–575.

(48) Pundt, A.; Sachs, C.; Winter, M.; Reetz, M. T.; Fritsch, D.; Kirchheim, R. *Journal of Alloys and Compounds* **1999**, *293-295*, 480–483.

(49) Makenas, B. J.; Birnbaum, H. K. *Acta Metallurgica* **1980**, *28*, 979–988.

(50) Barsellini, D.; Visintin, A.; Triaca, W. E.; Soriaga, M. P. *Journal of Power Sources* **2003**, *124*, 309–313.

(51) Kumar, P.; Malhotra, L. . *Electrochimica Acta* **2004**, *49*, 3355–3360.

(52) Ambrosio, R. C.; Ticianelli, E. A. *Surface and Coatings Technology* **2005**, *197*, 215–222.

(53) Geng, M. *Journal of Alloys and Compounds* **1994**, *215*, 151–153.

(54) Geng, M. *Journal of Alloys and Compounds* **1994**, *206*, L3–L5.

(55) Visintin, A. *Journal of The Electrochemical Society* **1998**, *145*, 4169.

(56) Lebouin, C. Films d'épaisseurs nanométriques de Pd sur Pt(111): élaboration, caractérisations et étude de l'électro-insertion de l'hydrogène, PhD thesis, Grenoble University, 2008.

4 Hydrogen electro-insertion into Pd/Pt(hkl) nanofilms

In the present chapter, we will show the results of the hydrogen electro-insertion into Pd films deposited onto Pt(100) and Pt(111). The first system has been studied using an established method, where isotherms are obtained calculating the integrated charge during the positive scan. A new method using hanging meniscus rotating disk electrode has been considered for the hydrogen insertion into Pd/Pt(111), allowing the isotherm measurements for very thin samples. Finally, a third section will focus on the aging of Pd/Pt(111) films during repeated cycles of hydrogen insertion/desinsertion.

4.1 Pd/Pt(100)-H system

The methods for the preparation of Pd films have been described in Chapter 2 (paragraph 2.1). In this chapter we will focus on the measurements of the hydrogen insertion electrochemical isotherm in the acidic media 0.1 M H_2SO_4. Nanometric films of different thicknesses up to about 15 layers have been studied.

From a practical point of view, the experiment is made following several steps:

- Pt single crystal surface preparation
- Surface check in the characterization cell (0.1 M H_2SO_4, thermostated at 25 ^oC)
- Pd film preparation in the deposition cell
- Pd film check in the characterization cell

Hydrogen electro-insertion into Pd film in the characterization cell (0.1 M H_2SO_4) We have used a PAR potentiostat (model 273A).

We recall that Pt(100) surface is less compact than that of Pt (111). It exhibits different adsorption sites on the surface, as it was discussed in the Chapter 1 paragraph 1.4. Pt(100) surface structure is extremely sensitive to the cooling conditions after annealing[1] and it is also less stable than the Pt(111). Therefore, it needs even more care for its preparation and its handling.

4.1.1 Voltammogram in acidic media

Figure 4.1 shows the voltammogram profile of Pd_{5ML}/Pt(100) and Pd_{16ML}/Pt(100) films in 0.1 M H_2SO_4 solution with a scan rate at 10 $mV{\cdot}s^{-1}$.

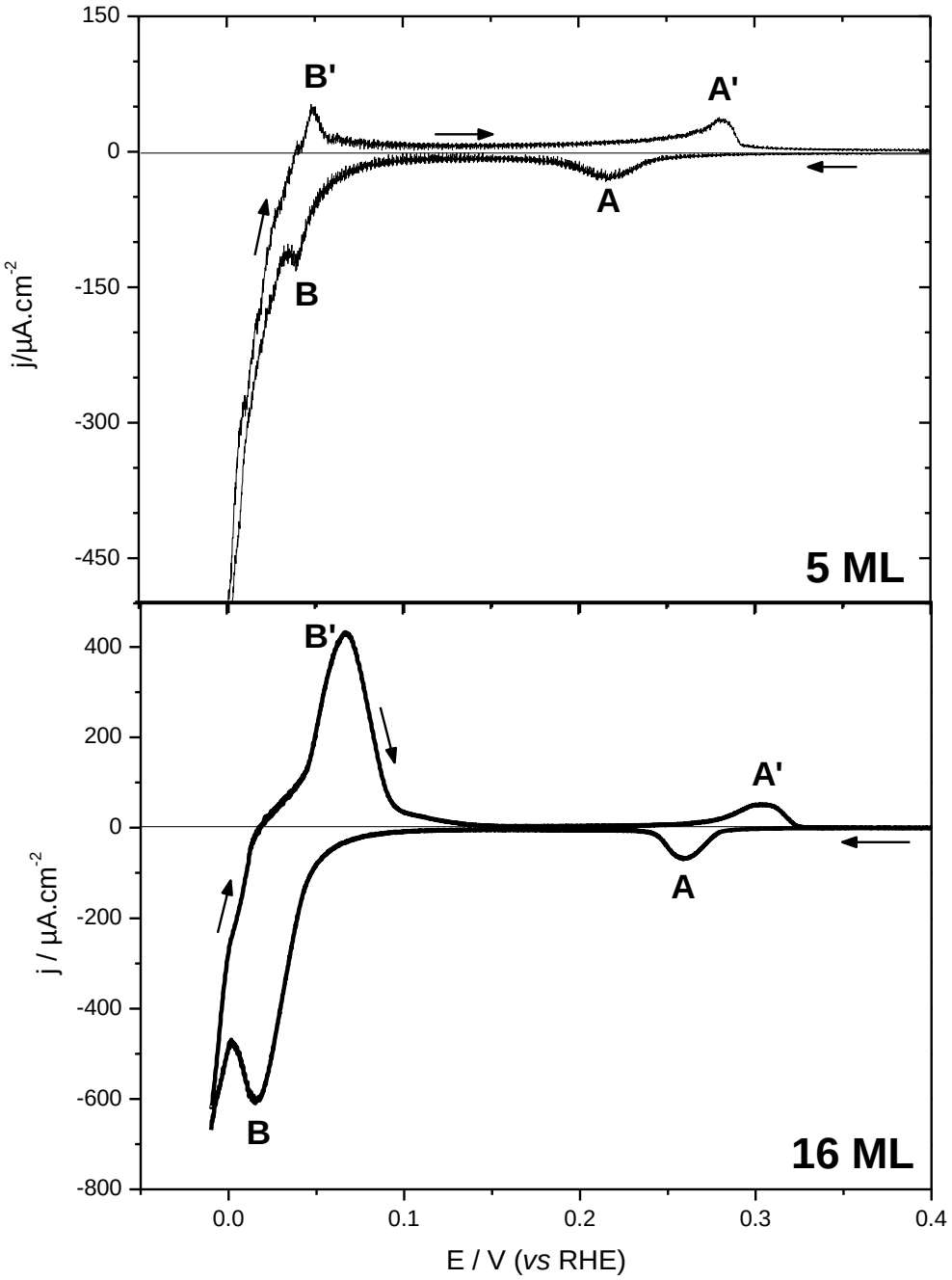

Figure 4.1 : Voltammogram profiles of Pd_{5ML}/Pt(100) and Pd_{16ML}/Pt(100) in 0.1 M H_2SO_4 at 10 $mV{\cdot}s^{-1}$.

The pair peaks A; A' has been discussed in chapter 2 paragraph 2.4. They are assigned to the adsorption/desorption reactions of anions at the surface of the Pd film. Peaks B; B' are related to hydrogen insertion and desinsertion, respectively. However, HER (hydrogen evolution reaction) and HOR (hydrogen oxidation reaction) (oxidation of H_2 generated by HER) occur in the same region. Both contribute to B; B' peaks. The potential difference between insertion and desinsertion processes. The

irreversibility of the system worsens with the film thickness, as indicated by the potential interval between the two reactions in the positive and negative scans. Such a difference points out the presence of irreversibility in the insertion process which may be related to the hysteresis observed in bulk Pd isotherms (see chapter 3 paragraph 3.2). The hysteresis seems to be more pronounced in thicker deposits.

The peaks B; B' are well defined with an overall good separation between the hydrogen insertion and the HER currents. This behavior is different compared to Pd/Pt(111), where the hydrogen insertion contribution was strongly overlapped with the HER-HOR ones (see paragraph 4.2). Even if there is still a slight overlapping of these two contributions in the positive scan, desinsertion process (peak B') is quite well separated. We will use this opportunity in the next paragraph to evaluate the amount of inserted hydrogen.

4.1.2 Experimental method to determine the inserted hydrogen amount

The most common method for the calculation of hydrogen insertion isotherm is to use cyclic potential scans[2,3]. The amount of hydrogen inserted in the sample at this potential value is found by charge integration of the desinsertion obtained during the positive scan. Figure 4.2 shows a representative scheme of this method.

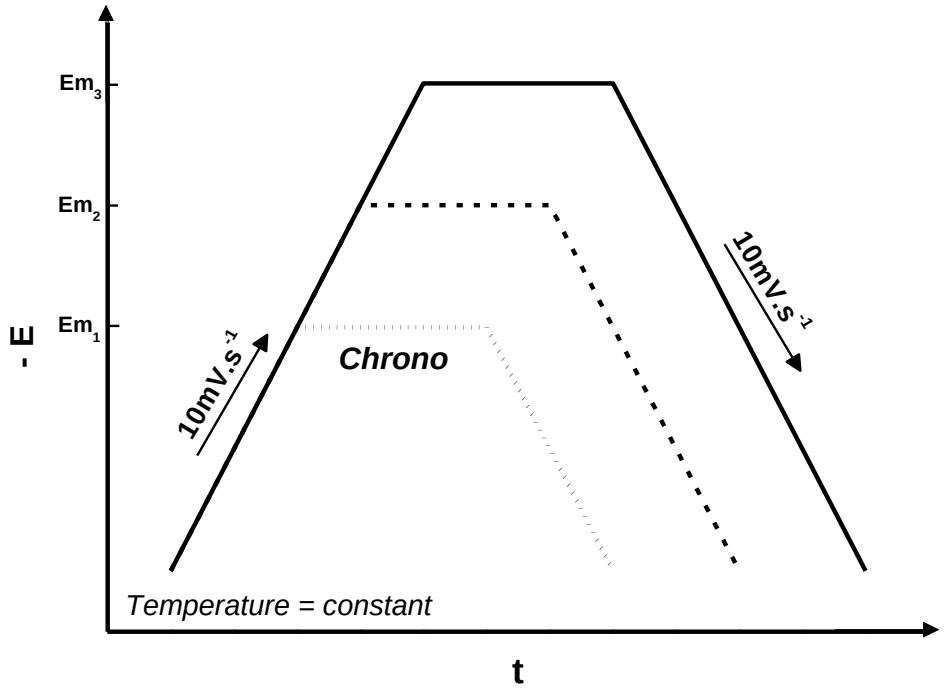

Figure 4.2 : Scheme of the experimental method followed for the calculation of the hydrogen insertion electrochemical isotherm in Pd/Pt(100) thin films. The three lines represent three different insertion potentials (dotted line E_{m1}, dashed line E_{m2}, continuous line E_{m3}). t: time; E: potential.

The potential is initially (t = 0) set in the double layer region at 0.62 V vs RHE (E_0). The potential is then decreased at 10 $mV \cdot s^{-1}$ to the potential of interest (E_m), where we want to determine the amount of inserted hydrogen. Once reached E_m, the potential is fixed at this value. A chronoamperometry is recorded until current stabilization (typically 60 sec). This measure allows to be sure that hydrogen insertion reached its limit. Afterwards, the potential is scanned back at 10 $mV.s^{-1}$ to the initial potential value E_0, allowing the hydrogen desinsertion from the sample. Considering that all the inserted hydrogen is desinserted, the charge integration in the positive scan corresponds to the quantity of inserted hydrogen at E_m. The procedure was followed for each hydrogen insertion potential considered to describe the electrochemical isotherm.

As previously explained, peak B corresponds to hydrogen insertion reaction (Figure 4.1). The calculation on the amount of inserted hydrogen could be done by integration of the charge under this peak, but the result could be impacted by the HER/HOR contribution. Indeed, HER contribution increases with potential decrease

and becomes dominant near 0 V vs RHE. For this reason, we decided to consider the hydrogen desinsertion process. This last process occurs at higher potential, compared to the insertion one. Consequently, it is better separated from HER contribution. There is still the possibility that $H_{2(g)}$ formed by HER stays in front of the electrode and, being re-oxidized at higher potential, it can modify the charge under peak B'. The solution was stirred during measurements, in order to minimize this contribution. This method has been already used for the system Pd/Pt(111)–H[2].

The charge of peak B' is calculated by integration (Equation 4.1).

$$|Q| = \frac{\left(\int_{E_z}^{E_l} i \, dE\right)}{v} \qquad \textbf{(Equation 4.1)}$$

where Q is the charge, E_z is the potential where current goes through zero value limit, E_l is the upper potential limit for integration taken equal to 0.15 V *vs* RHE, i is the current and v is the scan rate. E_l value is high enough to completely desorb the inserted hydrogen and low enough to minimize the hydrogen adsorption contribution, even if we cannot totally exclude that some hydrogen adsorption occurs at potential lower than 0.15 V vs RHE.

Finally, the ratio between the integrated desinsertion charge (one electron corresponds to one inserted hydrogen atom) and the number of deposited Pd atoms (obtained by coulometry during the films deposition) is directly the (H/Pd) value. This ratio must be calculated for each potential value E_m to build the hydrogen insertion isotherm.

4.1.3 Electrochemical isotherms

Hydrogen insertion isotherms in Pd/Pt(100) films of various thicknesses are shown in Figure 4.3.The measurements have been obtained from + 0.14 down to –0.02 V vs RHE. All (H/Pd) values have been recorded on the same sample, starting with the measurements at high potential.

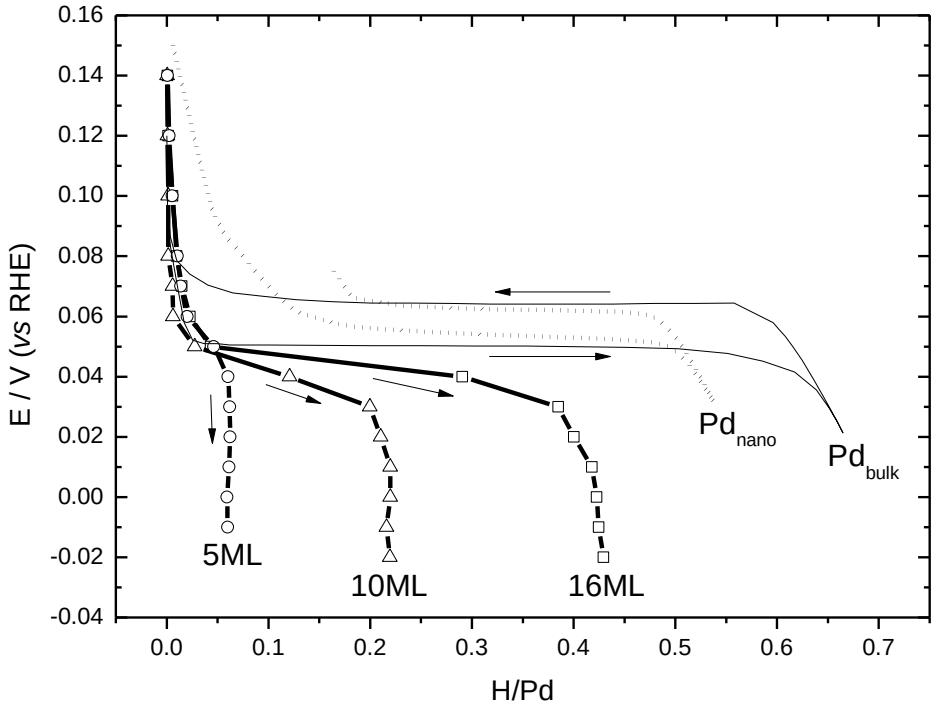

Figure 4.3 : Absorption branches of the electrochemical isotherms for Pd_{xML}/Pt(100)-H measured in 0.1 M H_2SO_4 ;(O) x = 5 ML, (Δ) x = 10 ML, (□) x = 16 ML. Bulk Pd (—)[2] and nanoparticles (diameter 3.6 nm) (⋯)[2] isotherms are also shown. T =25 °C.

Similarly to Pd bulk, Pd/Pt((100)-H isotherms can be described with 3 regions. At high potential (> 0.05 V vs. RHE) hydrogen insertion rate is low (< 0.03), corresponding to the solid solution of H in the Pd lattice (the so called α phase). The second region is associated with the rapid increase of hydrogen solubility in a narrow potential range (between 0.05 and 0.03 V vs. RHE). It presents large similarities with the two-phase region described by a plateau for bulk Pd, associated with the coexistence of the two phases (α and β). Nevertheless, for Pd/Pt(100) films this plateau is characterized by a slope. Finally, a third region at low potential (< 0.03 V vs. RHE) exhibits a nearly constant insertion rate. It corresponds to the β-phase domain.

With thickness reduction of Pd/Pt(100) film, the hydrogen insertion rate decreases in the second and third region. The maximal insertion rates $(H/Pd)_{max}$ are equal to 0.42, 0.22 and 0.06 for the 16 ML, 10 ML and 5 ML, respectively. We underline that for the thinnest films Pd_{5ML}/Pt(100) we cannot exclude non negligible contribution of HER and HOR. In opposite, the maximum insertion rate in the α-

phase has nearly the same value, $\alpha_{max} \approx 0.02$, independently of the thickness. The slope of the two-phase region decreases with thickness increase, approaching the bulk Pd behavior. For Pd_{5ML}/Pt(111), the intermediate region almost does not exist. It only consists in a rapid transition between the two outermost regions.

The isotherms of bulk Pd and Pd nanoparticles (diameter 3.6 nm) are shown in Figure 4.3 for comparison (courtesy from C. Lebouin[2]). Nanoparticles isotherm has been recorded in gas phase and converted to electrochemical isotherm using the equivalence between $H_{2(g)}$ pressure and the electrode potential. Despite the conversion, the comparison of isotherms for nanoparticles and for Pd films is not straightforward. The isotherms in gas phase include the H adsorption at the Pd surface, while the adsorption contribution to the electrochemical isotherm can be minimized by correctly choosing the integration limits. For this reason only the general behavior will be compared, and not the α_{max} and $(H/Pd)_{max}$ values.

α_{max} for Pd/Pt(100) nanofilms is very close to the value for bulk Pd. It is about 0.02 H/Pd. $(H/Pd)_{max}$ for Pd films is always smaller than bulk Pd (0.65), but it increases with thickness approaching this upper limit.

The two-phase region for Pd/Pt(100), highlighted by the plateau, starts at the same potential as bulk Pd, at about +0.05 V *vs.* RHE. Nevertheless, the plateau's width decreases as the films thickness is reduced. The two-phase region has almost disappeared for Pd_{5ML}/Pt(100). Moreover, the isotherm in this region is characterized by a slope. Such a behavior is not observed either for bulk Pd or for the nanoparticles. It does not seem that it is just an effect of the size reduction down to the nanometric scale. We believe that this effect is the consequence of the Pt substrate. This conclusion is supported by the fact that the slope in the two-phase region has also been observed for Pd/Pt(111) films[2]. In this case the slope has been attributed to the presence of non-equivalent absorption sites due to the constraints induced by the substrate. This point will be further discussed in the paragraph 4.3.2, where the isotherms obtained for Pd/Pt(111) will be discussed.

4.2 Pd/Pt(111)-H system

The method used for Pd/Pt(100) films is not well suited for isotherm measurements on ultra-thin Pd/Pt(111) films. In the following we will firstly explain

which difficulties must be faced in this system. Then we will propose a new method for isotherms measurement and we will present the obtained results for Pd/Pt(111) films down to 5 ML.

4.2.1 Voltammogram in acidic media

Hydrogen insertion into Pd films was first investigated with cyclic voltammetry, as shown in Figure 4.4.

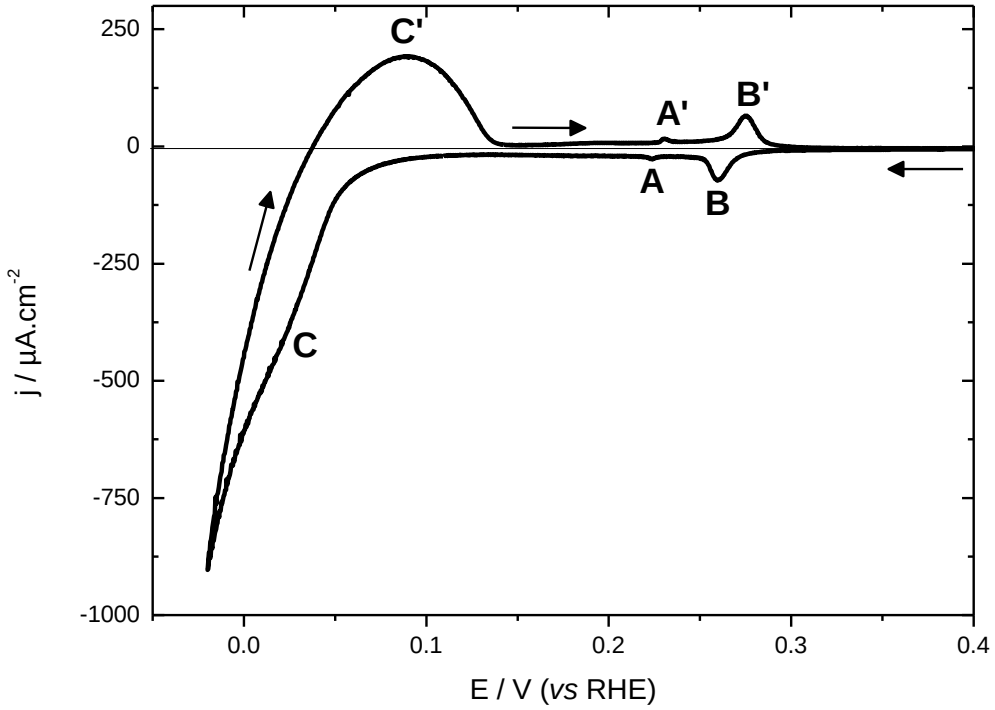

Figure 4.4 : Voltammogram profile of $Pd_{14.2ML}$/Pt(111) in 0.1 M H_2SO_4 at 10 $mV{\cdot}s^{-1}$.

Three pairs of peaks (A; A', B; B' and C; C') are clearly seen on the figure, representing different reactions. The two pairs of peaks at higher potentials have been discussed in Chapter 2 paragraph 2.4.3. They are related to hydrogen/(bi)-sulfate adsorption/desorption reactions occurring on the first Pd monolayer (A; A') and on the following layers (B; B'). The relative evolution of (A; A') and (B; B') is correlated to the thickness of Pd films and to their roughness. Two other peaks are observed at low potential (C; C'). They are highly irreversible. Peaks C and C' are related to hydrogen insertion and desinsertion, respectively. HER-HOR are present in

the same potential region, but contrary to Pd/Pt(100) their contributions are herein not well separated either from hydrogen insertion (C) or from desinsertion (C') peaks. Compared to hydrogen insertion, such contribution is more significant thinner Pd film. We will show that the “classical” method used for Pd/Pt(100) isotherm measurements cannot be used for Pd/Pt(111) for thicknesses lower than about 10 layers.

For this reason another method must be found to determine the hydrogen quantity inserted into Pd/Pt(111) deposits, which allows excluding the HER/HOR contributions.

Reactions at low potentials

A thorough analysis of the reactions occurring in the same potential range than the hydrogen insertion is necessary to understand the various contributions to the recorded electrochemical current.

Table 4.1 presents the reactions occurring at low potential in the hydrogen insertion potential region on the surface of the Pd/Pt(111) films.

$H^+ + e^- \rightleftarrows H_{(ads)}$	**(Equation 4.2)**
$H^+ + e^- \rightleftarrows H_{(ins)}$	**(Equation 4.3)**
$H^+ + e^- \rightleftarrows \frac{1}{2} H_{2(g)}$	**(Equation 4.4)**

Table 4.1 : Reactions in the hydrogen insertion potential region

In the negative scan, peak C corresponds to several reactions at the same time (see Figure 4.4): hydrogen insertion, HER/HOR and, even if in a smaller extent, hydrogen adsorption. The hydrogen adsorption on palladium is represented by (Equation 4.2 forward). Hydrogen insertion into Pd is represented by (Equation 4.3**)** forward). During this reaction, the hydrogen atom enters into the Pd film to form the solid solution or the hydride phase. As discussed in Chapter 3 paragraph 3.2.1, there is a divergence among authors about the mechanism involving direct insertion or an adsorption step preceding insertion. The last reaction (Equation 4.4 forward) is the hydrogen evolution reaction and corresponds to the formation of hydrogen gas. At least for low gas contents, the gas is completely dissolved in the solution.

During the positive scan, the two first reactions are reversed i.e. there is inserted hydrogen release (Equation 4.3) and hydrogen desorption (Equation 4.2

backward). In opposite, HER is still present (Equation 4.4 forward) and coexists with HOR, (Equation 4.4 backward) when approaching 0 V vs. RHE. This last reaction corresponds to the fact that in the positive scan the gaseous hydrogen that did not diffuse far away from the electrode is re-oxidized. This oxidation contributes to the current in peak C'. Thus, it is extremely important to apply a magnetic stirring in order to improve the diffusion of the $H_{2(g)}$ far from the surface, as it was the case for Pd/Pt(100) isotherms evaluation.

Leboin et al.[4] observed that the parallel reactions contributions are no more negligible compared to hydrogen insertion for Pd/Pt(111) films with smaller thickness than about 10 ML, where the $H_{2(g)}$ oxidation contribution causes larger errors in the (H/Pd) ratio calculation.

In the following paragraph, we will present a new method which associates a hanging meniscus rotating disk electrode (HMRDE) with a new calculation technique to measure the quantity of inserted hydrogen in very thin Pd/Pt(111) nanofilms.

4.2.2 Hanging Meniscus Rotating Disk Electrode (HMRDE)

The rotating disk electrode (RDE) has been extensively used in electrochemical studies on HER[5–9]. However, it is difficult to use the conventional RDE in our case. We should make a press-fitting with the electrode material into an insulating holder such as Teflon or another plastic. Such operation can irremediably damage the single crystal. Moreover, it is difficult to retain the protecting water droplet in front of the crystal during assembling, leading to surface contamination. Even more, all the assembling would be done in air and the significant delay needed to complete the procedure would enhance the probability of contamination. Finally, it is difficult to obtain a perfect sealing between the crystal and the plastic holder, resulting in unwanted currents due to the wetting of the lateral side of the crystal.

For these reasons, we decided to use the HMRDE[10–18]. From the point of view of the liquid dynamic, the geometric configuration is not ideal compared to classical RDE, but this is only critical for precise diffusion measurements. In our case, we just want to have a reproducible determination of the HER current and avoid $H_{2(g)}$ accumulation in front of the electrode. Therefore, we just need a constant electrolyte

stream in front of the electrode, which does not require a specific geometry. Figure 4.5 shows the differences between RDE and HMRDE.

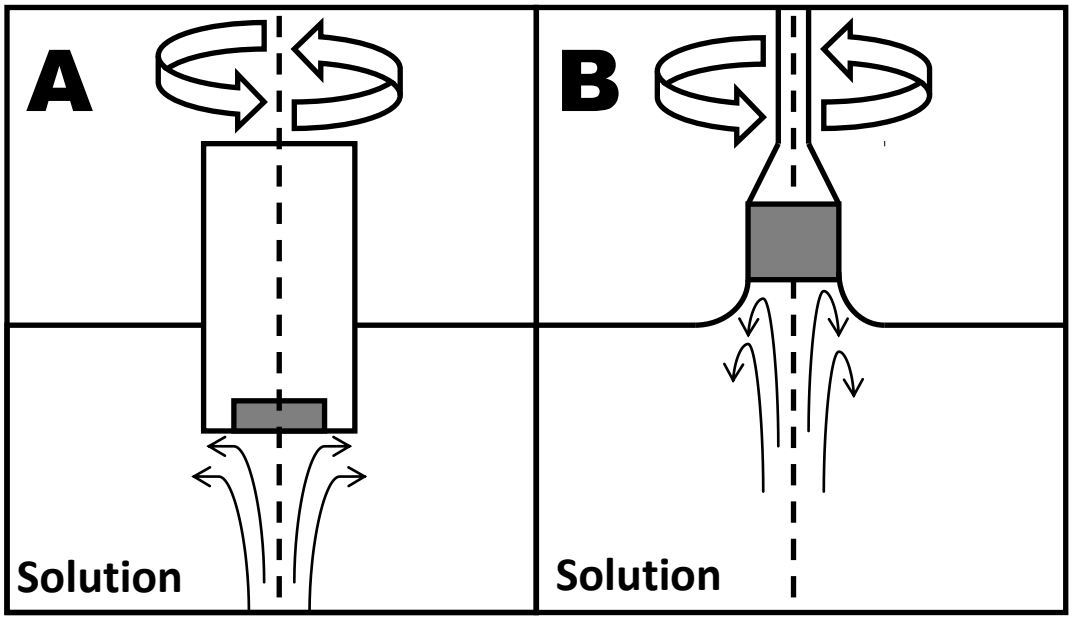

Figure 4.5 : Schematics representative of the rotating disk electrode. (A) classical RDE and (B) HMRDE.

This technique seems to be very simple. It only requires a careful control in the insertion of the electrode in meniscus configuration, avoiding the lateral face wetting. Actually, HMRDE is more complicated compared to classical Hanging Meniscus. We encountered several problems. As the working electrode current is very small, any perturbation is important. When launching the rotation of the electrode, the electrical noise increases significantly. To minimize this effect, it is necessary to check cautiously all the electrical contacts in the RDE. Another problem is due to the current associated with the reduction of oxygen traces. In the rotating system, this problem is increased. It is caused by the not perfect sealing of the RDE, allowing oxygen molecules to enter into the electrochemistry cell. For this reason it is necessary to strongly increase the argon gas flow into the cell to remove the oxygen.

All these experimental problems convinced us to use HMRDE only in the hydrogen insertion/desinsertion measurements and not during Pd deposition.

Single crystal surface preparation and characterization and Pd electro-deposition procedures are the same as those described in Chapter 2 paragraph 2.1. After these steps, the film is rinsed and the crystal is fixed on the RDE. In classical hanging meniscus it is possible to adjust the height of the single crystal above the

solution. It was not possible with HMRDE in our experimental configuration. Thus, the cell was filled with a volume of solution allowing the crystal surface to lie few millimeters above the solution contact. Argon gas stream was maintained for long time (20-25 min) before crystal insertion, but without bubbling in solution. As usual, the potentiostat was switched on before putting the crystal in contact with the solution. Then a soft gas bubbling was turned on inside the solution increasing the level of the solution towards the crystal surface. When the bubbling is turned off, the solution level moves back down and only the hanging meniscus remains. At this step, Pd/Pt(111) was characterized without rotation. Afterwards, the HMRDE rotation was turned on for insertion/desinsertion measurements.

A rotating electrode from Radiometer Analytical BM – ED101 regulated by control station radiometer Copenhagen CTV 101 was used.

Figure 4.6 shows the voltammogram profile obtained using the HMRDE in 0.1 M H_2SO_4 at 10 $mV \cdot s^{-1}$ and 800 rpm.

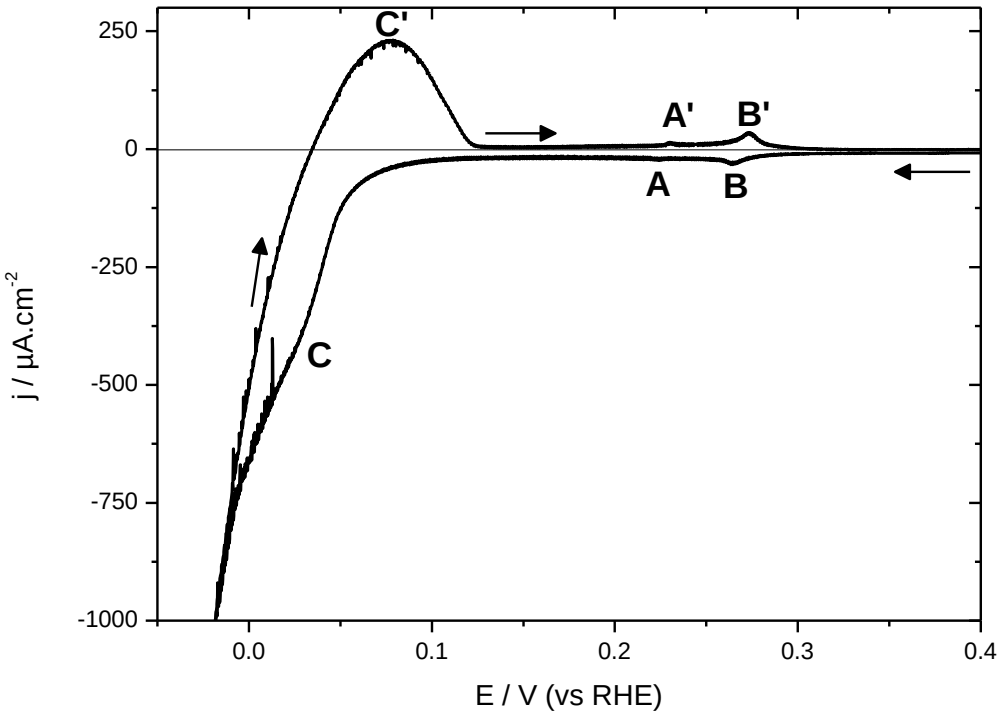

Figure 4.6 : Voltammogram profile of $Pd_{14.2ML}$/Pt(111) using HMRDE in 0.1 M H_2SO_4 at 10 $mV \cdot s^{-1}$.

This voltammogram presents a similar behavior as the one obtained without HMRDE (see Figure 4.4), even if some differences are present: (1) the current is

larger at −0.02 V vs. RHE; (2) the electrical noise is more important, due to the electrode rotation. The voltammogram presented in Figure 4.6 has been obtained after several insertion/desinsertion cycles: the ageing of the film induces a reduction of the peaks A;A' and B;B' intensity compared to Figure 4.4.

4.2.3 Isotherm evaluation method with HMRDE

From the experimental point of view, we followed the same procedure described in paragraph 4.1.2 for the Pd/Pt(100)-H system. The potential was scanned down from +0.15 V vs. RHE (E_{in}) down to the target potential value E_m. It was maintained at E_m until steady state was reached and then it was scanned back to the initial potential value (see Figure 4.2).

By cons, the calculation method used to quantify the hydrogen insertion amount is different when using HMRDE.

The use of a rotating disk electrode firstly allows an immediate removal of $H_{2(g)}$ produced by HER from the front of the electrode avoiding or at least minimizing the HOR contribution. The use of this electrode has the same objective as the use of the magnetic stirring, but with a much better efficiency. So we can minimize the contribution of $H_{2(g)}$ accumulation near the electrode.

With the rotation of the electrode, we also expect a better reproducibility of Faradaic reactions that may be sensitive to diffusion. This means that the current should be the same at a particular potential value, independently from the fact that the potential is scanned positively or negatively. In this case, contributions from Faradaic reactions HER in our case, Table 4.1, (Equation 4.4) should cancel simply subtracting the currents recorded during positive and negative scans. Hence, a simple subtraction of the currents in the positive scan I_p and in the negative scan I_n recorded in the ($E_{in} - E_m$) potential interval would permit to isolate the contribution of adsorption and insertion processes over the HER Faradaic one.

More in details, the integrated charge $\tilde{Q}_H$ of this difference (Equation4.5) would directly give the amount of adsorbed and inserted hydrogen ($H^+ + e^- \rightarrow H_{ads}$ and $H^+ + e^- \rightarrow H_{abs}$):

$$\int_{E_{in}}^{E_m} (I_p - I_n)/2 \, dE = \widetilde{Q}_H(E_m) \qquad \textbf{(Equation4.5)}$$

The relevant aspect for this new method is the cancellation/minimization of the HER/HOR contributions. This allows the removal of a major source of errors in the calculation of the inserted hydrogen amount.

An example of this method is shown in Figure 4.7. It represents the subtraction of the positive scan current to the negative scan one for several lower limits (E_m) on Pd_{14ML}/Pt(111) in 0.1 M H_2SO_4 at 10 mV·s^{-1} and 800 rpm.

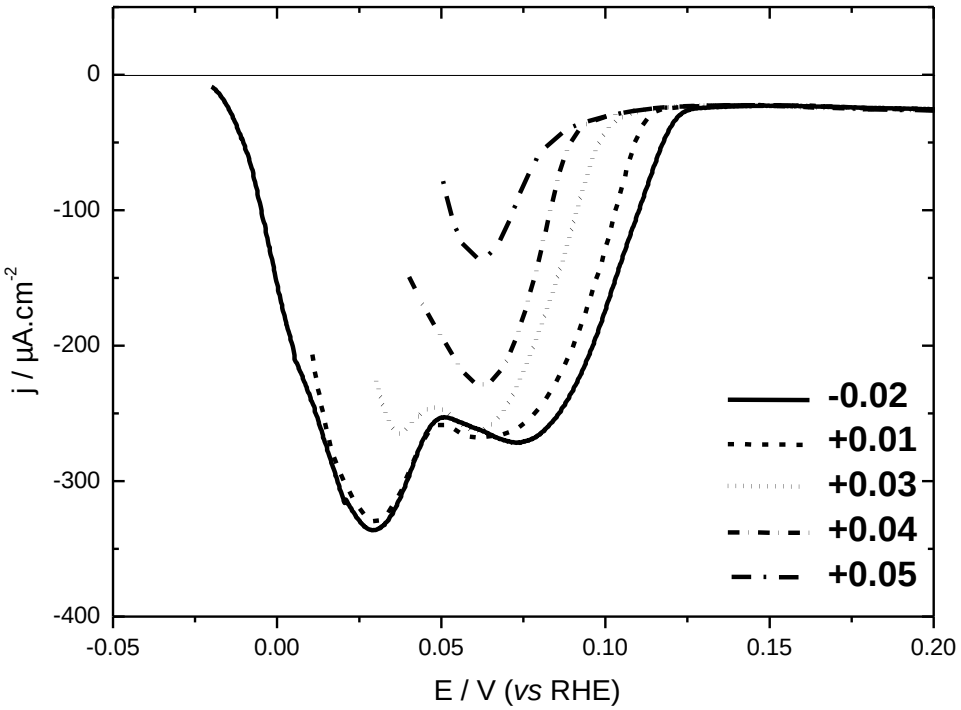

Figure 4.7 : Subtraction between currents recorded in the negative and positive scans for Pd_{14ML}/Pt (111) in 0.1 M H_2SO_4 at 10 mV·s^{-1} and 800 rpm. Each curve represents a different insertion potential E_m.

One can observe the presence of two peaks. This is due to the irreversibility of the hydrogen insertion/deinsertion processes. It is also well shown that the current is nearly back to 0 at –0.02 V vs. RHE, suggesting that HER/HOR contribution is largely eliminated. We will check it more carefully in the following.

Residual HOR contribution

Actually HOR contribution may be incompletely balanced between negative and positive scans due a scan rate too high or to a rotating speed too slow. We have to check it.

Pd_{1ML}/Pt(111) is characterized by a complete Pd layer and it has been shown that no hydrogen insertion is present[19]. For these reasons it can be considered as a system where only HER/HOR and hydrogen adsorption processes are present on Pd. In the HMRDE system the HER is reversible on the Pd surface. The subtraction of negative/positive scan results in the cancellation of HER contribution. Nevertheless, small contributions due to HOR and to hydrogen adsorption may still be present. We made the same measurements presented in the previous paragraph (negative scan, achievement of equilibrium and positive scan) on a Pd_{1ML}/Pt(111) sample, with two rotational speeds, 500 and 800 rpm. Figure 4.8 shows the corresponding integrated charge $2\tilde{Q}_{1ML}(E_m)$ for several target potentials E_m.

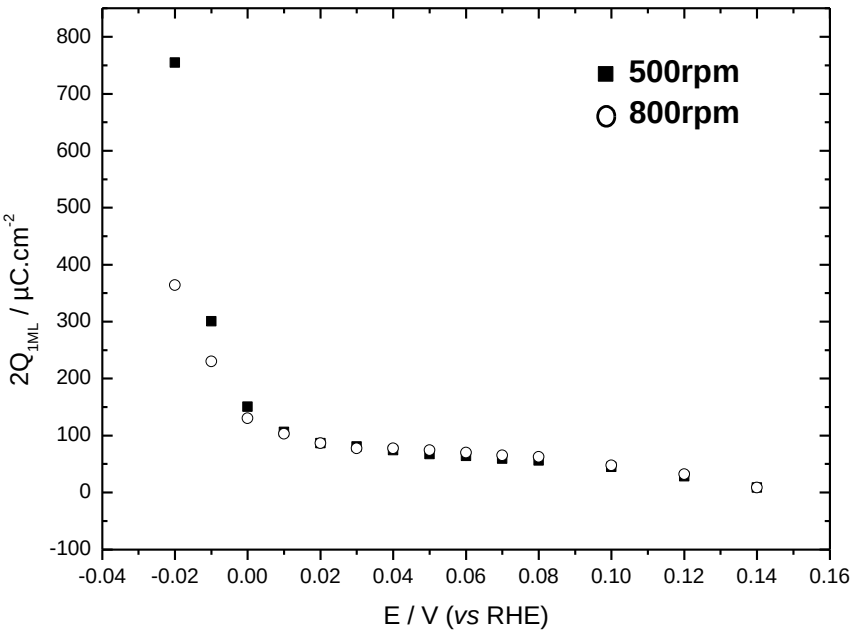

Figure 4.8 : Pd_{1ML}/Pt(111) in 0.1 M H_2SO_4: integrated charge obtained by integration of the difference between the positive scan I_p and the negative scan I_n currents between +0.15 V vs. RHE and E_m.

At positive potentials, the calculated charges are the same with both rotating speeds. In this range, the charge only corresponds to hydrogen adsorption. On the contrary, for potentials equal or lower than 0 V vs. RHE the calculated charges are

more and more sensitive to the rotation speed. We believe that this difference is caused by an incomplete elimination of the H_2 on the on the Pd surface resulting in a non-negligible HOR contribution. The easiest idea to reduce this drawback would be to increase the rotating speed. This is what we observe when changing it from 500 to 800 rpm. At the lowest potential, −0.02 V *vs*. RHE, the charge is decreased from 755 down to 365 $\mu C \cdot cm^{-2}$. As a drawback, the noise strongly increases with the rotation speed of the electrode. This fact makes it difficult to work at speeds greater than 800 rpm. Finally, we chose to work at 800 rpm for the hydrogen insertion study on Pd films. As Figure 4.8 shows, a small, reproducible difference remains between positive and negative currents even at 800 rpm. It is due to the hydrogen adsorption in the 0.15 at −0.02 V vs. RHE interval and to an incomplete elimination of HOR for lower potentials. We have extrapolated the behavior observed on Pd_{1ML}/Pt(111) to thicker Pd films. Indeed, the kinetic of hydrogen evolution is reasonably expected not to depend on the thickness, as shown in Figure 4.9.

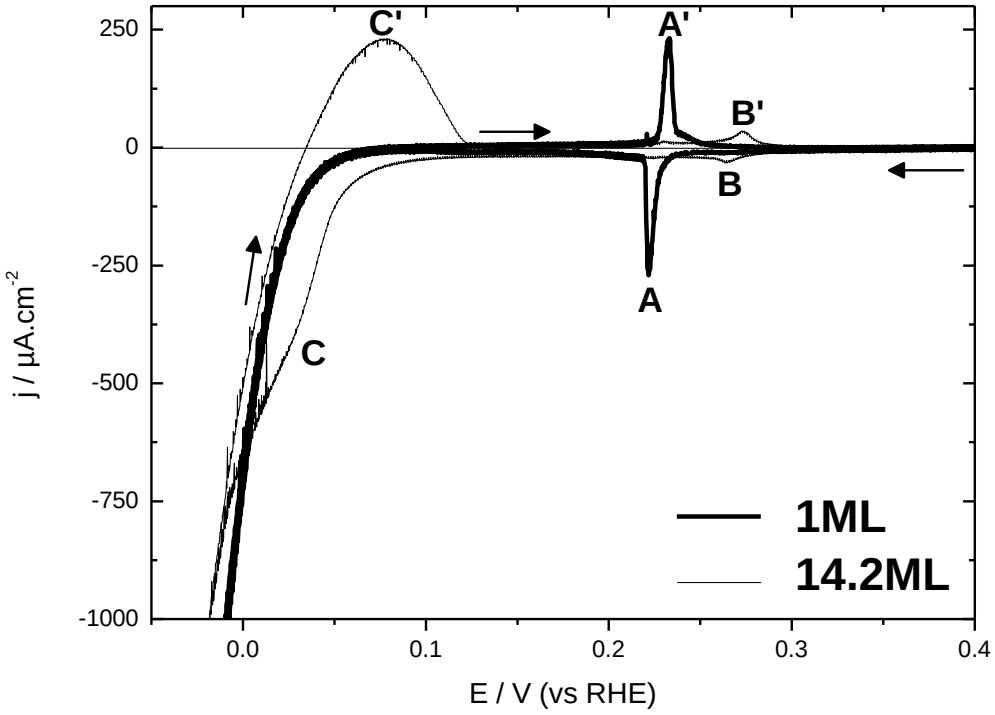

Figure 4.9 : Voltammograms of Pd_{1ML}/Pt(111) and Pd_{14ML}/Pt(111) in 0.1 M H_2SO_4 at 10 mV·s^{-1} and 800 rpm.

Such hypothesis is supported by the fact that hydrogen adsorption is nearly independent of thickness at low potentials. In this way we have considered that the integrated charge $\tilde{Q}_{1ML}(E_m)$ shown in Figure 4.8 represents the H adsorption and HOR contributions to the $\tilde{Q}_H(E_m)$ charge (Equation4.5).

Finally, we used the difference $(\widetilde{\mathrm{Q}}_{\mathrm{H}} - \widetilde{\mathrm{Q}}_{1\mathrm{ML}})$ calculated in the same (E_{in}, E_m) interval to evaluate the amount of inserted hydrogen for the insertion isotherms, allowing not only a better elimination of the HOR contribution but also a complete removal of the hydrogen adsorption contribution.

$$\widetilde{\mathrm{Q}}_{\mathrm{Habs}}(\mathrm{E_m}) = \widetilde{\mathrm{Q}}_{\mathrm{H}}(\mathrm{E_m}) - \widetilde{\mathrm{Q}}_{1\mathrm{ML}}(\mathrm{E_m}) \qquad \textbf{(Equation4.6)}$$

Comparison between classic and HMRDE methods for isotherm measurements

To test the appropriateness of the new proposed method for isotherm measurements, we made a comparison with the results published by Lebouin et al.[2] using the classical procedure as used in our work for Pd/Pt(100).

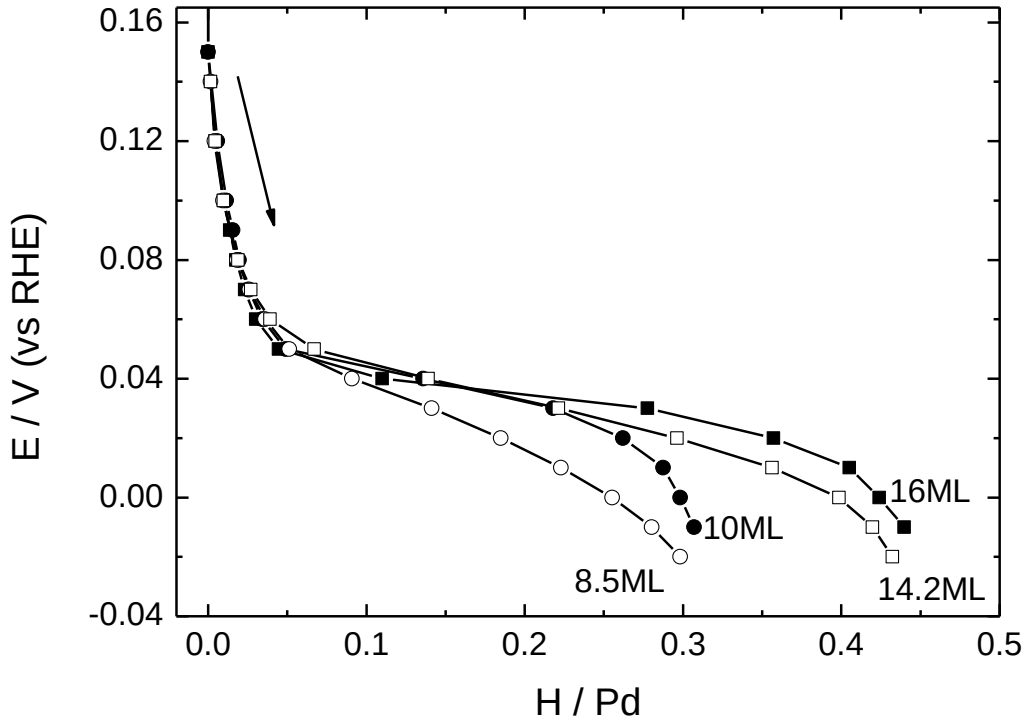

Figure 4.10 : Comparison between the classic[2] (full symbols) and HMRDE (open symbols) methods for the measurements of the absorption branch of H–Pd_{xML}/Pt(111) measured in 0.1 M H_2SO_4. T = 25 °C.

Within the small thickness difference, we can consider that for thicknesses down to about 10 ML both methods are in agreement, even if an overestimation of the inserted hydrogen quantity in the two-phase domain with the classic method is clearly seen.

This comparison allows validating the proposed HMRDE method, opening the possibility to evaluate the hydrogen insertion isotherm for ultra-thin Pd/Pt(111) films.

4.2.4 Experimental isotherms

Following the procedure explained in the previous paragraph, we measured the hydrogen isotherms of very thin Pd/Pt (111) films down to about 4 ML (Figure 4.11). We will see in paragraph 4.1.2 that the isotherm measurements, consisting of repeated cycles of insertion/desinsertion, may induce an ageing of the Pd films during the very first cycles. In order to consider a reproducible response of our samples, we applied the aging process with 10 cycles between 0.62 and –0.02 V vs. RHE at 10 mV s^{-1} previous the isotherm measurements.

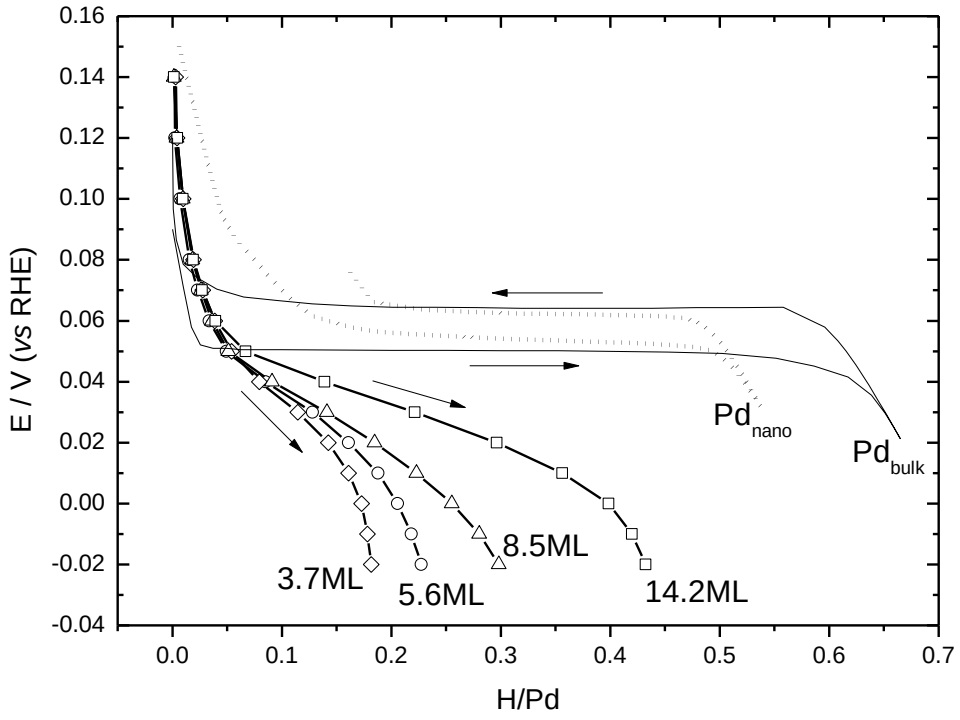

Figure 4.11 : Absorption branches of the electrochemical hydrogen isotherms for H–Pd_{xML}/Pt(111) measured in 0.1 M H_2SO_4; (◊) x = 3.7 ML, (O) x = 5 ML, (Δ) x = 10 ML, (□) x = 16 ML. (—) bulk Pd[2] and (····) nanoparticles (diameter 3.6 nm)[2] are also shown. T =25 °C.

As it was the case for Pd/Pt(100), the hydrogen insertion isotherm for Pd/Pt(111) can be described with 3 regions. At high potential (> 0.05 V vs. RHE), hydrogen insertion rate is low (< 0.05), although slightly higher than the one of α-phase in bulk Pd (α_{max}≈0.03). It corresponds to the solid solution of H in the Pd lattice. The second region is associated to a strong increase of hydrogen solubility, recalling the plateau region of bulk Pd, but with a significant slope. We associate it

with the two phase (α+β) coexistence. Finally, the insertion rate reaches a limit at the lowest potential (-0.02 V vs. RHE). Indeed, boundaries between the different regions (α zone, two-phase domain, β zone) are not well marked in Pd supported films, as suggested by the presence of the slope, and α_{max} and β_{min} parameters do not probably have the same meaning as for bulk Pd. For this reason we will only describe their trend as a function of the various parameters (support, thickness,…), but we will not give any quantitative results.

There is a global decrease of hydrogen insertion rate while reducing the thickness of the Pd/Pt(111) films. $(H/Pd)_{max}$ decreases from 0.43 (14.2 ML) down to 0.18 (3.7 ML). A similar behavior was observed for Pd/Pt(100). In opposite, α_{max} and insertion rates at high potential (> 0.05 V vs. RHE) seem to be very close for all nanofilms and higher than for bulk Pd. The two-phase region seems to start nearly at the same potential (about 0.05 V vs. RHE) for films and bulk Pd.

The Pd/Pt(111)-H isotherms are compared to those for bulk Pd and Pd nanoparticles (3.6 nm). We recall that nanoparticles isotherm has been recorded in gas phase and converted to electrochemical isotherm using the equivalence between $H_{2(g)}$ pressure and the electrode potential (see Chapter 3 paragraph 3.2.2). Again, we observe that the plateau is not horizontal only for the supported Pd films. So, like for Pd/Pt(100), the slope seems to originate from the substrate and not from the nanometric size.

4.3 Isotherms interpretation

4.3.1 Comparison of Pd/Pt(111) and Pd/Pt(100) isotherms

It is interesting to consider the effect of the substrate orientation by comparing the hydrogen insertion isotherms for Pd/Pt(111) and for Pd/Pt(100). We recall that Pd/Pt(100)-H system has been studied with the classical methods and that a small contribution of HER and H adsorption may hence contribute to the isotherm in particular for the thinnest film. For this reason we will discuss the behavior of α_{max} and of the slope in the two-phase region only for the thicker deposits.

Figure 4.12 shows the comparison for several thicknesses.

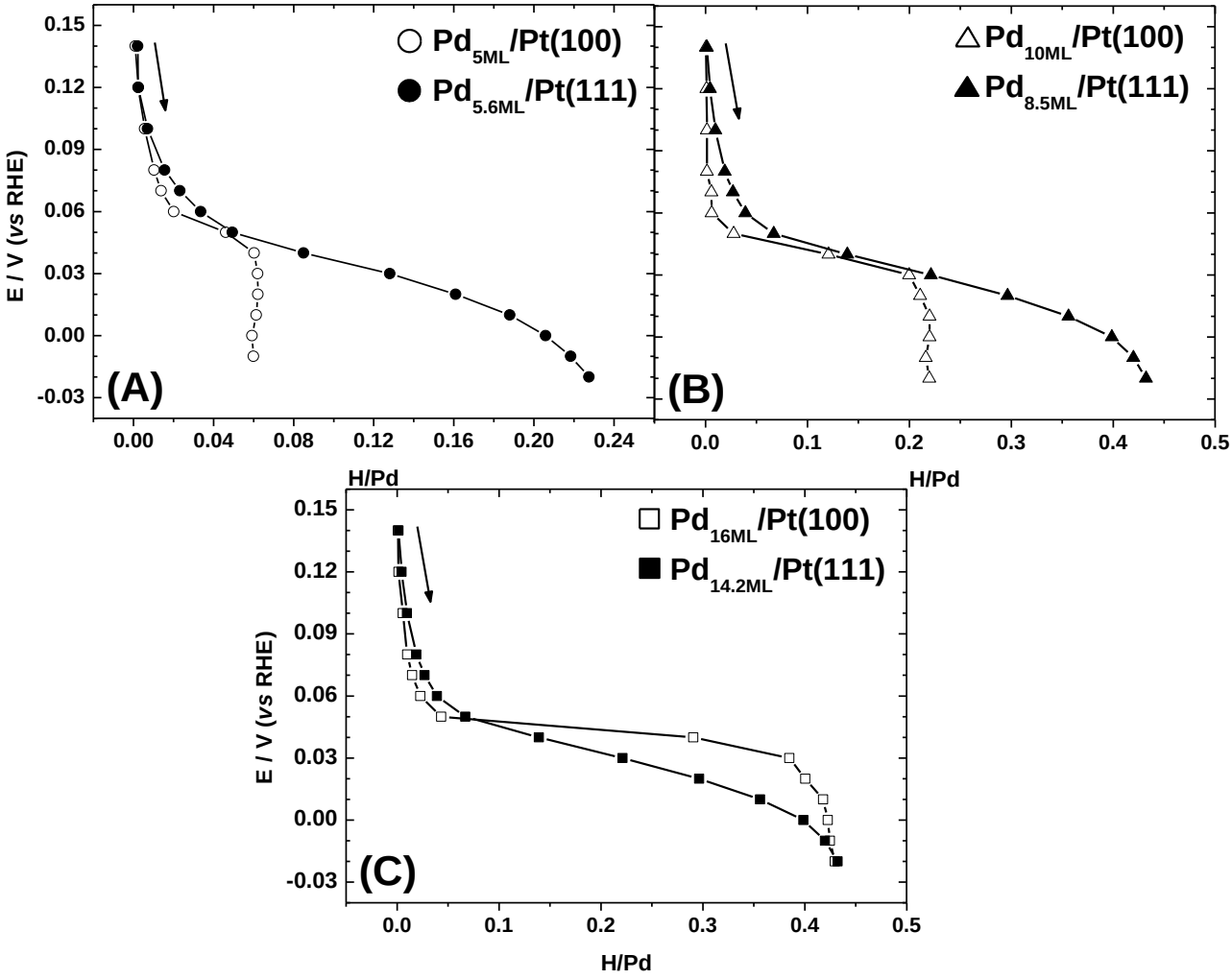

Figure 4.12 : Comparison of hydrogen insertion isotherms for Pd/Pt(111° and Pd/Pt(100) films; thinner (A), intermediary (B) and largest (C) thicknesses.

The maximum hydrogen insertion rate $(H/Pd)_{max}$ values are very similar in correspondence of the highest thicknesses, approaching in both systems the bulk Pd value. The separation in 3 regions (low insertion rate, plateau and high insertion rate) is much more evident on Pt(100), compared to Pt(111), due to a larger slope in this last system.

When reducing the thickness, $(H/Pd)_{max}$ decreases much faster on Pt(100) compared to Pt(111). For instance, its value for Pd_{5ML}/Pt(100) is only about one quarter of that for $Pd_{5.6ML}$/Pt(111).

The potential range covered by the two-phase plateau is smaller on Pt(100), compared to Pt(111). For Pd/Pt(100), the plateau starts at 0.06 V vs. RHE and ends at about 0.04 V vs. RHE. For Pd/Pt(111), as far as we can precisely define the limits, it also starts at about 0.06 V vs. RHE, but it finishes at around 0 V vs. RHE. Hence

the potential range of plateau is three times larger on Pd/Pt(111) compared Pd/Pt(100).

4.3.2 Pd/Pt(111)-H isotherms interpretation

In order to explain the behavior versus hydrogen insertion of Pd nanofilms on Pt(111), physical characterizations of the Pd deposit have been performed in LEPMI by the ESME team in the past years. Surface X-ray diffraction measurements have been done *in situ* in electrochemical environment before and after hydrogen insertion into Pd/Pt(111) nanofilms from 2 ML[19] up to about 20 ML[20].

The following explanations are mostly extracted from a submitted paper that combines the above mentioned X-ray measurements with our new HMRDE isotherm determination.

Figure 4.13 shows a scheme of the thinnest film Pd_{2ML}/Pt(111) structure derived from the best fit results.

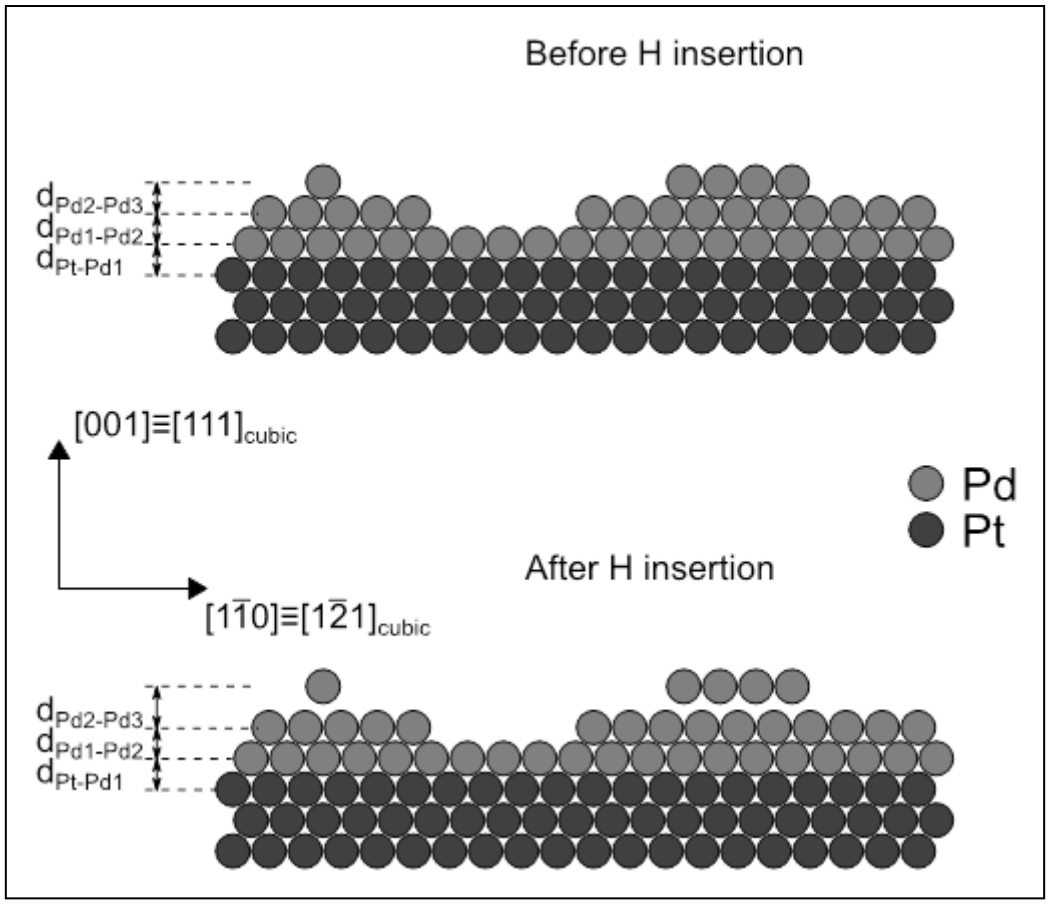

Figure 4.13 : Schematic representation of Pd_{2ML}/Pt(111) structure before and after hydrogen insertion.

Even if three layers are necessary to describe the experimental data, the deposit is quite flat, with a poorly occupied third layer, $\tau_3 \approx 0.22$. The smaller interplanar distance between the palladium layers, 2.22 ± 0.02 Å, results in the preservation of the unit cell volume in the pseudomorphic growth. The most interesting result obtained concerns the structure evolution of the Pd film after hydrogen insertion. First the pseudomorphic character is maintained, as shown by the fact that the data are fitted using the same structural model as before insertion. Moreover, no significant evolution is observed of either the distance at the Pt-Pd_1 interface, or the distance between Pd_1 and Pd_2 layers. Yet, the formation of hydride (β-phase) is accompanied by an increase of the lattice parameter and this expansion is related to the PdH_x stoichiometry[21]. Hence, the absence of interlayer expansion allows concluding that, contrarily to what expected, no hydride is formed in the two atomic Pd layers closest to the Pt interface. However, we must underline that our measurements cannot exclude the presence of interstitial hydrogen with lower concentration (α-phase), inducing no measurable interplanar distance expansion.

These results show that the geometric and ligand effects induced by the substrate play a major role in the absence of hydride formation in the two pseudomorphic layers.

Compared to bulk Pd, even if the volume of the unit cell in the Pd film is roughly preserved, the cell is distorted. There is an increase of the in-plane parameters by 0.86 % and a decrease in the out-of-plane direction by about 1.2 %. This substrate induced strains persist after hydrogen insertion. They surely play an important role in explaining the resistance to hydriding of the Pd_{2ML}/Pt(111) film. It has been already pointed out that the constraints induced by the substrate must be considered for the thermodynamic treatment of hydrogen insertion in thin films[22–24]. Induced variations in the surface electronic structure for pseudomorphic metallic overlayers must be considered as well, as it has been underlined with density functional calculations[24,25].

Hydride formation is observed between the second and the third Pd layers, with the increase of the interplanar distance ($d_{Pd2\text{-}Pd3}$ = 2.305 ± 0.02 Å). This expansion corresponds to a variation of 2.6 ± 0.9 % when calculated with respect to bulk Pd lattice constant. Due to the significant error bar, we cannot state any clear tendency compared to $PdH_{0.6}$.

Thicker films, Pd_{22ML}/Pt(111) and Pd_{14ML}/Pt(111), were studied to better correlate hydrogen insertion to the induced structural modifications. This allowed revealing the presence of two regions in the hydride Pd film, as the schematic representation of the film structure in Figure 4.14.

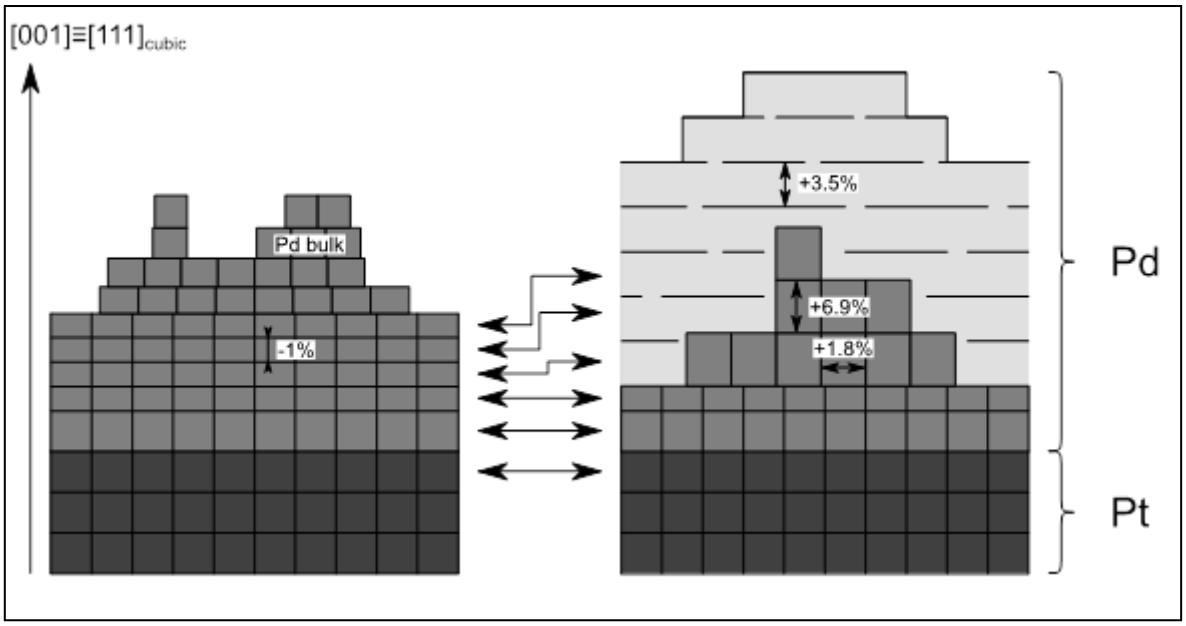

Figure 4.14 : Out-of-plane schematic representation of the Pd film structure before (left) and after (right) hydrogen insertion. The relaxed region in the hydride Pd film is indicated by the lightest grey zone. The percentages represent unit cells expansion in the nanofilm compared to bulk Pd.

Before hydrogen insertion, the film is in registry with the substrate with pseudomorphic growth. Both fits, Pd_{22ML}/Pt(111) and Pd_{14ML}/Pt(111), give a quite high number of fully occupied layers (17 and 10, respectively). The occupancy value then rapidly decreases in both deposits, giving an equivalent thickness of 22 and 14 layers, respectively. The comparison between the quantitative analysis of these two Pd films shows that, independently of the thickness of the film, the Pd deposits are quite flat.

The interlayer spacing before hydrogen insertion $d_{Pt\text{-}Pd1}$ distance is equal to 2.25 Å and d_{111} value of the following about ten Pd layers is equal to 2.218 Å, in agreement with the results obtained for Pd_{2ML}/Pt(111). This distance is compressed with respect to the correspondent bulk value, compensating for the in plane strain induced by the coherent epitaxy on the Pt substrate. Above this thickness, a gradient of the interlayer distances is obtained, and d_{111} reaches the asymptotic value close to the Pd bulk one (2.245 Å). We believe that this corresponds to a progressive in plane relaxation.

After hydrogen insertion, the hydride formation is clearly seen in diffraction signals. Shortly, 3 regions are observed (Figure 4.14). No interlayer expansion is seen between the 1st and the 2nd layer. The following about 5 layers as equivalent thickness, even if no more pseudomorphic, are still coherent with the substrate. The

in-plane expansion versus the substrate is about 1 %. The out-of-plane expansion is about 6.9 % compared to bulk Pd. The third region composed by the outermost layers is not correlated at all with the substrate. The out-of-plane expansion, around 3.5 %, corresponds to the hydride bulk Pd, $PdH_{0.6}$.

As discussed in previous paragraph 4.1.3, the maximum hydrogen insertion rate $(H/Pd)_{max}$ dramatically diminishes for Pd nanofilms on Pt(111) compared to bulk palladium. Moreover, it strongly depends on the film thickness: the thinner the film, the smaller the hydrogen solubility.

A first attempt to explain this result takes into account for the absence of hydride formation in the two first Pd layers, as shown by *in situ* SXRD measurements. Such resistance to hydriding surely diminishes the total hydrogen solubility and this effect is all the more important as the thickness diminishes. Even if H insertion in α-phase cannot be excluded, its amount would be negligible due to the small α_{max} value (α_{max} = 0.03 in bulk Pd). Nevertheless, the absence of hydriding in the two first Pd layers is not enough to explain the measured $(H/Pd)_{max}$ values. Considering two "dead" layers at the interface of $Pd_{8.5ML}$/Pt(111) ($Pd_{14.2ML}$/Pt(111)) and an insertion rate for the remaining 6.5 (12.2) layers equal to the bulk one, $(H/Pd)_{max}$=0.67, we would expect to measure a total insertion ratio of 0.51 (0.58), still far from the observed values. A further mechanism must be invoked.

X-ray measurements showed that a region close to the interface beyond the two first monolayers is still strained and maintains some kind of registry with the substrate up to about 5 ML as equivalent thickness. We believe that the constraints of this region affects (decreases) its hydrogen solubility. In this context we propose a structural model composed by 3 zones. The two first pseudomorphic layers are characterised by a negligible insertion rate. A reduced hydrogen insertion rate $(H/Pd)_{constraint}$ is attributed to the following still constraint zone extending up to about 5 equivalent layers. The outermost layers, characterized by a hydride bulk like interlayer distance, are supposed to have the bulk $(H/Pd)_{max}$ solubility. A confirmation of this "bulk Pd like" behaviour comes from the electrochemical isotherms. They show that the potential value corresponding to the beginning of β-phase formation (+0.05 V *vs.* RHE) is about the same as for bulk Pd (Figure 4.11).

Comparing with the electrochemical isotherm hydrogen maximum solubility values, it is possible to evaluate the hydrogen insertion rate value $(H/Pd)_{constraint}$ in the constraint part of the deposit. In the calculations we took into account that for the two

thinnest films, 3.6 and 5.7 ML, the second layer is not complete, as it is shown by electrochemical characterisation[2]. We did an overall evaluation of $(H/Pd)_{max}$ values considering four equations, one for each thickness, with no hydriding in the first and second Pd layers, a reduced $(H/Pd)_{constraint}$ hydrogen solubility in the constraint region up to 5 layers and a $(H/Pd)_{relaxed}$ solubility in the outermost part of the film. We considered an occupation rate τ_2 of the second layer equal to 0.8 for $Pd_{3.6\ ML}$/Pt(111) and equal to 0.85 for $Pd_{5.7ML}$/Pt(111) ($\tau_2 = 0.73$ for Pd_{2ML}/Pt(111))[19]. τ_2 has been set equal to 1 for the higher thicknesses. As a result, we obtain $(H/Pd)_{relaxed}$=0.66, value very close to bulk Pd one (0.67), confirming the fact that the relaxed region behaves like bulk Pd. For the constrained part, the hydrogen insertion rate is much lower, $(H/Pd)_{constraint} = 0.32 \pm 0.04$. Of course our model is quite schematic, but nevertheless it succeeds in accounting even quantitatively for the experimental behaviour of the maximum hydrogen insertion rate as a function of the thickness.

Such structural model can be used to explain another characteristic of the electrochemical isotherms on Pd/Pt(111) films, i.e. the presence of a slope in the two–phase domain (Figure 4.11). This slope is not only absent for Pd bulk, but also for unsupported Pt nanoparticles, confirming that such an effect is induced by the substrate. Indeed, the origin of this phenomenon can be at least partly understood with the help of the structural characterisation given by SXRD. Not only there is a front line separating two differently ordered regions, which is moving and shape evolving as a function of the hydrogen insertion rate, but the relaxed outermost domain incorporates inhomogeneities, defects and uncorrelated domains. These phenomena induce the presence of many different absorption sites for hydrogen, contributing to the explanation for the presence of a slope in the two-phase plateau in the case of Pd/Pt(111) nanofilms.

As a conclusion, the electrochemical isotherm measurements are in agreement with the presence of 3 regions in the hydride Pd film, as observed by SXRD. Each region is characterised by a different order and by a different hydrogen insertion rate. In the constraint region near the Pt–Pd interface, no hydride is present in the two first pseudomorphic layers and the following constraint layers are marked by a small hydrogen insertion rate, corresponding to about slightly less than one half of the hydride bulk value. The third zone is the outermost relaxed part of the Pd deposit, which has a bulk Pd like behaviour.

4.3.3 Pd/Pt(100)-H isotherms interpretation

In the absence of detailed physical characterization of the hydrided Pd films, it is difficult to propose any model for the shape and the behavior of the isotherms. Nevertheless, we can give some clues thanks to the comparison with Pd/Pt(111).

The slope in the two-phase region in Pd/Pt(111) has been attributed to the presence of non-equivalent absorption sites due to the substrate induced constraints. For this system *in situ* SXRD measurements have shown that the substrate influence extends up to about 10 monolayers. The less pronounced slope in the two-phase region for the thicker Pd/Pt(100) film should hence be related to the presence of mainly equivalent absorption sites. Indeed, the surface characterizations we made on Pd/Pt(100) deposits (*ex situ* AFM images, electrochemical characterization) have shown that the influence of the support is very strong up to 2 ML, while it recedes for higher thicknesses. Hence, it looks like Pd/Pt(100) films beyond about 15 ML are not characterized by largely differently constraints regions, and hence by non-equivalent hydrogen insertion sites, concerning the hydrogen insertion rate.

Nevertheless it seems that at about 15 ML the Pd films have about the same total amount of inserted hydrogen, independently from the substrate. The lower $(H/Pd)_{max}$ value compared to bulk Pd should therefore be mainly due to the nanometric size of the deposits and not the induced constraints.

More difficult is the comprehension of the stronger $(H/Pd)_{max}$ decrease with thickness for Pd/Pt(100) than for Pd/Pt(111). Such behavior suggests that the region resistant to hydriding should be larger compared to Pd/Pt(111), maybe characterized by the absence of β phase or at least by a very small insertion rate, even lower than for the constraint region in Pd/Pt(111). We also remark that the isotherm behavior of Pd_{5ML}/Pt(100) reminds the result found by Pundt et al.[26] for nanoparticles and the isotherm behavior of bulk Pd beyond the critical temperature, where only one phase is present.

Such intriguing results need further investigations. In particular *in situ* SXRD measurements are needed to better understand such intriguing behavior*.

* *In situ* SXRD measurements on Pd/Pt(100) films have been recently made at the ESRF. The data analysis will be made in the next months.

4.4 Aging process of the Pd/Pt(111) nano-films

As discussed in chapter 3, bulk Pd is subject to strong degradations through repeated hydrogen insertion/desinsertion cycles. Such process is called ageing. In the aim of knowing if such a phenomenon occurs in Pd nanofilms as well, we made specific experiments on Pd/Pt(111) nanofilms.

We applied 10 potential cycles down to -0.02 V *vs*. RHE on a freshly prepared and characterized sample. Each cycle should correspond to a full insertion/desinsertion process, but we must underline that we did not wait to obtain a steady state at the lowest potential. Following figure presents the result obtained for $Pd_{8.5ML}$/Pt(111):

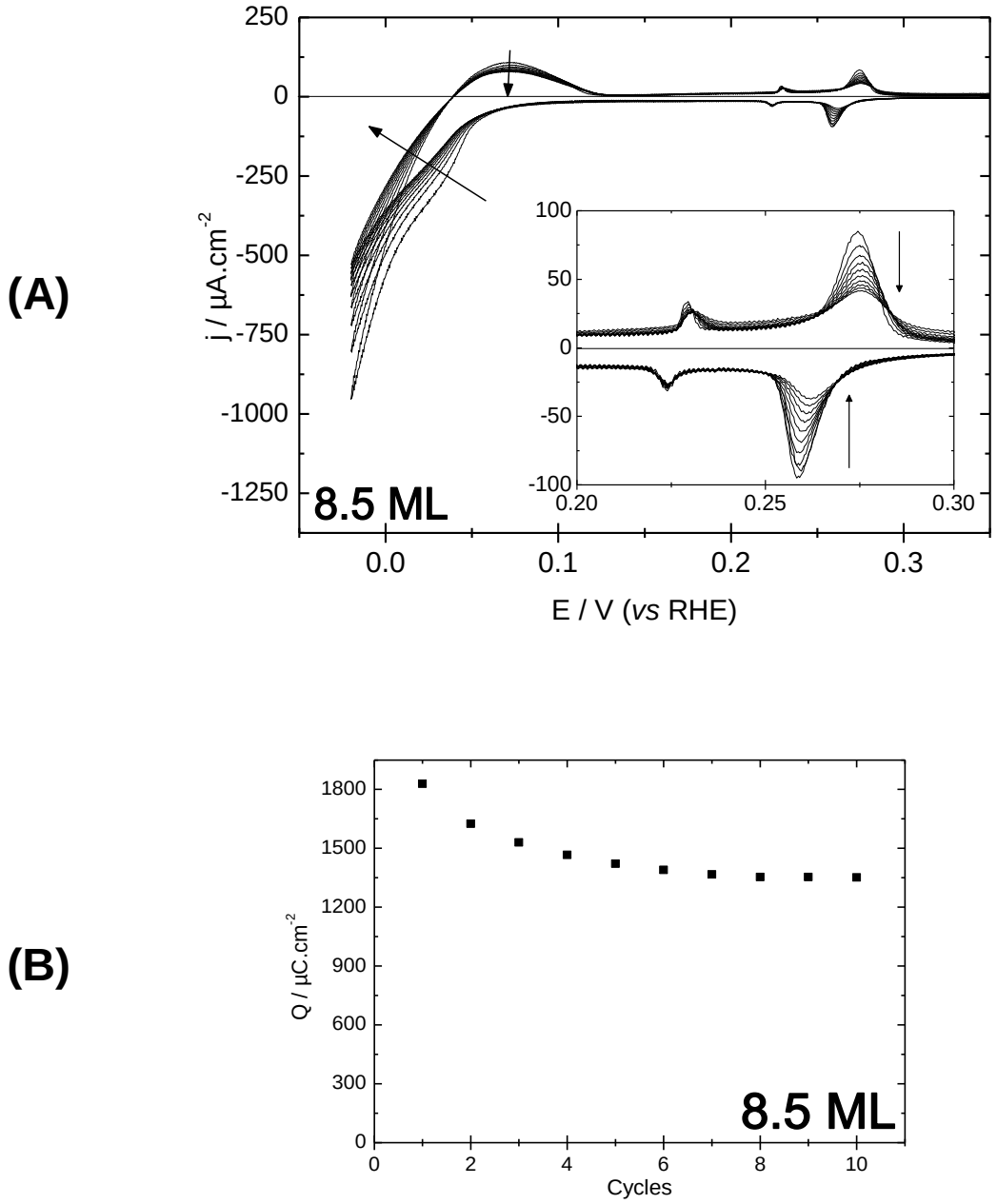

Figure 4.15: Ageing process: (A) 10 first cycles for hydrogen insertion/desinsertion on $Pd_{8.5ML}$/Pt(111) in 0.1 M H_2SO_4 at 10 $mV \cdot s^{-1}$ and 800 rpm. (B) Total hydrogen charge calculated for each complete cycle (0.15, –0.02 V *vs.* RHE).

Not only ageing process modifies the surface morphology of the Pd films, as shown by the decrease in the anions adsorption peaks at higher potentials, but also the current value at lower potential undergoes important changes. The total integrated charge Q, even if it does not represent the total amount of inserted hydrogen, testifies such structural evolution, reaching a limit value after about 5 cycles.

We repeated such experiments for several Pd thicknesses. We must underline that we observed a lack of reproducibility in the experiments made on samples with the same thickness. Nevertheless, the ageing exists for all thicknesses, as shown in Figure 4.16.

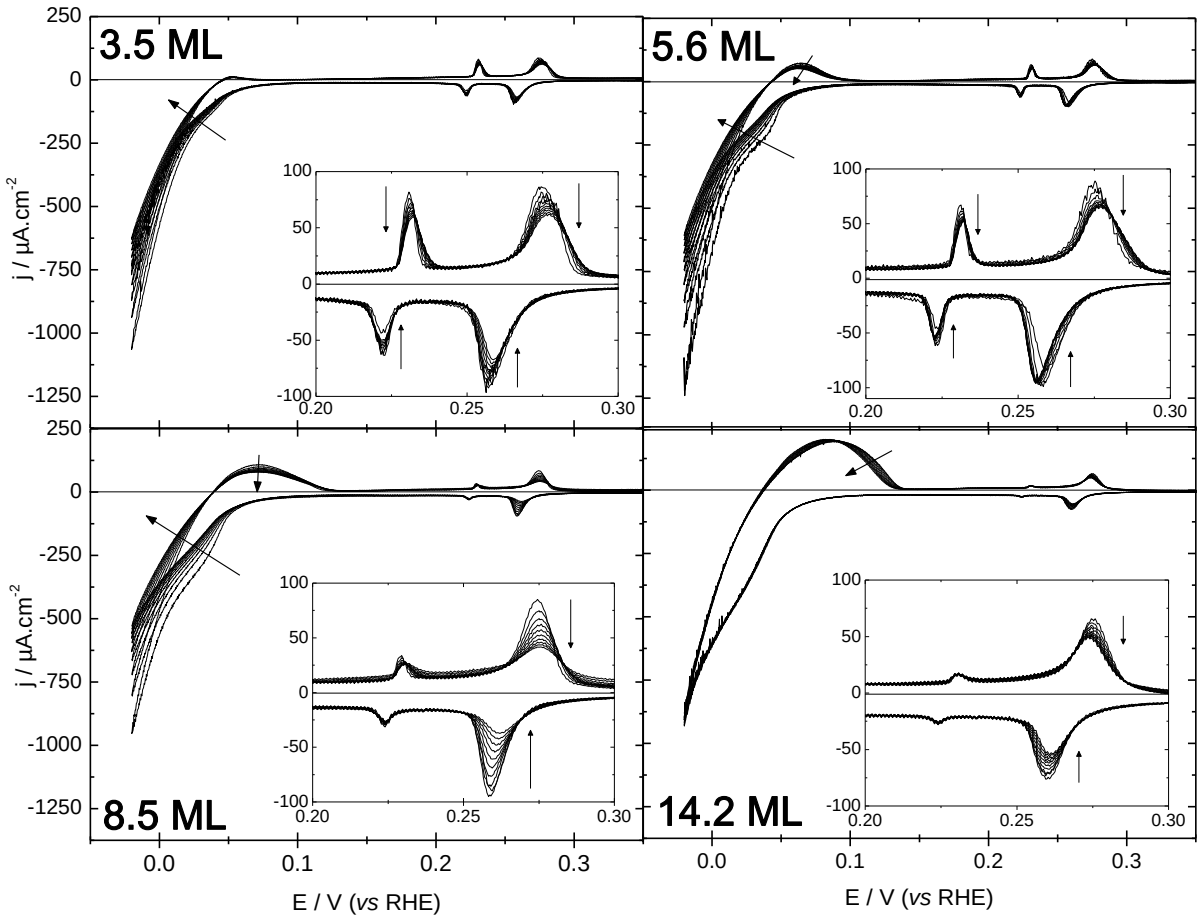

Figure 4.16 : Ageing process: 10 first cycles for hydrogen insertion/desinsertion on Pd_{xML}/Pt(111) in 0.1 M H_2SO_4 at 10 $mV \cdot s^{-1}$ and 800 rpm. Insets: enlargement of high potential region.

Our findings show that hydrogen insertion/desinsertion process modifies the Pd nanofilms structure, even if a more detailed study must be performed in order to quantify the effect of such ageing on the total amount of inserted hydrogen.

4.5 Conclusion

We made the first measurements of hydrogen insertion isotherms in Pd/Pt(100) thin films. The total amount of inserted hydrogen, $(H/Pd)_{max}$, strongly

decreases with thickness reduction, hardly overcoming for Pd_{5ML}/Pt(100) the α_{max} insertion rate value of bulk Pd. The two-phase plateau region of the isotherm not only reduces with thickness decrease, but it also presents a slope. Such a slope is not observed with unsupported Pd nanoparticles with equivalent size, suggesting that the slope is due to a substrate effect.

For Pd/Pt(111), hydrogen insertion and desinsertion are not as well separated from hydrogen evolution reaction as for Pd/Pt(100). For this reason we have developed a new experimental setup using hanging meniscus rotating disk electrode. Using this experimental device in conjunction with a new calculation method, we were able to record hydrogen insertion isotherm on Pd/Pt(111) with thicknesses down to 3.7 ML.

Similarly to Pd/Pt(100), (H/Pd)max decreases with Pd/Pt(111) film thickness diminishing, but its value is larger for the same thickness. The plateau region shows a slope, but it extends over a larger potential interval (60 mV versus 20 mV for Pd/Pt(100)). We could link the isotherm behavior observed as a function of the thickness to the structure at the atomic level of the hydride Pd film measured with *in situ* Surface X-ray diffraction measurements. The main role of substrate induced constraints on the Pd deposit has been revealed.

The presence of an ageing process during the first hydrogen insertion/desinsertion cycles has been revealed for Pd/Pt(111) ultra-thin films.

4.6 References

(1) Kibler, L. A. *International Society of Electrochemistry* **2003**, 1–55.

(2) Lebouin, C.; Soldo-Olivier, Y.; Sibert, E.; Millet, P.; Maret, M.; Faure, R. *Journal of Electroanalytical Chemistry* **2009**, *626*, 59–65.

(3) Birry, L.; Lasia, A. *Electrochimica Acta* **2006**, *51*, 3356–3364.

(4) Lebouin, C. Films d'épaisseurs nanométriques de Pd sur Pt(111): élaboration, caractérisations et étude de l'électro-insertion de l'hydrogène, Grenoble University, 2008.

(5) Sheng, W.; Gasteiger, H. A.; Shao-Horn, Y. *Journal of The Electrochemical Society* **2010**, *157*, B1529.

(6) Conway, B. E.; Tilak, B. V. *Electrochimica Acta* **2002**, *47*, 3571–3594.

(7) Freitas, K. S.; Lopes, P. P.; Ticianelli, E. A. *Electrochimica Acta* **2010**, *56*, 418–426.

(8) Montero, M. A.; Gennero de Chialvo, M. R.; Chialvo, A. C. *International Journal of Hydrogen Energy* **2011**, *36*, 3811–3816.

(9) Santos, L. G. R. A.; Freitas, K. S.; Ticianelli, E. A. *Journal of Solid State Electrochemistry* **2007**, *11*, 1541–1548.

(10) Cahan, B. D.; Villullas, H. M. *Journal of Electroanalytical Chemistry and Interfacial Electrochemistry* **1991**, *307*, 263–268.

(11) Cahan, B. D.; Villullas, H. M.; Yeager, E. B. *Journal of Electroanalytical Chemistry and Interfacial Electrochemistry* **1991**, *306*, 213–238.

(12) Pérez, J. M.; Gonzalez, E. R.; Villullas, H. M. *The Journal of Physical Chemistry B* **1998**, *102*, 10931–10935.

(13) Pérez, J. M.; Villullas, H. M.; Gonzalez, E. R. *Química Nova* **1997**, *20*, 555–559.

(14) Pérez, J. M.; Villullas, H. M.; Gonzalez, E. R. *Journal of Electroanalytical Chemistry* **1997**, *435*, 179–187.

(15) Villullas, H. M.; Brunetti, V.; Teijelo, M. L. *Journal of Electroanalytical Chemistry* **1997**, *437*, 255–258.

(16) Villullas, H. M.; Teijelo, M. L. *Journal of Electroanalytical Chemistry* **1996**, *418*, 159–165.

(17) Villullas, H. M.; Teijelo, M. L. *Journal of Electroanalytical Chemistry* **1995**, *385*, 39–44.

(18) Villullas, H. M.; Teijelo, M. L. *Journal of Electroanalytical Chemistry* **1995**, *384*, 25–30.

(19) Lebouin, C.; Soldo-Olivier, Y.; Sibert, E.; De Santis, M.; Maillard, F.; Faure, R. *Langmuir* **2009**, *25*, 4251–5.

(20) Soldo-Olivier, Y.; Lafouresse, M. C.; De Santis, M.; Lebouin, C.; De Boissieu, M.; Sibert, E. *The Journal of Physical Chemistry C* **2011**, *115*, 12041–12047.

(21) Rose, A.; Maniguet, S.; Mathew, R. J.; Slater, C.; Yao, J.; Russell, A. E. *Physical Chemistry Chemical Physics* **2003**, *5*, 3220.

(22) Suleiman, M.; Faupel, J.; Borchers, C.; Krebs, H.-U.; Kirchheim, R.; Pundt, A. *Journal of Alloys and Compounds* **2005**, *404-406*, 523–528.

(23) Wagner, S.; Uchida, H.; Burlaka, V.; Vlach, M.; Vlcek, M.; Lukac, F.; Cizek, J.; Baehtz, C.; Bell, A.; Pundt, A. *Scripta Materialia* **2011**, *64*, 978–981.

(24) Ruban, A.; Hammer, B.; Stoltze, P.; Skriver, H. .; Nørskov, J. . *Journal of Molecular Catalysis A: Chemical* **1997**, *115*, 421–429.

(25) Kitchin, J.; Nørskov, J.; Barteau, M.; Chen, J. *Physical Review Letters* **2004**, *93*, 156801.

(26) Pundt, A.; Suleiman, M.; Bähtz, C.; Reetz, M. T.; Kirchheim, R.; Jisrawi, N. M. *Materials Science and Engineering: B* **2004**, *108*, 19–23.

5 General conclusion

Hydrogen storage represents a technological lock for the use at large scale of hydrogen as energy vector. In the last years metallic hydrides have been largely studied for their properties as hydrogen reservoir.

Palladium is a very interesting model system for the study of hydrogen insertion/desinsertion. Several studies are present in the literature on hydrogen insertion into bulk palladium and into Pd nanoparticles. In opposite, very little work has been done on palladium supported nanofilms. Original properties are expected not only due to the nanometric size, but also to the influence of the substrate. The use of single crystal as well-defined substrates may provide Pd nanofilms with low defect content, more suitable for model studies.

The present work deals with the elaboration and characterization of Pd films on Pt(111) and Pt(100), and with the electro-insertion of hydrogen.

Pd/Pt(100) nanofilms preparation was done by electrochemical deposition in acidic aqueous media. After single crystal surface preparation and quality check, it is put in contact with the deposition solution at high potential. Then, the potential is slowly (0.1 $mV \cdot s^{-1}$) scanned down, allowing the detection of a specific phenomenon called UPD (Under Potential Deposition) of the first atomic layer of Pd. Such UPD effect was theoretically predicted, but it was never experimentally proved for Pt(100). The crystallographic orientation of the substrate has a large effect on Pd growth. Firstly, the UPD of the first layer happens at higher potential for the more open Pt(100) surface, close to the potential region of surface oxide formation. We had to increase the amount of Cl^- in deposition solution in order to get enough potential separation between UPD and oxide formation. Second, we highlighted the UPD character of the second Pd/Pt(100) atomic layer. Such phenomenon of two UPD layers is quite uncommon and is not observed for Pt(111).

Pd/Pt(100) nanofilms have been characterized in sulphuric acid solution. We could confirm the assignment of two different peaks in the voltammograms to the anion adsorption on the first Pd layer and on Pd atoms of the second and following layers. This electrochemical characterisation has confirmed the layer-by-layer growth of Pd/Pt(100) deposit up to two layers, as expected for UPD. It also suggests the presence of a 3D growth beyond the two first complete layers.

In collaboration with SIMAP, we recorded *ex situ* AFM images on several samples with different thickness. The Pd_{2ML}/Pt(100) surface is quite flat. A 3D growth with a significant increase of the roughness is observed for Pd_{4ML}/Pt(100). Roughness only slightly increases for the higher thickness Pd_{14ML}/Pt(100), but the surface is uniformly composed by square based pyramids following the (100) orientation of the substrate. The description of the surface morphology as obtained by AFM is in complete agreement with the electrochemical characterizations.

We made measurements of hydrogen insertion isotherms for the two differently oriented systems and for several thicknesses. For Pd/Pt(100), the maximum rate of inserted hydrogen $(H/Pd)_{max}$ strongly decreases with thickness reduction. Its value in correspondence of Pd_{5ML}/Pt(100) is only slightly higher than the α_{max} insertion rate of bulk Pd. The two-phase plateau region presents a slope and its width decreases with the thickness diminishing. Such a slope is not observed with unsupported Pd nanoparticles with equivalent size, confirming that it is due to a substrate effect.

Contrary to Pd/Pt(100), hydrogen evolution reaction is not well separated from hydrogen insertion and desinsertion for Pd/Pt(111). The classical method used to measure electrochemical isotherms for Pd/Pt(100) cannot be used in the case of deposits thinner than about 10 ML. For this reason we have developed a new experimental setup using hanging meniscus rotating disk electrode. We used it in combination with a new calculation method. We were able to record hydrogen insertion isotherm on Pd/Pt(111) with thicknesses down to about 4 ML.

Like for Pd/Pt(100), $(H/Pd)_{max}$ decreases with Pd/Pt(111) film thickness reduction. Nevertheless, for the same thickness, hydrogen solubility is higher in Pd/Pt(111) compared to Pd/Pt(100). The plateau region exhibits a slope, but it extends over a larger potential interval (60 mV versus 20 mV for Pd/Pt(100)). We could link the isotherm behaviour observed as a function of the thickness to the structure at the atomic level of the hydride Pd film measured with *in situ* Surface X-ray diffraction. The main role of substrate induced constraints on the Pd deposit has been revealed.

During this thesis work, we showed that the crystallographic orientation of the substrate has a strong influence on several aspects. First, deposition potentials and associated UPD processes depend from the orientation. Second, the morphology of Pd nanofilms is very different. Even if only the first layer is Under Potentially

Deposited onto Pt(111), the deposit shows a pseudomorphic growth up to about ten complete adlayers. In opposite, the two first complete Pd layers on Pt(100) are followed by a 3D growth of pyramidal square based structures following the substrate's orientation. Third, the Pd-H isotherms evolve differently. $(H/Pd)_{max}$ decreases faster with thickness reduction for Pd/Pt(100) compared to Pd/Pt(111). The potential range of the plateau is three times smaller for Pd/Pt(100) versus Pd/Pt(111).

6 Annex I

6.1 Complexation Equilibria

Complexation reactions[1] involve a salt of $PdCl_2$ that dissociates according to the (Equation 6.1).

$$PdCl_2 \rightleftarrows Pd^{2+} + 2\,Cl^- \quad \textbf{(Equation 6.1)}$$

This metal ion Pd^{2+} reacting with a ligand Cl^- to form a complex: $PdCl_1^+$; $PdCl_2$; $PdCl_3^-$ and $PdCl_4^{2-}$. Complexation reactions occur in a stepwise fashion: the reaction showed is often followed by additional reactions:

$(n = 1)$ $$Pd^{2+} + Cl^- \overset{K_1}{\Leftrightarrow} PdCl^+ \quad \textbf{(Equation 6.2)}$$

$(n = 2)$ $$PdCl^+ + Cl^- \overset{K_2}{\Leftrightarrow} PdCl_2 \quad \textbf{(Equation 6.3)}$$

$(n = 3)$ $$PdCl_2 + Cl^- \overset{K_3}{\Leftrightarrow} PdCl_3^- \quad \textbf{(Equation 6.4)}$$

$(n = 4)$ $$PdCl_3^- + Cl^- \overset{K_4}{\Leftrightarrow} PdCl_4^{2-} \quad \textbf{(Equation 6.5)}$$

The equilibrium constants for complex formation reactions are generally written as formation constants. Thus, each of the Reaction through is associated with a stepwise formation constant through K_n.

$$K_n = \frac{\text{products}}{\text{reagents}} \quad \textbf{(Equation 6.6)}$$

We can also write the equilibria as the sum of individual steps. These have overall formation constants designated by the symbol β as shown in

$$\beta_n = K_1 K_2 \cdots K_n \quad \textbf{(Equation 6.7)}$$

$$(K_1 = 1.26x10^6;\ K_2 = 3.98x10^4;\ K_3 = 3.16x10^2;\ K_4 = 3.98x10^2)^2$$

The $[Pd^{2+}]_{total}$ is know to 10^{-4} M (initial concentration) and it can be represented through the (Equation 6.8).

$$[Pd^{2+}]_{total} = [Pd^{2+}] + [PdCl^+] + [PdCl_2] + [PdCl_3^-] + [PdCl_4^{2-}] \quad \textbf{(Equation 6.8)}$$

However this concentration can be expressed in $[Cl^-]$, merging the (Equation 6.9) and (Equation 6.10).

$$[Pd^{2+}]_{total} = [Pd^{2+}] \cdot (1 + \beta_1[Cl^-] + \beta_2[Cl^-]^2 + \beta_3[Cl^-]^3 + \beta_4[Cl^-]^4) \quad \textbf{(Equation 6.9)}$$

We can replace overall formation constants (β) from the equilibrium constants (K).

$$[Pd^{2+}]_{total} = [Pd^{2+}] \cdot (1 + K_1[Cl^-] + K_1K_2[Cl^-]^2 + K_1K_2K_3[Cl^-]^3 + K_1K_2K_3K_4[Cl^-]^4) \quad \textbf{(Equation 6.10)}$$

Therewith we is possible calculated the fraction of each species in solution, it is represented with an α shown in the (Equation 6.11).

$$\alpha_n = \frac{PdCl_n^{(2-n)}}{[Pd^{2+}]_{total}} \quad \textbf{(Equation 6.11)}$$

Thus it is merged the (**Equation I.J)** and **(Equation 6.11**).

$$\alpha_{(Pd^{2+})} = \frac{1}{1 + K_1[Cl^-] + K_1K_2[Cl^-]^2 + K_1K_2K_3[Cl^-]^3 + K_1K_2K_3K_4[Cl^-]^4} \quad \textbf{(Equation 6.12)}$$

$$\alpha_{(PdCl^+)} = \frac{K_1[Cl^-]}{1 + K_1[Cl^-] + K_1K_2[Cl^-]^2 + K_1K_2K_3[Cl^-]^3 + K_1K_2K_3K_4[Cl^-]^4} \quad \textbf{(Equation 6.13)}$$

$$\alpha_{(PdCl_2)} = \frac{K_1K_2[Cl^-]^2}{1 + K_1[Cl^-] + K_1K_2[Cl^-]^2 + K_1K_2K_3[Cl^-]^3 + K_1K_2K_3K_4[Cl^-]^4} \quad \textbf{(Equation 6.14)}$$

$$\alpha_{(PdCl_3^-)} = \frac{K_1K_2K_3[Cl^-]^3}{1 + K_1[Cl^-] + K_1K_2[Cl^-]^2 + K_1K_2K_3[Cl^-]^3 + K_1K_2K_3K_4[Cl^-]^4} \quad \textbf{(Equation 6.15)}$$

$$\alpha_{(PdCl_4^{2-})} = \frac{K_1K_2K_3K_4[Cl^-]^4}{1 + K_1[Cl^-] + K_1K_2[Cl^-]^2 + K_1K_2K_3[Cl^-]^3 + K_1K_2K_3K_4[Cl^-]^4} \quad \textbf{(Equation 6.16)}$$

It is possible evaluated the fraction of each species in function of $[Cl^-]_{sol}$, as shown in the Figure 6.1.

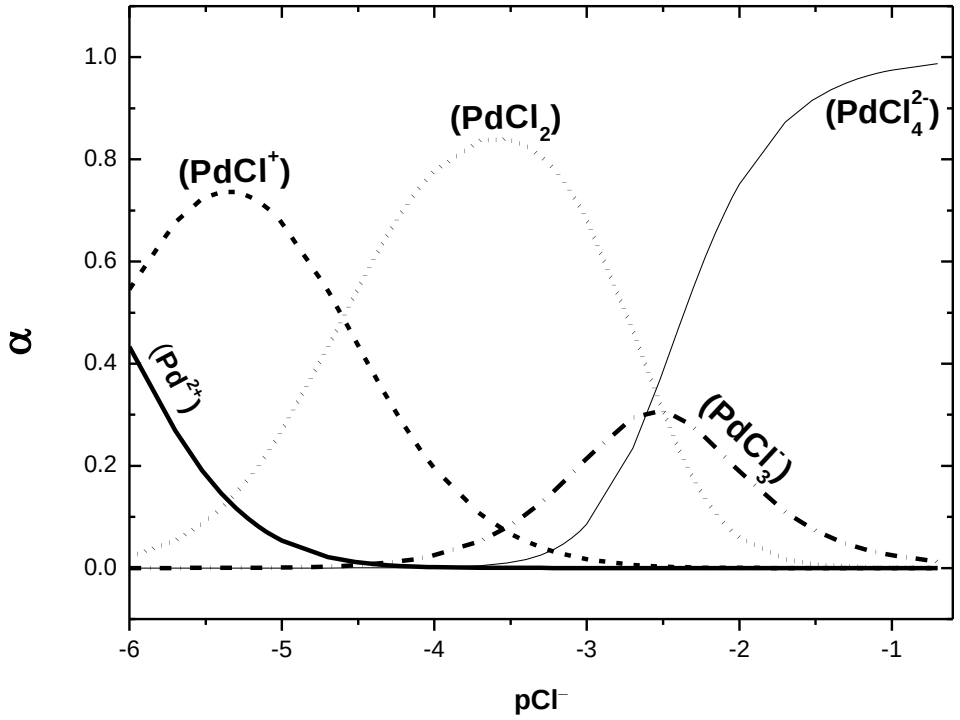

Figure 6.1 : Composition of Pd complex in solutions as a function of $[Cl^-]_{sol}$.

Note that these equilibrium constant are analogous to the a expressions we wrote for polyfunctional acids and bases except that the equations here are written in terms of formation equilibria while those for acids or bases are written in terms of dissociation equilibria. Also, the master variable is the ligand concentration Cl^- instead of the solution. The denominators are the same for each a value.

The total chloride concentration $[\mathrm{Cl}^-]_{\mathrm{initial}}$ can be written:

$$[\mathrm{Cl}^-]_{\mathrm{initial}} = [\mathrm{Cl}^-]_{\mathrm{sol}} + [\mathrm{PdCl}^+] + 2 \cdot [\mathrm{PdCl}_2] + 3 \cdot [\mathrm{PdCl}_3^-] + 4 \cdot [\mathrm{PdCl}_4^{2-}] \qquad \textbf{(Equation 6.17)}$$

However the species can be represented in function of $[Pd^{2+}]_{total}$ and its fraction.

$$[\mathrm{Cl}^-]_{\mathrm{initial}} = [\mathrm{Cl}^-]_{\mathrm{sol}} + \alpha_{(\mathrm{PdCl}^+)} \cdot [\mathrm{Pd}^{2+}]_{\mathrm{Total}} + 2 \cdot \alpha_{(\mathrm{PdCl_2})} \cdot [\mathrm{Pd}^{2+}]_{\mathrm{Total}} + 3 \cdot \alpha_{(\mathrm{PdCl_3^-})} \cdot [\mathrm{Pd}^{2+}]_{\mathrm{Total}} + 4 \cdot \alpha_{(\mathrm{PdCl_4^{2-}})} \cdot [\mathrm{Pd}^{2+}]_{\mathrm{Total}}$$ **(Equation 6.18)**

Using the values found in Figure 6.1 for fraction of the Pd complex is possible find the amount of $[\mathrm{Cl}^-]_{\mathrm{initial}}$ versus $[\mathrm{Cl}^-]_{\mathrm{sol}}$, as show in

Figure 6.2.

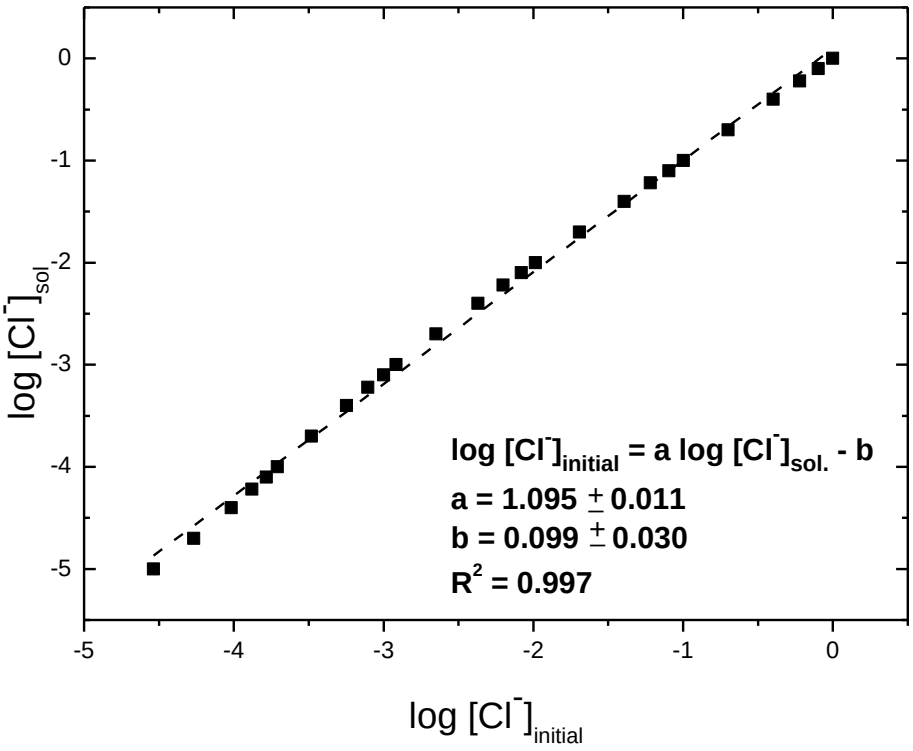

Figure 6.2: Composition of $[Cl^-]_{sol.}$ in solution as a function of $[Cl^-]_{initial}$.

Through of

Figure 6.2 we can find the equation of the line and so the $[\mathrm{Cl}^-]_{\mathrm{sol}}$ in solution. For this stimulate α, in other words, the fraction of the each species. After, it uses the (Equation 6.18) for calculate values for each species. The values calculated are represented in the Table 2.1 (Chapter 2).

6.2 Reference

(1) Skoog, D. A. *Fundamentals of Analytical Chemistry*; Boeck, D., Ed.; 8th ed.; Brooks Cole, 2004; p. 1176.

(2) Droll, H. A.; Block, B. P.; Fernelius, W. C. *The Journal of Physical Chemistry* **1957**, *61*, 1000–1004.

Table of Contents

Introduction

Le développement économique de la majorité des pays repose largement sur l'utilisation des énergies fossiles, ce qui pose de nombreux problèmes environnementaux (pollution, modification du climat..). Dans ce contexte, l'exploitation rationnel d'énergies propres et renouvelables est un défi mondial. L'hydrogène, en tant que vecteur d'énergie, pourrait être une technologie clé. Néanmoins, son utilisation à grande échelle présent encore des difficultés, entre autre à cause de son stockage difficile. L'hydrogène est léger et très inflammable. Sa compression, sa liquéfaction et sa conversion en hydrures métalliques sont les principales méthodes à l'étude.

Le palladium est largement étudié dans différents domaines en raison de ses bonnes propriétés catalytiques dans les réactions mettant en jeu de l'hydrogène. En particulier, il est très efficace vis-à-vis de l'insertion/desinsertion de l'hydrogène atomique. Même si en pratique, il ne présente pas d'intérêt pour le stockage de l'hydrogène à cause de son prix élevé et de dégradations importantes, il constitue un système modèle pour la compréhension des mécanismes mis en jeu dans les processus d'insertion/desinsertion d'hydrogène dans les solides. Des alliages légers à base de Li ou de Mg présentent de hautes capacités de stockage. Inversement, ils possèdent une faible cinétique de rupture de la liaison de H_2 et ils peuvent être oxydés par des traces d'oxygène ou d'eau. Une proposition est de recouvrir ces alliages légers avec de fines couches de Pd. Ceci fournirait une haute activité catalytique pour la dissociation de H_2, protégerait le matériau des contaminations mais minimiserait les quantités de Pd. L'étude des propriétés des films ultra-minces de Pd pour l'insertion/desinsertion d'hydrogène est l'objectif de ce travail, où les effets de taille nanométrique et l'influence du support doivent être pris en compte.

Afin d'obtenir une meilleure compréhension des phénomènes, nous nous sommes penchés sur des nanofilms de Pd bien définis à l'échelle atomique. Ils ne peuvent être obtenus qu'en utilisant des substrats bien définis comme des monocristaux taillés suivant des orientations cristallographiques bien précises. Nous avons retenu le platine comme premier substrat car son paramètre de maille est très proche de celui du Pd (+0.7 %), ce qui doit permettre une croissance pseudomorphe,

au moins pour les premières couches atomiques. Deux orientations différentes, Pt(100) et Pt(111), ont été étudiées.

Dans notre étude, nous avons commencé par développer la préparation de nanofilms de Pd sur Pt(100), en s'inspirant de la procédure développée précédemment pour Pd/Pt(111) par C. Lebouin au LEPMI. Dans un second temps, nous avons étudié l'insertion d'hydrogène dans les nanofilms de Pd à la fois pour Pd/Pt(111) et Pd/Pt(100). L'insertion d'hydrogène est réalisée par réduction électrochimique de H^+ en solution acide. La quantité d'hydrogène inséré est déduite des mesures de charge à l'électrode. Cependant, des réactions comme le dégagement d'hydrogène peuvent se produire en parallèle. Nous n'avons pas pu éliminer leur contribution pour les films les plus minces de Pd/Pt(111) avec les méthodes existantes. Pour ce système, nous avons développé une nouvelle méthode de mesure des isothermes d'insertion en utilisant une électrode tournante à ménisque suspendu d'électrolyte.

7 Électrodépôt de films minces de Pd sur Pt(100)

7.1 Méthodes expérimentales

7.1.1 Montage électrochimique

Deux cellules électrochimiques ont été utilisées pour le dépôt des films de Pd, comme représenté par la Figure 2.1. Les cellules en Pyrex à double-enceinte permettent le contrôle de la température (25°C). Une cellule est utilisée pour les caractérisations électrochimiques, l'autre pour l'électro-dépôt de Pd.

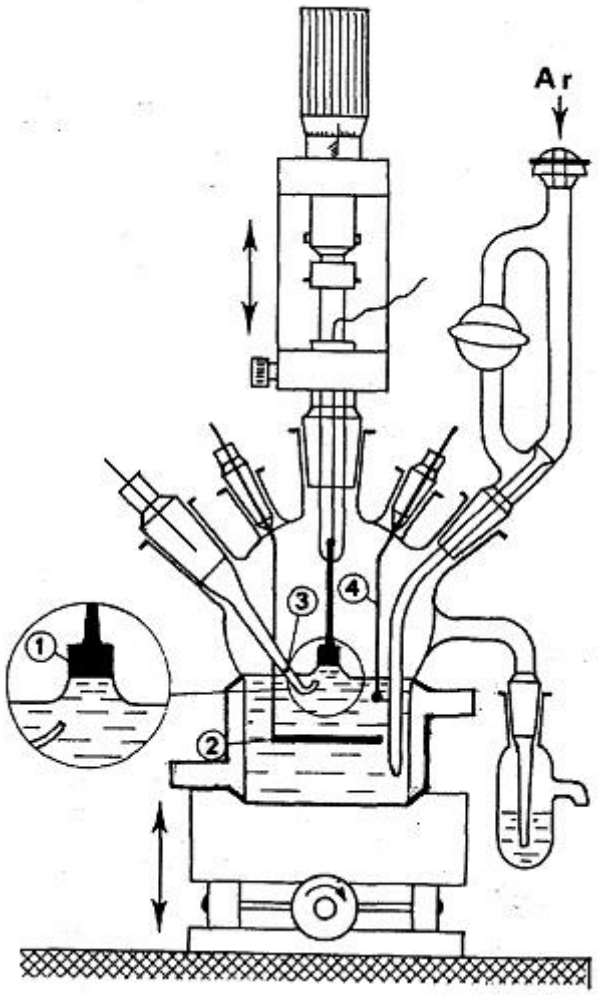

Figure 7.1: Schéma d'une cellule électrochimique (1) électrode de travail, (2) contre-électrode, (3) électrode de référence, (4) électrode auxiliaire.

L'électrode de travail est toujours utilisée en configuration à ménisque suspendu pour s'assurer que seule la face avant du cristal, qui correspond à l'orientation cristallographique souhaitée, soit en contact avec l'électrolyte.

L'électrode de référence est une Electrode de Référence à Hydrogène (ERH) préparée avant chaque expérience.

Les mesures ont été réalisées avec un potentiostat PAR 273A.

7.1.2 Préparation de la surface Pt(100)

La surface est préparée par traitement thermique suivant la méthode développée par Clavilier *et al.*[1]. Un recuit dans une flamme H_2/Air est appliqué pendant 10 mn. Ceci permet de régénérer l'alignement des atomes de surface et d'éliminer les impuretés organiques par pyrolyse. L'électrode est ensuite refroidie dans une atmosphère réductrice (H_2/Ar : 1/9) pour éviter la formation d'oxydes de surface[2,3]. Lorsque la surface est suffisamment froide, elle est mise en contact avec une solution saturée du même mélange afin de prévenir l'adsorption d'impuretés, en particulier durant le transfert vers la cellule électrochimique. La qualité de la surface est contrôlée en réalisant un voltammogramme dans H_2SO_4 0.1 M qui doit correspondre à une signature typique[1–3].

7.1.3 Dépôt électrochimique de Pd

Après caractérisation électrochimique, l'électrode Pt(111) est transférée dans la cellule de dépôt contenant une solution de H_2SO_4 0.1 M + $PdCl_2$ 10^{-4} M + x HCl (x=$3\cdot10^{-3}$ M, $6\cdot10^{-3}$ M, $9\cdot10^{-3}$ M). L'électrode de travail est introduite à 0.95 V_{ERH} pour éviter à la fois la formation d'oxyde et le dépôt de Pd. Le potentiel est alors balayé à 0.1 $mV.s^{-1}$ vers des basses valeurs correspondant à la limite de diffusion des ions Pd^{2+} en solution. Le potentiel est alors maintenu jusqu'à obtention de la quantité souhaitée de Pd. Cette méthode de dépôt a déjà été utilisée pour Pd sur Pt(111) et a permis d'obtenir des films assez plats et pseudomorphes jusqu'à 10 ML (Mono-Layer)[10,11].

La quantité de Pd déposée est mesurée par coulométrie en supposant un atome de Pd par atome de Pt en surface et un transfert de charge de deux électrons par atome. La charge correspondant à une monocouche (Q_{ML}) est égale à 418 $\mu c.cm^{-2}$. Le taux de couverture du Pd est exprimé comme un nombre équivalent de monocouches x ML sans tenir compte de la morphologie réelle du dépôt[11].

7.2 Électrodépôt de Pd/Pt(100)

La figure 2.3 montre le voltamogramme de Pt(100) dans $PdCl_2$ 10^{-4} M + HCl $3{\cdot}10^{-3}$ M + H_2SO_4 0.1 M à la vitesse de 0.1 mV·s^{-1}.

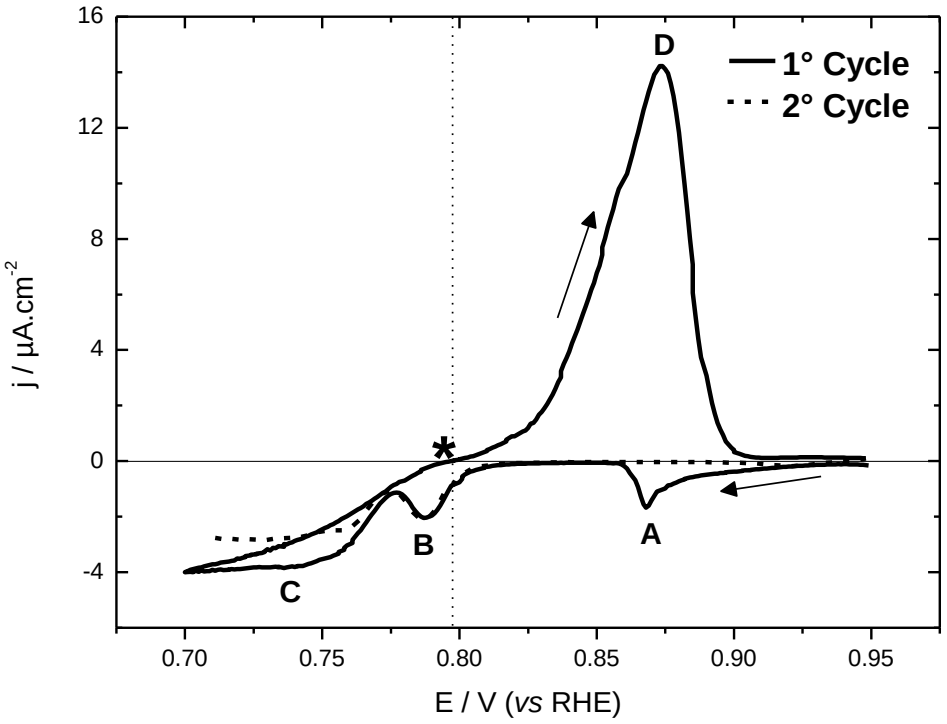

Figure 7.2 : Pt(100) dans $PdCl_2$ 10^{-4} M + HCl $3{\cdot}10^{-3}$ M + H_2SO_4 0.1 M à 0.1 mV·s^{-1}. Premier cycle (ligne continue) et début du second cycle (tirets). Potentiel d'équilibre théorique (ligne pointillée) et expérimental (*).

Les pics A (0.87 V_{ERH}) et B (0.78 V_{ERH}) sont présents durant le balayage négatif. La région C est caractéristique de la limite de diffusion avec un courant constant. Un profil de courant semblable a été trouvé pour Pt(111)[11], à l'exception de la présence du pic B et de l'absence d'un petit pic d'oxydation à haut potentiel durant le balayage positif.

La position du pic A est toujours au-dessus du potentiel de Nernst (potentiel d'équilibre). Cela correspond à un processus de dépôt en sous tension (UPD : under potential deposition) : le dépôt électrochimique d'une (fraction de) couche atomique se produit à un potentiel supérieur au potentiel de Nernst du dépôt massif[11,28]. La charge du pic A est égale à 395 µC.cm^{-2}. Cette valeur est proche de la charge

théorique d'une monocouche (418 µC.cm^{-2}). Cela suggère que le pic A correspond au dépôt d'une première couche atomique.

Le pic B se développe majoritairement en-dessous du potentiel de Nernst mais il débute au-dessus. Ce dernier point suggérerait que nous sommes aussi en présence d'un UPD. À l'inverse, le pic B n'est pas bien séparé du dépôt massif (le courant ne retourne pas à zéro entre les pics B et C). La charge du pic B est calculée par intégration du courant depuis les hauts potentiels jusqu'au minimum de courant entre les pics B et C. Elle est égale à 415 µC.cm^{-2}. Cela suggère que le pic B correspond au dépôt d'une seconde couche atomique. Bien que les charges des pics B et C correspondent respectivement à une couche atomique chacune, nous ne connaissons pas la morphologie des dépôts associés. L'assignation de ces pics sera discutée en détail au paragraphe 2.4 à l'aide des caractérisations électrochimiques. Le pic C s'apparente plus à un plateau. Il est bien en-dessous du potentiel de Nernst. Il est associé au dépôt massif de Pd. Le plateau correspond à la limite de diffusion des espèces Pd^{2+} venant du cœur de la solution.

Un seul pic de dissolution, D (0.87 V_{ERH}) est observé durant le balayage positif de potentiel, ne permettant pas de distinguer les différentes contributions (dissolutions des pics A, B et C). Le potentiel du pic D est significativement supérieur à ceux des pics et C. Inversement, le pic A se superpose à la partie supérieure du pic D.

Durant le second balayage négatif (Figure 2.3), le pic d'UPD A n'est plus present. Cette observation ne peut être expliquée par le fait que que la première couche de Pd n'a pas été dissoute en-dessous de 0.95 V_{ERH}. Ainsi, le pic D de dissolution n'inclut pas la dissolution de l'UPD associé au pic A. Un phénomène similaire a déjà été rapporté dans le cas de Pd/Pt(111)[11] avec une dissolution incomplète de la première couche. Dans tous les cas, au-dessus de 0.95 V_{ERH}, il serait difficile de séparer la dissolution de l'UPD de la formation des oxydes de surfaces.

Inversement, durant le second cycle, la charge sous le pic B ne change pas significativement (410 µC.cm^{-2}), correspondant toujours au dépôt d'une second couche complète. Ainsi, de manière sûre, le pic D de dissolution inclut bien le dépôt associé au pic B. Le pic D correspond à la fois à la dissolution de la seconde couche de Pd et du dépôt massif.

7.2.1 Effet de la concentration en chlorure

La concentration en chlorure dans la solution de dépôt modifie le potentiel d'équilibre théorique d'une électrode de Pd. La figure 2.4 montre l'effet de différentes concentrations (x = $3{\cdot}10^{-3}$ M, $6{\cdot}10^{-3}$ M, $9{\cdot}10^{-3}$ M).

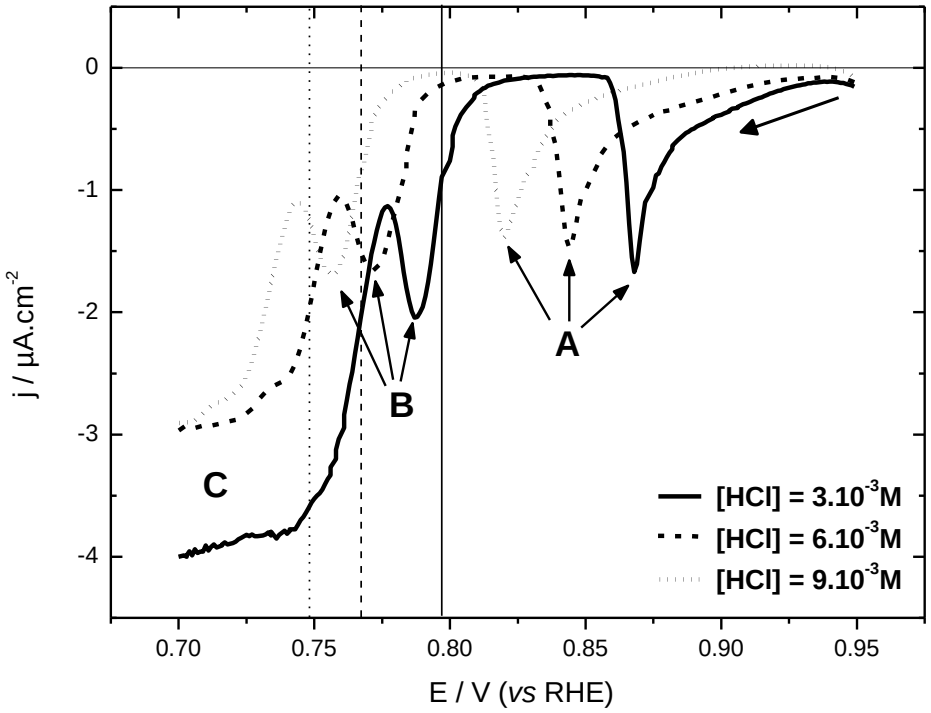

Figure 7.3 : Pt(100) dans $PdCl_2$ 10^{-4} M + H_2SO_4 0.1 M + x HCl (x = $3{\cdot}10^{-3}$ M ligne continue; $6{\cdot}10^{-3}$ M tirets; $9{\cdot}10^{-3}$ M pointillé), 0.1 $mV{\cdot}s^{-1}$. Les lignes verticales correspondent aux potentiels théoriques d'équilibre

Les changements de concentration en Cl^- ne modifient pas l'allure générale des courbes mais induisent un décalage global vers les bas potentiels avec l'augmentation de [Cl^-]. La table 2.3 montre l'effet sur les pics A et B.

[HCl] / M	**Pic A** / V *vs.* ERR	**Pic B** / V *vs.* ERH
3·10^{-3}	0.868	0.787
6·10^{-3}	0.844	0.771
9·10^{-3}	0.820	0.757

Table 7.1: Potentiel des pics A et B de la figure 2.4.

Le pic A se déplace vers les bas potentiels comme prévu par la théorie (environ 48 mV de $3 \cdot 10^{-3}$ M à $9 \cdot 10^{-3}$ M en pratique pour 49 mV en théorie). Inversement, le pic B ne se déplace que de 32 mV. Ceci suggère que des mécanismes différents sont en jeu pour les pics A et B. De plus, à 9.10^{-3} M, le maximum du pic B est 9 mV au-dessus du potentiel de Nernst, confirmant son caractère d'UPD. Nous constatons surtout que les concentrations plus élevées permettent une meilleure séparation entre le début du dépôt et la formation des oxydes. Aussi, nous avons retenu la concentration de 9.10^{-3} M pour HCl dans la suite.

7.3 Caractérisation électrochimique de Pd_{xML}/Pt(100)

Après dépôt, les électrodes ont été caractérisées par voltammétrie cyclique dans H_2SO_4 0.1 M.

7.3.1 De 1 ML à 2 ML

La Figure 2.6 montre les caractérisations de 1 à 2 ML ainsi que la signature de la surface libre de Pt(100).

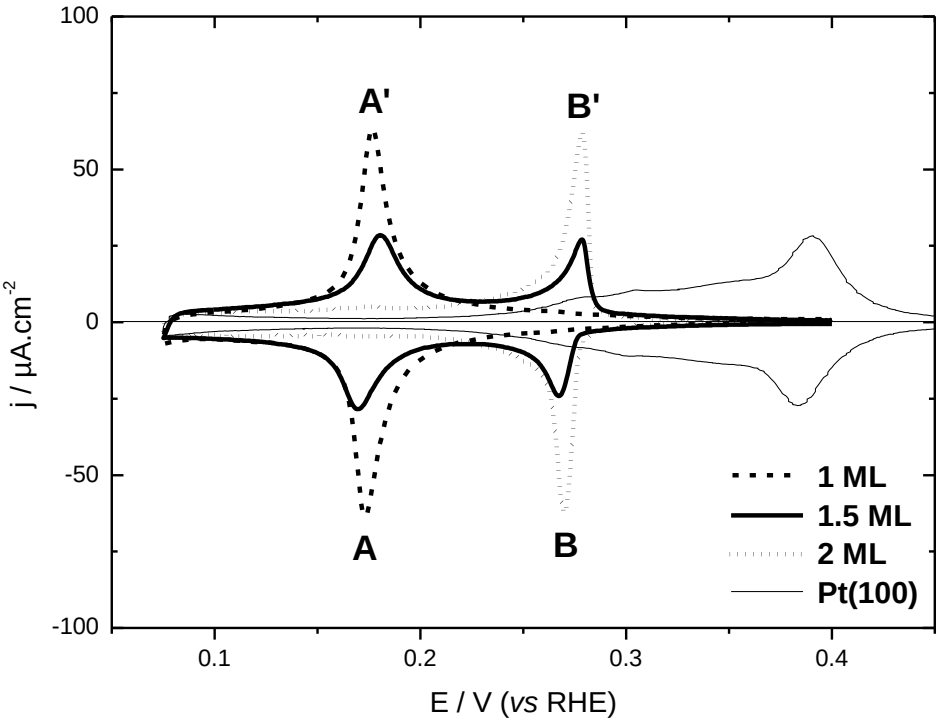

Figure 7.4 : Pd_{xML}/Pt(100) dans H_2SO_4 0.1 M, 10 $mV{\cdot}s^{-1}$.

Les différences sont remarquables. Dès 1 ML, la signature du Pt libre a complètement disparu, confirmant une couverture complète et homogène de la première couche, comme attendu pour un UPD. Le pic A/A' est une signature spécifique de la surface libre de la première couche de Pd. Il est absent sur Pt(100). Il est maximum pour Pd_{1ML}/Pt(100). Il diminue fortement pour $Pd_{1,5ML}$/Pt(100). Il a complètement disparu pour Pd_{2ML}/Pt(100). Ceci confirme le dépôt homogène de la seconde couche de Pd, toujours en accord avec un caractère UPD. Inversement, le pic B/B' semble être une signature spécifique de la seconde couche atomique. Il est absent pour Pd_{1ML}/Pt(100). Il croît pour $Pd_{1,5ML}$/Pt(100). Il est maximum pour Pd_{2ML}/Pt(100).

Il en résulte que le dépôt de Pd sur Pt(100) procède couche par couche au moins jusqu'à 2 couches. Ceci n'avait jamais été observé par voie électrochimique mais déjà constat en ultra-vide [8].

7.3.2 Au-delà de 2ML

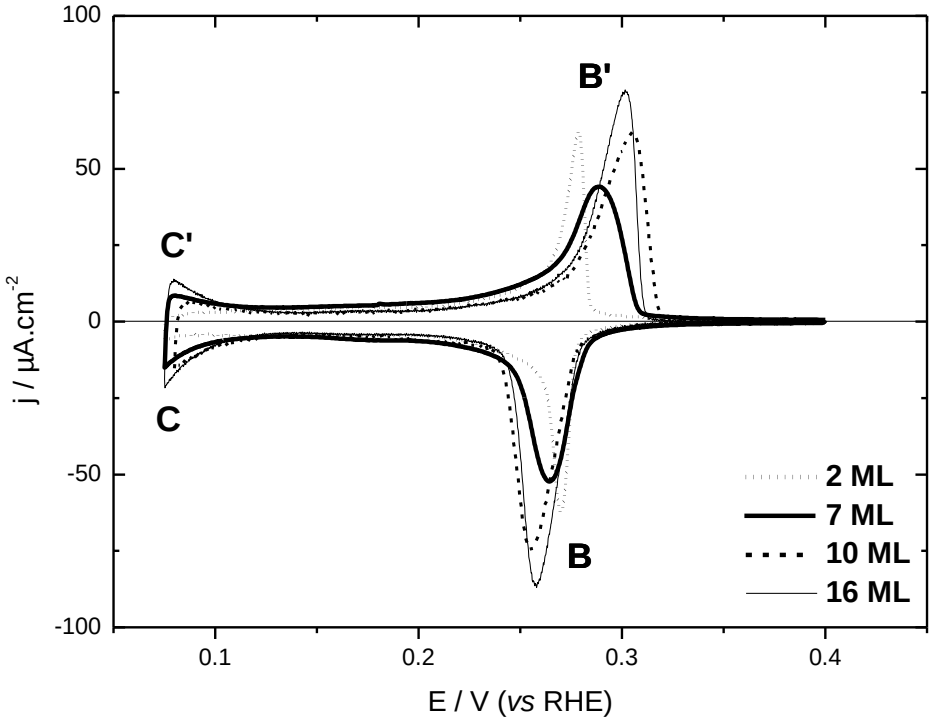

Figure 7.5 : PdxML/Pt(100) dans H_2SO_4 0.1 M, 10 $mV.s^{-1}$.

L'augmentation d'épaisseur de 2 à 16 ML n'induit pas l'apparition d'autres pics mais produit des déformations sur le pic B/B'. Il perd sa réversibilité, ce qui est habituellement associé à des croissances 3D[36–38].

7.4 Microscopie à force atomique

Nous avons réalise des mesures par microscopie à force atomique *ex situ*, en collaboration avec Mireille Maret du SIMAP.

7.4.1 Pd_{2ML}/Pt(100)

La figure 2.12 montre l'image AFM de Pd_{2ML}/Pt(100).

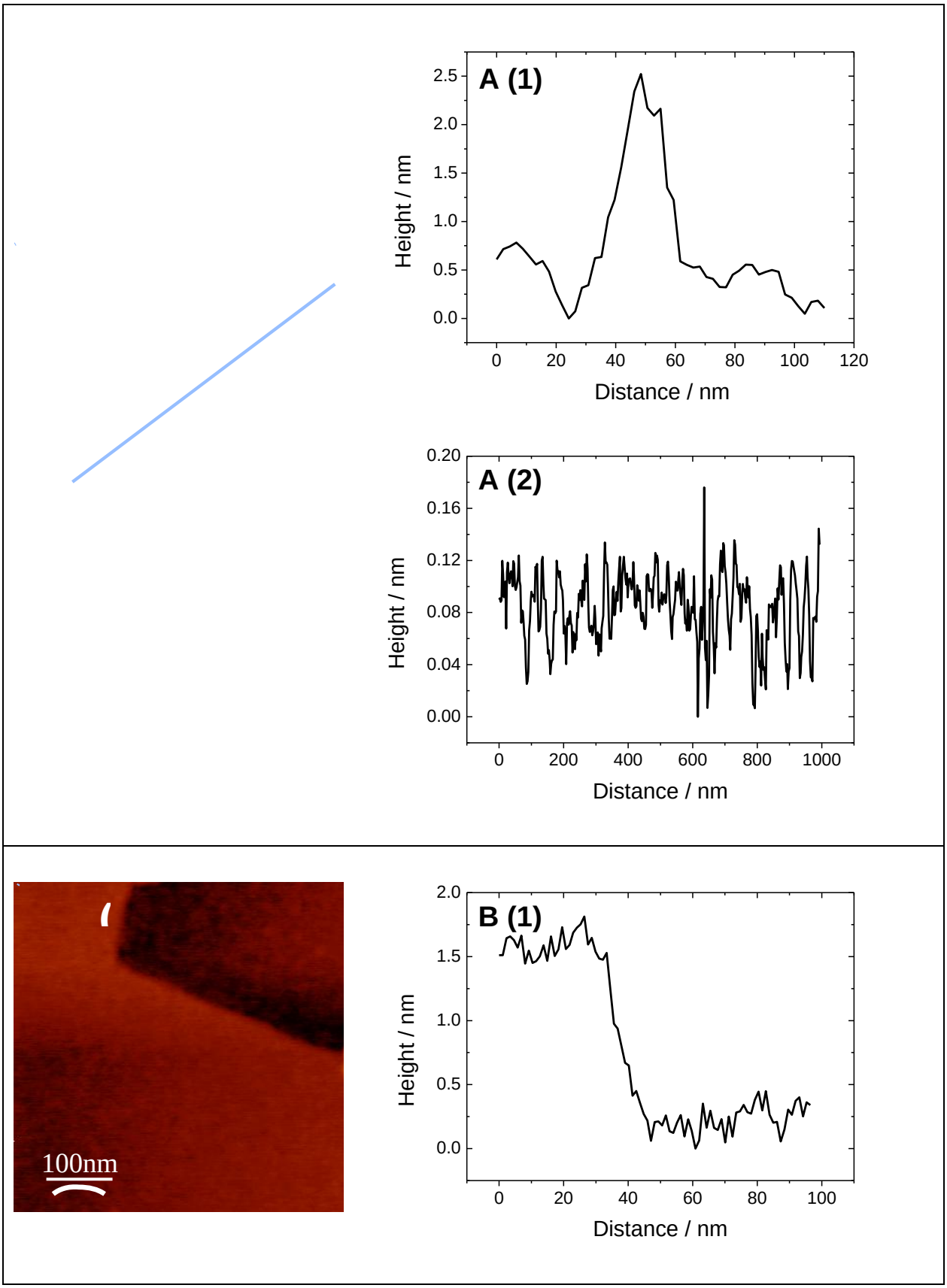

Figure 7.6: Images AFM *ex situ* de Pd_{2ML}/Pt(100) sample. Les profils (droite) sont représentés par des traits sur les images (gauche)

La surface de Pd_{2ML}/Pt(100) est très plate avec peu de defaults. Seules les marches atomiques correspondant au substrat apparaissent clairement.

7.4.2 Pd_{4ML}/Pt(100)

La figure 2.13 montre l'image AFM de Pd_{4ML}/Pt(100).

Deux zones distinctes ont été observées. La première (Figure 2.13 – A) correspond à des zones relativement plates même si quelques îlots sont observés. Dans d'autres zones (Figure 2.13 – B), la présence d'îlots est plus importante avec une rugosité RMS de 6,5 plans atomiques. Le profils des îlots montre une hauteur de 2,5 à 4 nm pour des largeurs d'envirob 25 nm.

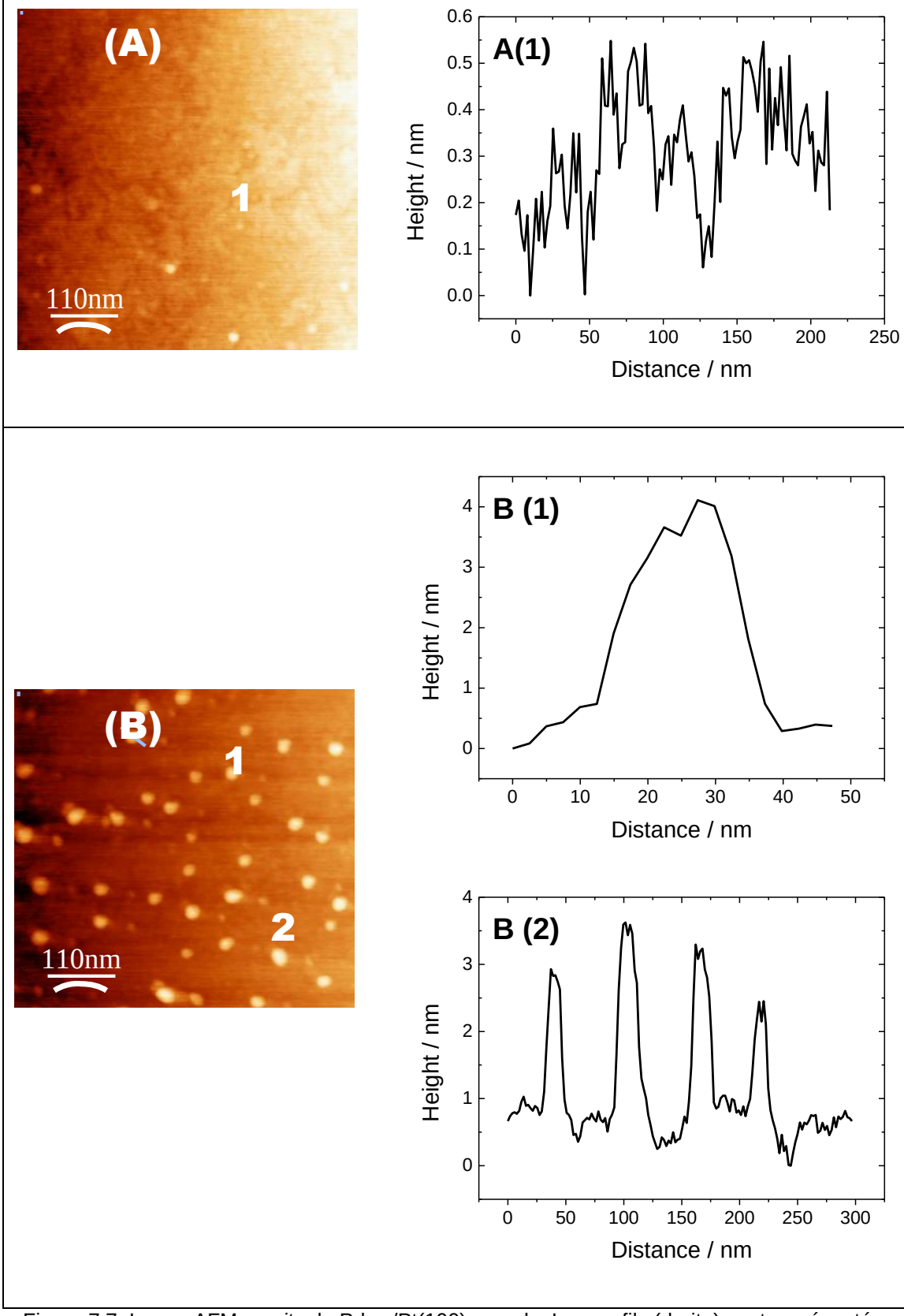

Figure 7.7: Image AFM *ex situ* de Pd_{4ML}/Pt(100) sample. Les profils (droite) sont représentés par des traits sur les images (gauche)

7.4.3 Pd_{14ML}/Pt(100)

La figure 2.14 montre l'image AFM de Pd_{14ML}/Pt(100).

La morphologie des dépôts est bien différente des autres épaisseurs. Il n'y a plus de zones plates mais principalement des pyramides à base carrée, toutes de même orientation. La rugosité est importante même si les pyramides présentent des pentes latérales inférieures à 45° comme on pourrait l'attendre pour une croissance préférentielle des facettes (111).

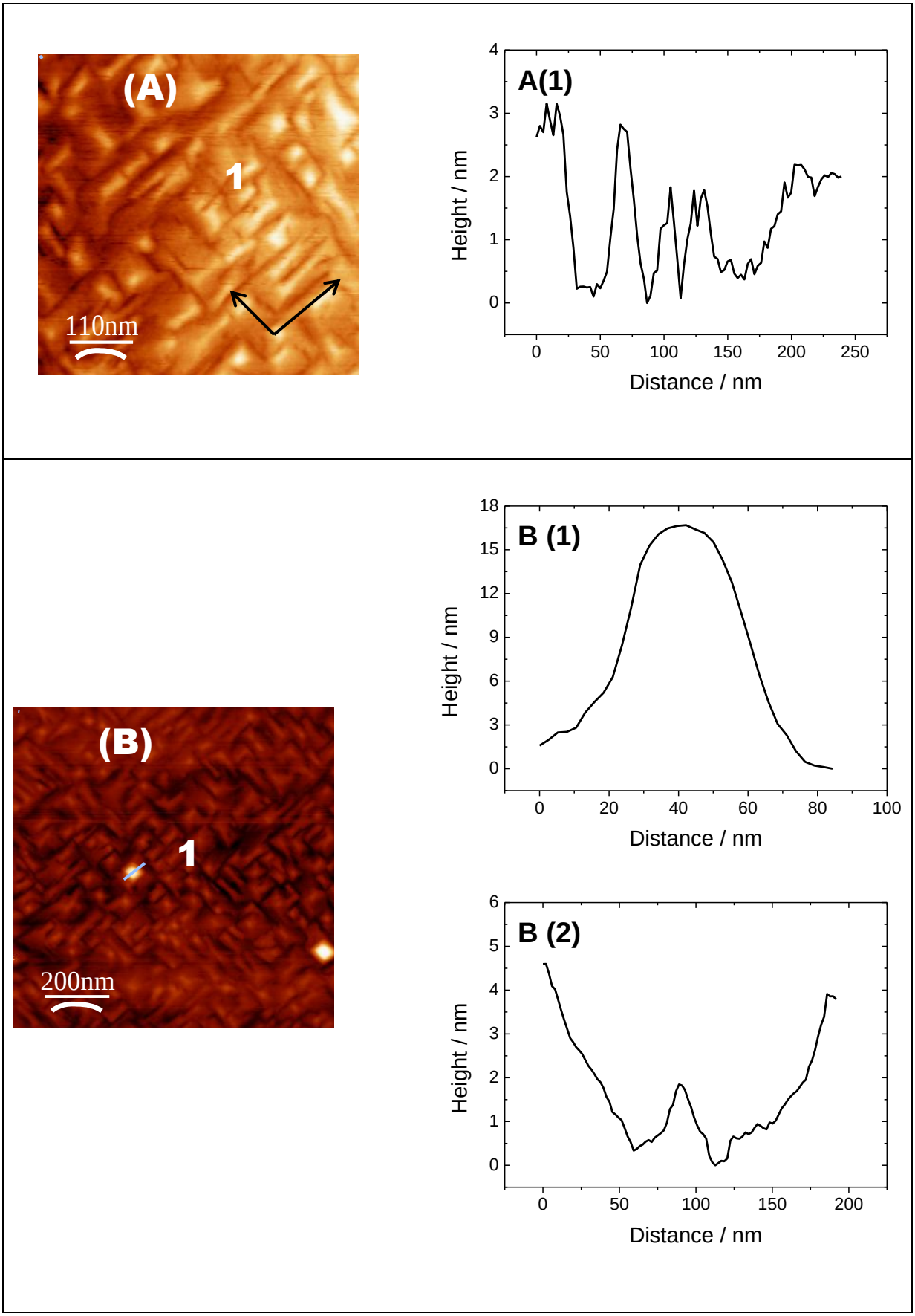

Figure 7.8: Images AFM *ex situ* de Pd_{14ML}/Pt(100) sample. Les profils (droite) sont représentés par des traits sur les images (gauche).

7.5 Conclusion

Ce chapitre a présenté l'étude de l'électro-dépôt et de la caractérisation des films Pd/Pt(100).

Nous avons réalisé les dépôts par balayage lent (0.1 $mV.s^{-1}$) de potentiel. Nous avons montré l'influence importante des chlorures, ce qui nous a conduit à choisir une concentration élevée de 9.10^{-3} M de Cl^-. Les deux premières couches se déposent successivement par un mécanisme d'UPD. Les couches suivantes, après apparition d'îlots, conduisent à une croissance 3D en pyramides.

7.6 References

(1) Clavilier, J.; Faure, R.; Guinet, G.; Durand, R. *Journal of Electroanalytical Chemistry and Interfacial Electrochemistry* **1979**, *107*, 205–209.

(2) Clavilier, J.; Armand, D.; Wu, B. L. *Journal of Electroanalytical Chemistry and Interfacial Electrochemistry* **1982**, *135*, 159–166.

(3) Kibler, L. A. *International Society of Electrochemistry* **2003**, 1–55.

(4) Kibler, L. a.; Cuesta, A.; Kleinert, M.; Kolb, D. M. *Journal of Electroanalytical Chemistry* **2000**, *484*, 73–82.

(5) Clavilier, J.; Armand, D.; Sun, S. G.; Petit, M. *Journal of Electroanalytical Chemistry and Interfacial Electrochemistry* **1986**, *205*, 267–277.

(6) Rodes, A.; Zamakhchari, M. A.; El Achi, K.; Clavilier, J. *Journal of Electroanalytical Chemistry and Interfacial Electrochemistry* **1991**, *305*, 115–129.

(7) Wagner, F. T.; Ross, P. N. *Journal of Electroanalytical Chemistry and Interfacial Electrochemistry* **1983**, *150*, 141–164.

(8) Attard, G. A.; Price, R. *Surface Science* **1995**, *335*, 63–74.

(9) Al-Akl, A.; Attard, G. A.; Price, R.; Timothy, B. *Journal of Electroanalytical Chemistry* **1999**, *467*, 60–66.

(10) Soldo-Olivier, Y.; Lafouresse, M. C.; De Santis, M.; Lebouin, C.; De Boissieu, M.; Sibert, E. *The Journal of Physical Chemistry C* **2011**, *115*, 12041–12047.

(11) Lebouin, C.; Soldo-Olivier, Y.; Sibert, E.; Millet, P.; Maret, M.; Faure, R. *Journal of Electroanalytical Chemistry* **2009**, *626*, 59–65.

(12) Skoog, D. A. *Fundamentals of Analytical Chemistry*; Boeck, D., Ed.; 8th ed.; Brooks Cole, 2004.

(13) Kibler, L. a.; Kleinert, M.; Randler, R.; Kolb, D. M. *Surface Science* **1999**, *443*, 19–30.

(14) Sassani, D. C.; Shock, E. L. *Geochimica et Cosmochimica Acta* **1998**, *62*, 2643–2671.

(15) Crosby, J. N.; Harrison, J. A.; Whitfield, T. A. *Electrochimica Acta* **1981**, *26*, 1647–1651.

(16) Droll, H. A.; Block, B. P.; Fernelius, W. C. *The Journal of Physical Chemistry* **1957**, *61*, 1000–1004.

(17) Harrison, J. a.; Hill, R. P. J.; Thompson, J. *Journal of Electroanalytical Chemistry and Interfacial Electrochemistry* **1973**, *47*, 431–440.

(18) Harrison, J. a.; Sierra Alcazar, H. B.; Thompson, J. *Journal of Electroanalytical Chemistry and Interfacial Electrochemistry* **1974**, *53*, 145–150.

(19) Harrison, J. A.; Thompson, J. *Electrochimica Acta* **1973**, *18*, 829–834.

(20) Attard, G. a.; Hazzazi, O.; Wells, P. B.; Climent, V.; Herrero, E.; Feliu, J. M. *Journal of Electroanalytical Chemistry* **2004**, *568*, 329–342.

(21) Álvarez, B.; Berná, a.; Rodes, a.; Feliu, J. M. *Surface Science* **2004**, *573*, 32–46.

(22) Paunovic, M.; Schlesinger, M. *Fundamentals of electrochemical deposition*; second.; John Wiley & Sons, Inc., 2006.

(23) Schlesinger, M.; Paunovic, M.; Abys, J. A. *Modern Electroplating*; 5th ed.; Wiley, 2010.

(24) Bard, A. J.; Faulkner, L. R. *ELECTROCHEMICAL METHODS Fundamentals and Applications*; JOHN WILEY & SONS, I., Ed.; 2nd ed.; 2001.

(25) Haynes, W. M. *Handbook of Chemistry and Physics*; 93rd ed.; CRC Press, 2012.

(26) Schlesinger, M.; Paunovic, M. *Modern Electroplating*; 5th ed.; Wiley, 2010.

(27) Castellan, G. W. *Physical Chemistry*; 3rd ed.; Addison-Wesley Publishing Company, Inc., 1983.

(28) Leiva, E. P. M. *Electrochimica Acta* **1996**, *41*, 2185–2206.

(29) Duncan, H.; Lasia, A. *Electrochimica Acta* **2007**, *52*, 6195–6205.

(30) Llorca, M. J.; Feliu, J. M.; Aldaz, A.; Clavilier, J. *Journal of Electroanalytical Chemistry* **1994**, *376*, 151–160.

(31) Llorca, M. J.; Feliu, J. M.; Aldaz, A.; Clavilier, J. *Journal of Electroanalytical Chemistry* **1993**, *351*, 299–319.

(32) Ball, M. J.; Lucas, C. a.; Marković, N. M.; Stamenković, V.; Ross, P. N. *Surface Science* **2003**, *540*, 295–302.

(33) Roudgar, A.; Groß, A. *Journal of Electroanalytical Chemistry* **2003**, *548*, 121–130.

(34) Lebouin, C.; Soldo-Olivier, Y.; Sibert, E.; De Santis, M.; Maillard, F.; Faure, R. *Langmuir* **2009**, *25*, 4251–5.

(35) Sibert, E.; Ozanam, F.; Maroun, F.; Behm, R. J.; Magnussen, O. M. *Surface Science* **2004**, *572*, 115–125.

(36) Duncan, H.; Lasia, A. *Journal of Electroanalytical Chemistry* **2008**, *621*, 62–68.

(37) Ball, M. J.; Lucas, C. a.; Marković, N. M.; Stamenkovic, V.; Ross, P. N. *Surface Science* **2002**, *518*, 201–209.

(38) Hoyer, R.; Kibler, L. a.; Kolb, D. M. *Electrochimica Acta* **2003**, *49*, 63–72.

(39) Lebouin, C. Films d'épaisseurs nanométriques de Pd sur Pt(111): élaboration, caractérisations et étude de l'électro-insertion de l'hydrogène, Grenoble University, 2008.

(40) Inukai, J.; Ito, M. *Journal of Electroanalytical Chemistry* **1993**, *358*, 307–315.

(41) El-Aziz, a. M.; Hoyer, R.; Kibler, L. a.; Kolb, D. M. *Electrochimica Acta* **2006**, *51*, 2518–2522.

(42) Climent, V.; Marković, N. M.; Ross, P. N. *The Journal of Physical Chemistry B* **2000**, *104*, 3116–3120.

(43) Arenz, M.; Stamenkovic, V.; Schmidt, T. J.; Wandelt, K.; Ross, P. N.; Marković, N. M. *Surface Science* **2003**, *523*, 199–209.

(44) Attard, G. A.; Bannister, A. *Journal of Electroanalytical Chemistry and Interfacial Electrochemistry* **1991**, *300*, 467–485.

(45) Arenz, M.; Stamenkovic, V.; Schmidt, T. J.; Wandelt, K.; Ross, P. N.; Marković, N. M. *Surface Science* **2002**, *506*, 287–296.

(46) Álvarez, B.; Climent, V.; Rodes, A.; Feliu, J. M. *Physical Chemistry Chemical Physics* **2001**, *3*, 3269–3276.

(47) Álvarez, B.; Climent, V.; Rodes, a.; Feliu, J. M. *Journal of Electroanalytical Chemistry* **2001**, *497*, 125–138.

(48) Marković, N. M.; Lucas, C. A.; Climent, V.; Stamenković, V.; Ross, P. N. *Surface Science* **2000**, *465*, 103–114.

(49) Álvarez, B.; Feliu, J. M.; Clavilier, J. *Electrochemistry Communications* **2002**, *4*, 379–383.

(50) Clavilier, J.; Llorca, M. J.; Feliu, J. M.; Aldaz, a. *Journal of Electroanalytical Chemistry and Interfacial Electrochemistry* **1991**, *310*, 429–435.

(51) Schmickler, W. *Chemical Physics* **1990**, *141*, 95–104.

(52) Lehnert, W.; Schmickler, W. *Journal of Electroanalytical Chemistry and Interfacial Electrochemistry* **1991**, *310*, 27–37.

(53) Binnig, G.; Quate, C. F. *Physical Review Letters* **1986**, *56*, 930–933.

(54) Giessibl, F. J. *Reviews of Modern Physics* **2003**, *75*, 949–983.

(55) Dupas, C.; Houdy, P.; Lahmani, M. *Nanoscience: Nanotechnologies and Nanophysics*; Springer, verlag B., Ed.; 2007.

(56) Núñez, M. E. Biophysics of Bacterial Biofilms http://www.mtholyoke.edu/~menunez/ResearchPage/AFM.html.

(57) Miller, J. D.; Veeramasuneni, S.; Drelich, J.; Yalamanchili, M. R.; Yamauchi, G. *Polymer Engineering & Science* **1996**, *36*, 1849–1855.

(58) Khulbe, K. C.; Feng, C. Y.; Matsuura, T. *Synthetic Polymeric Membranes*; Springer Berlin Heidelberg: Berlin, Heidelberg, 2008.

(59) Boussu, K.; Van der Bruggen, B.; Volodin, A.; Snauwaert, J.; Van Haesendonck, C.; Vandecasteele, C. *Journal of colloid and interface science* **2005**, *286*, 632–8.

8 Insertion d’hydrogène dans Pd

8.1 Système Pd/Pt(100)-H

La méthode la plus courante pour déterminer les quantités d'hydrogène inséré utilise des cycles de potentiel et mesure la charge lors de la désinsertion[2,3].

Voici les résultats pour différentes épaisseurs de Pd sur Pt(100).

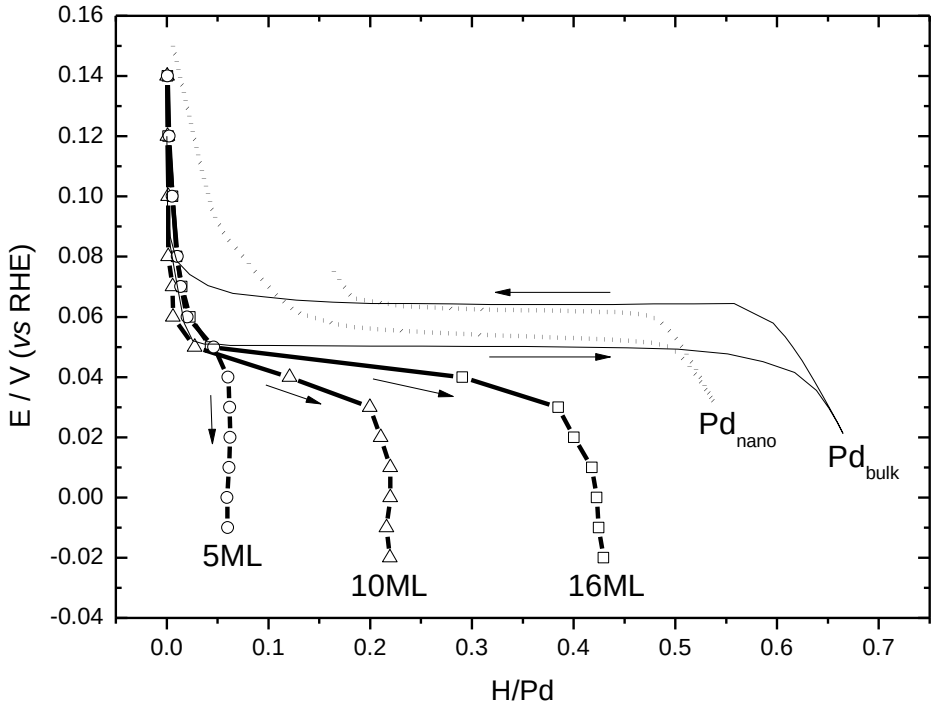

Figure 8.1 : Branche d'insertion de Pd_{xML}/Pt(100)-H dans H_2SO_4 0.1 M ;(O) x = 5ML, (Δ) x = 10 ML, (□) x = 16 ML. Pd massif (—)[2] and nanoparticules (diamètre 3.6 nm) (····)[2] T =25 C.

Comme pour le Pd massif, les isothermes de Pd/Pt(100) peuvent être décrites en trois régions. À haut potentiel (>0.05 V_{ERH}), le taux d'insertion de l'hydrogène est faible (<0.03), correspondant à une solution solide de H dans le réseau de Pd (la phase α). La deuxième région est associée à une hausse rapide de la solubilité d'hydrogène dans un domaine restreint de potentiel(entre 0.05 et 0.03 V_{ERH}). Ceci rappelle le plateau du Pd massif, correspondant à la coexistance des deux phase (α et β). Néanmoins, pour les films Pd/Pt(100), ce plateau présente une inclinaison absente de Pd massif. Enfin, la troisième région, à bas potentiel (<0.03 V_{ERH}) montre un taux d'insertion presque constant. Ça correspond à la phase β.

Avec la diminution d'épaisseur, les taux d'insertion baissent dans les seconde et troisième régions. Les taux d'insertion maximum $(H/Pd)_{max}$ sont égaux à 0.42, 0.22 et 0.06 pour 16, 10 et 5 ML respectivement. Pour Pd_{5ML}/Pt(100), la région intermédiaire n'existe presque plus. Elle ne consiste qu'en une rapide transition entre les deux régions extrêmes.

La comparaison avec des nanoparticules non supportées (diamètre 3.6 nm) montre que l'inclinaison du plateau intermédiaire est une spécificité des nanofilms et non un effet général de la taille nanométrique.

8.2 Système Pd/Pt(111)-H

La méthode utilisée pour mesurer les isothermes sur Pd/Pt(100) est plus difficile à employer sur Pd/Pt(111) en raison de l'insertion d'hydrogène à plus bas potentiel qui induit une concurrence avec la réaction de dégagement d'hydrogène. En particulier, la méthode précédente n'est pas applicable pour les dépôts de Pd de moins de 10 couches atomiques.

Nous avons développé une nouvelle méthode de mesure. Nous avons employé une électrode tournante à ménisque suspendu (HMRDE : Hanging Meniscus Rotating Disk Electrode). Ceci permet, grâce à la convection forcée, d'avoir des conditions plus reproductibles à la surface de l'électrode. Ainsi, la réaction de dégagement d'hydrogène est supposée être constante à un potentiel donné, quelque soit les antécédents de balayage de potentiel. De même, le dihydrogène produit ne doit plus s'accumuler devant l'électrode, évitant sa ré-oxydation parasite ultérieure. Nous avons alors réalisé une intégration du cycle complet d'insertion/désinsertion et nous avons divisé sa charge par deux pour avoir la charge d'insertion.

En complément, nous avons réalisé des mesures sur le film Pd_{1ML}/Pt(111) qui n'est pas sujet à l'insertion d'hydrogène. Nous avons constaté qu'il demeurait à haut potentiel (>0.01 V_{ERH}) la contribution de l'adsorption. À bas potentiel (<0.01 V_{ERH}), la contribution du dégagement d'hydrogène n'apparaît pas identique entre les balayages aller et retour, induisant une charge résiduelle. Comme nous avons observé que l'adsorption était peu dépendante de l'épaisseur des dans la zone juste au-dessus du dégagement d'hydrogène et que la cinétique de ce même dégagement évolue elle aussi de manière limitée, nous avons décidé de soustraire les charges

résiduelles (adsorption et dégagement d'hydrogène) mesurées sur Pd_{1ML}/Pt(111) aux mesures effectuées sur les dépôts plus épais.

Nous avons ainsi pu réaliser des mesures pour des épaisseurs de 3.7 à 14 couches atomiques.

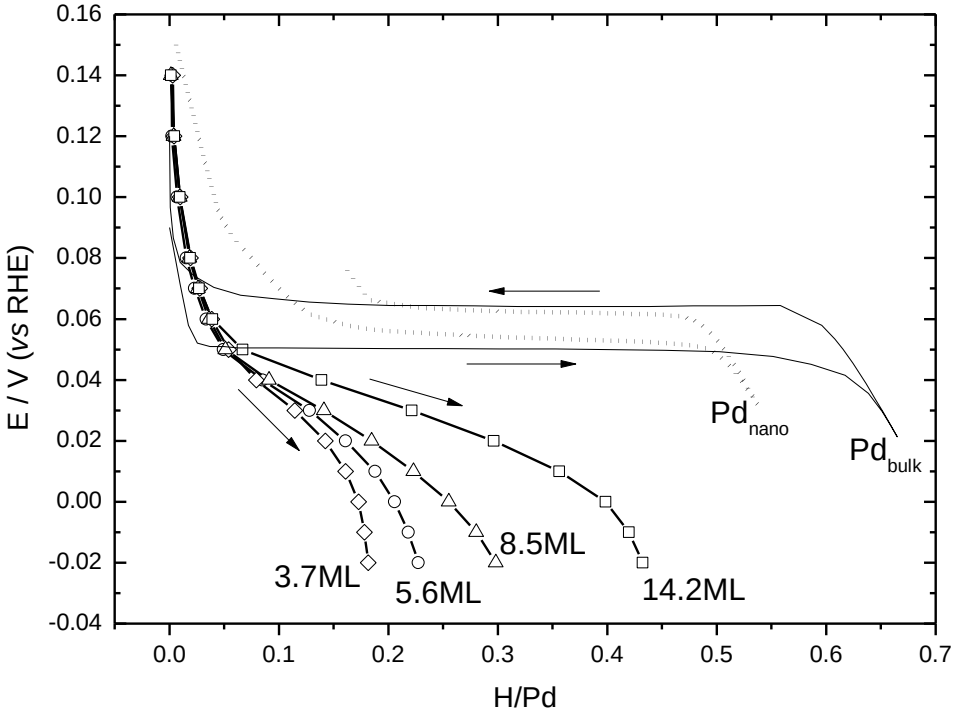

Figure 8.2 : Branches d'insertion des isothermes de H–Pd_{xML}/Pt(111) dans H_2SO_4 0.1 M; (◊) x = 3.7 ML, (O) x = 5 ML, (Δ) x = 10 ML, (□) x = 16 ML. (—) Pd massif[2] et (⋯) nanoparticules (diamètre 3.6 nm)[2]. T =25 °C.

Nous observons de nouveau trois régions, comme pour Pd/Pt(100). Néanmoins, la zone intermédiaire est beaucoup plus inclinée avec une transition sur 60 mV au lieu de 20 mV pour Pd/Pt(100). Inversement, les taux d'insertion maximum $(H/Pd)_{max}$ diminuent moins vite avec la réduction d'épaisseur. Nous observons une fois de plus une influence importante du substrat et plus particulièrement de son orientation cristallographique.

8.3 Reference

(1) Kibler, L. A. *International Society of Electrochemistry* **2003**, 1–55.

(2) Lebouin, C.; Soldo-Olivier, Y.; Sibert, E.; Millet, P.; Maret, M.; Faure, R. *Journal of Electroanalytical Chemistry* **2009**, *626*, 59–65.

(3) Birry, L.; Lasia, a. *Electrochimica Acta* **2006**, *51*, 3356–3364.

(4) Lebouin, C. Films d'épaisseurs nanométriques de Pd sur Pt(111): élaboration, caractérisations et étude de l'électro-insertion de l'hydrogène, Grenoble University, 2008.

(5) Sheng, W.; Gasteiger, H. A.; Shao-Horn, Y. *Journal of The Electrochemical Society* **2010**, *157*, B1529.

(6) Conway, B. E.; Tilak, B. V. *Electrochimica Acta* **2002**, *47*, 3571–3594.

(7) Freitas, K. S.; Lopes, P. P.; Ticianelli, E. a. *Electrochimica Acta* **2010**, *56*, 418–426.

(8) Montero, M. a.; Gennero de Chialvo, M. R.; Chialvo, A. C. *International Journal of Hydrogen Energy* **2011**, *36*, 3811–3816.

(9) Santos, L. G. R. a.; Freitas, K. S.; Ticianelli, E. a. *Journal of Solid State Electrochemistry* **2007**, *11*, 1541–1548.

(10) Cahan, B. D.; Villullas, H. M. *Journal of Electroanalytical Chemistry and Interfacial Electrochemistry* **1991**, *307*, 263–268.

(11) Cahan, B. D.; Villullas, H. M.; Yeager, E. B. *Journal of Electroanalytical Chemistry and Interfacial Electrochemistry* **1991**, *306*, 213–238.

(12) Pérez, J. M.; Gonzalez, E. R.; Villullas, H. M. *The Journal of Physical Chemistry B* **1998**, *102*, 10931–10935.

(13) Pérez, J. M.; Villullas, H. M.; Gonzalez, E. R. *Química Nova* **1997**, *20*, 555–559.

(14) Pérez, J. M.; Villullas, H. M.; Gonzalez, E. R. *Journal of Electroanalytical Chemistry* **1997**, *435*, 179–187.

(15) Villullas, H. M.; Brunetti, V.; Teijelo, M. L. *Journal of Electroanalytical Chemistry* **1997**, *437*, 255–258.

(16) Villullas, H. M.; Teijelo, M. L. *Journal of Electroanalytical Chemistry* **1996**, *418*, 159–165.

(17) Villullas, H. M.; Teijelo, M. L. *Journal of Electroanalytical Chemistry* **1995**, *385*, 39–44.

(18) Villullas, H. M.; Teijelo, M. L. *Journal of Electroanalytical Chemistry* **1995**, *384*, 25–30.

(19) Lebouin, C.; Soldo-Olivier, Y.; Sibert, E.; De Santis, M.; Maillard, F.; Faure, R. *Langmuir* **2009**, *25*, 4251–5.

(20) Soldo-Olivier, Y.; Lafouresse, M. C.; De Santis, M.; Lebouin, C.; De Boissieu, M.; Sibert, E. *The Journal of Physical Chemistry C* **2011**, *115*, 12041–12047.

(21) Rose, A.; Maniguet, S.; Mathew, R. J.; Slater, C.; Yao, J.; Russell, A. E. *Physical Chemistry Chemical Physics* **2003**, *5*, 3220.

(22) Suleiman, M.; Faupel, J.; Borchers, C.; Krebs, H.-U.; Kirchheim, R.; Pundt, a. *Journal of Alloys and Compounds* **2005**, *404-406*, 523–528.

(23) Wagner, S.; Uchida, H.; Burlaka, V.; Vlach, M.; Vlcek, M.; Lukac, F.; Cizek, J.; Baehtz, C.; Bell, A.; Pundt, A. *Scripta Materialia* **2011**, *64*, 978–981.

(24) Ruban, A.; Hammer, B.; Stoltze, P.; Skriver, H. .; Nørskov, J. . *Journal of Molecular Catalysis A: Chemical* **1997**, *115*, 421–429.

(25) Kitchin, J.; Nørskov, J.; Barteau, M.; Chen, J. *Physical Review Letters* **2004**, *93*, 156801.

(26) Pundt, A.; Suleiman, M.; Bähtz, C.; Reetz, M. T.; Kirchheim, R.; Jisrawi, N. M. *Materials Science and Engineering: B* **2004**, *108*, 19–23.

9 Conclusion générale

Le présent travail est axé sur l'électrodéposition, la caractérisation et la capacité de stockage d'hydrogène de nanofilms sur Pt(100). Ces nanofilms ont été électrodéposés en présence de chlorures dans l'électrolyte. La caractérisation des nanofilms en milieu sulfurique révèle des signatures bien définies pour différentes couches. La croissance pseudomorphique des deux premières couches commence par une première étape d'adsorption, suivie par un mécanisme de croissance par nucléation. Pour des films de Pd plus épais, une croissance 3D est observée avec formation d'une base d'îlots carrés. La comparaison des films Pd/Pt(100) et Pd/Pt(111) révèle des caractéristiques distinctes tant sur la courbe d'électrodéposition que sur la caractérisation électrochimique. Ces différentes observations semblent être reliées aux sites d'adsorption dans les différentes orientations. L'absorption d'hydrogène dans les nanofilms a été étudiée en milieu sulfurique pour le système Pd/Pt(100). Une nouvelle méthode a également été développée dans le but de calculer l'insertion d'hydrogène dans des films de Pd de moins de 10 ML sur Pt(111) en utilisant l'hanging meniscus rotating disk. Les isothermes d'insertion montrent des différences entre Pd/Pt(100) et Pd/Pt(111) comme un maximum de ratio d'insertion $(H/Pd)_{max}$ et une pente caractéristique pour le plateau de transition de phase. Cette valeur $(H/Pd)_{max}$ diminue avec l'épaisseur du film dans les deux cas, approchant environ 14 ML.